2008

A statistical based damage detection approach for highway bridge structural health monitoring

Ping Lu
Iowa State University

A statistical based damage detection approach for highway bridge structural health monitoring

by

Ping Lu

A dissertation submitted to the graduate faculty

in partial fulfillment of the requirements for the degree of

DOCTOR OF PHILOSOPHY

Major: Civil Engineering

Program of Study Committee:
Terry J. Wipf, Co-major Professor
Brent M. Phares, Co-major Professor
Loren W. Zachary
Reginald R. Souleyrette
Zhengdao Wang
Huaiqing Wu

Iowa State University

Ames, Iowa

2008

TABLE OF CONTENTS

APPENDICES

LIST OF FIGURES

LIST OF TABLES

ACHNOWLEDGMENTS

I would like to take this opportunity to express my thanks to those who helped me throughout my Ph.D. Study.

First and foremost, I would like to thank my major professors Dr. Brent M. Phares and Dr. Terry J. Wipf for their valuable guidance, patience and support throughout this research and the writing of this dissertation. Their insights and words of encouragement have greatly inspired me. Words are not enough to thank them for their constant support through my stay at ISU, and above all, for teaching me the way to do research.

I would also like to thank my committee members Dr. Huaiqing Wu, Dr. Zhengdao Wang, Dr. Loren W. Zachary, and Dr. Reg Souleyrette for their suggestions for the research.

Deep appreciation and thanks to Dr. Lowell Greimann for his valuable guidance, insightful advices, encouragement and support throughout my study. His understanding toward life will inspire me forever.

I would also like to thank Dough Wood, ISU Research Laboratory Manager, for his contribution to the field testing. Thanks to my officemates Justin Doornink, Ursula Deza, Jake Bigelow, and Yoon-Si Lee who have gladly extended their help for this project. I wish to thank Nick Burdine, the system analyst of CTRE, for helping me set up the hardwares. Special thanks to my friends Ursula Deza, Jiong Hu, and Gang Lv with whom my studying life at ISU became more memorable.

Last but not the least, I would like to express my hearty gratitude to my husband, my parents and my sisters. Their consistent and selfless love made my dream come true.

ABSTRACT

Upon the request of Iowa DOT, the Bridge Engineering Center (BEC) of Iowa State University developed a fiber optic sensor (FOS) structural health monitoring (SHM) system to monitor the fatigue crack formation for fracture critical bridges in 2006. The system enables bridge owners to remotely monitor bridges for gradual and sudden damage formation. However, the correlation between the data analysis results and damage was not objectively defined; bridge owners need to interpret the results according to their experiences. To improve the existing SHM system, a statistical damage detection method was proposed and analytically evaluated in this work.

The basic idea of this method is that the response of a normal structure is different from that of the damaged structure. To define the difference mathematically, Shewhart $\overline{X}$ control chart analysis was carried out over a strategically defined damage indicator (i.e. residuals calculated from cross prediction models). With different prediction models and different damage indicator calculation procedures, three damage detection methods (one-to-one model direct evaluation method, two-level evaluation method, and many-to-one model method) were studied. As a result, the one-to-one model direct evaluation method was recommended due to the best performance in terms of both damage sensitivity and damage location detection accuracy. For this method, significant efforts were made to select the performance matrix, the load condition, and residual matrix simplification procedure. Results show that using event strain ranges obtained from right-lane, five-axle, heavy trucks along with the combined summation residual matrix simplification approach lead to the best damage detection performance. The optimal group size used in the control chart analysis was also recommended based on the synthetic data verification.

Compared to the previously developed damage detection method, improvements were made by:

1. Developed a strain-based truck detection sub-system, which can detect truck events and calculate relevant parameters including the number of axles, axle spacings, speed, event start and end time, and weight group autonomously in a near-real-time fashion. The sub-system has been integrated into the existing SHM system successfully.

2. The truck detection subsystem allowed for a successful data selection procedure. Using a single truck type during the structural evaluation improved the performance of the system significantly.
3. Using the simplified residual as the damage indicator enabled reliable mathematical control limits selection. The strategically defined damage indicator significantly improved the damage detection power of the method.
4. By using the uniquely one-to-one cross prediction model, the developed damage detection approach can be applied for virtually all types of bridges.
5. The control chart analysis results show the damage occurrence and damage location directly.

CHAPTER 1 INTRODUCTION

1.1 General Background

Currently, bridge condition information is primarily obtained through scheduled biennial visual inspection which is enforced by the National Bridge Inspection Program (NBIP). However, a study funded by the Federal Highway Administration (FHWA) concluded that these are labor and cost intensive (Dubin 2001) and that visual inspections are subjective and unreliable (Phares 2001). In addition, the effectiveness of these periodic inspections is highly constrained by the shortage of timely damage detection ability. Therefore, to maintain overall highway operational safety with current funding limitations, the development of continuous, automatic, and low cost bridge structural health monitoring (SHM) systems is highly and urgently demanded.

Benefiting from the rapid development of computing, sensing, and tele-communication technology during the last two decades, computer-based long term SHM systems have been studied and are more and more widely utilized to provide timely condition information. A SHM system includes data acquisition, storage and analysis hardware and software, and evaluates the status of entire structure or structural component continuously. It is desired that damage, which is defined as the changes introduced into a structural system that adversely affects its current or future performance (Sohn 2003), be detected at an early stage. To do this, an effective comparison between the measured response from an unknown structural status and its undamaged response is necessary. As a powerful comparison tool, statistical pattern recognition has shown its effectiveness in several SHM approaches. In this research, a statistical control chart was employed as the data analysis tool to identify structural damage from continuously collected strain data.

Extremely large data volumes have been seen as problematic attributes of some long term SHM systems. Data reduction that results in the extraction of useful information from the original data is a key step toward the development of a real-time/near real-time damage detection approach. It is probable that only global changes such as foundation settlement, bearing failure or major defects, such as the loss of main cable tension or the rupture of the deck, would be detectable by global SHM procedures with a minimum of optimally located sensors, as Saint Venant's principle indicates that the zone of influence is typically small. It is hard, if not impossible, to find a global

measurement that can be monitored by a few sensors while sensitive to the localized structural response change. Therefore, a relatively dense and wide spread sensor network is necessary to achieve the required coverage if the damage location is not already known. At the same time, the data acquisition frequency should be sufficiently high so that enough information can be obtained to support the decision making. High data collection frequencies coupled with large sensor numbers leads to extremely large data volumes. Obviously, processing and saving all the data in a near real-time fashion is not only impossible, but unnecessary. Thus, extracting only the useful information from the collected data is important. In this research, the event extreme strains (e.g. maximum and minimum strains) from vehicle passage events are extracted from the original data and used in the damage detection analysis. By doing so, the data volume was reduced from 46k/sec to 0.6k/truck. At peak traffic volumes, the reduction can be higher than 98% with more dramatic reductions during off peak times.

Data preprocessing and damage indicator selection are essential to the sensitivity of the damage detection approach. In the operational environment, highway bridges are inevitably subjected to many changing factors that will affect the monitored structural performance metric. If the variances caused by these factors are not properly addressed, they can either mask the subtle changes caused by structural damage and reduce the sensitivity of the damage detection approach or result in undesirable false alarms. In this research, algorithms were utilized/developed to address three major factors: 1) temperature induced strain, 2) vibration due to the interaction between trucks and the bridge, and 3) variance caused by different types of trucks and travel lanes. In addition to the data cleansing strategies, damage indicators were also developed to reduce the effect of weight variability of ambient trucks. Using the event extreme strains or by combining them into an event strain range, linear prediction models can be constructed. It is assumed that the linear models developed from the undamaged structure response can not predict the response of damaged structure at the damage vicinity areas. Therefore, residuals (i.e. the difference between predicted and measured strains) are used as the damage sensitive feature.

Applying control chart analysis on the residuals is the concept for the proposed damage detection solution. In general, large numbers of out of limits data points on the control chart does not necessarily indicate the occurrence of structural damage. Rather this is an indication that the system has varied, causing a statistically significant change in the structural response. However, in this work,

the variability of the environmental and operational conditions has been eliminated during the data preprocessing. So the structural damage is considered to be the primary cause of changes of the system.

1.2 Scope and Objective of Research

This study is an improvement and extension of the fracture critical bridge (FCB) monitoring project conducted by Doornink (2006). Efforts were carried out to:

1) Develop an autonomous, strain-based, truck parameters detection sub-system. The output of the sub-system can not only be used to select data for the damage detection procedure, and such, reduce the operational variability, but it can also provide details of the composition and density of trucks that unitize the bridge
2) Extend the previously developed damage detection approach, which assume the damage vicinity is known, into a general purpose one. In this way, users are not required to differentiate the sensors into TS (sensors installed in the damage prone areas) and NTS (sensors not near damage prone areas) and the approach is therefore widely applicable.
3) A more systematic control chart analysis approach was developed, so that:
    a. The control limits can be established mathematically
    b. Each sensor is associated with only one control chart. In this way, the control chart results indicate both damage occurrence and location directly.
4) Evaluate the damage detection approach using synthetic data to determine:
    a. Probability of detection (POD)
    b. Detection delay (how many trucks need to pass the bridge to ensure a 99% chance of damage capture) and its relation with the damage level.
    c. Propose an optimal group size which can achieve the smallest detection delay for slight damages.

1.3 Organization of the Dissertation

In the remainder of this dissertation, a review of the SHM concepts, their application in bridge engineering, and damage detection algorithms is presented in Chapter 2. Chapter 3 illustrates the hardware of the SHM system and the demonstration bridge. In Chapter 4, the details of the data preprocessing procedure are described. Significant attention is placed on the illustration of the developed truck detection sub-system and the data selection procedure. Presented in Chapter 5 are

the damage detection algorithm development and its performance evaluation. Finally, Chapter 6 summarizes the research work and the conclusions made about the developed damage detection approach and the truck detection sub-system. Recommended future work is also provided in Chapter 6.

CHAPTER 2 LITERATURE REVIEW

Structural health monitoring has been widely studied during the past two decades. Significant progress has been achieved to develop new sensors and systems that are capable of monitoring the performance of a structure. Some of them claim to be able to perform structural system prognosis and management optimization. A large amount of related research can be found in the literature. However, only a few selected pertaining topics including the general concepts of SHM and selected damage detection approaches are reviewed here to show the novelty and advantages of the SHM solution proposed in this research. Special efforts were put on the review of static (pseudo static) strain based damage detection approaches and damage detection approaches using statistical control charts.

2.1 General Concept of SHM

2.1.1 Definition of SHM

There is no standard definition of SHM in the literature. Sohn and et al (2003; Inman 2004) define it as the process of implementing a damage identification strategy for aerospace, civil and mechanical engineering infrastructure. Damage is defined here as changes introduced into a system that adversely affects its current or future performance. Brownjohn (2007) pointed out SHM is a continuous system identification of a physical or parametric model of the structure using time-dependent data. Balageas (2006) said SHM aims to give, at every moment during the life of a structure, a diagnosis of the "state" of the constituent materials, of the different parts, and of the full assembly of these parts constituting the structure as a whole. Much more definitions can be easily found in the literature. Although they are different from one another, all imply that SHM system should be able to collect time dependent data and interpret the data in terms of structural performance states.

SHM involves the integration of sensors, possibly smart materials, data transmission, computational power, and processing ability inside the structures. It makes it possible to reconsider the design of the structure and the full management of the structure itself and of the structure considered as a part of wider systems (Balageas 2006). As shown in Fig. 2.1, SHM systems may be organized as following three level configurations:

1) The monitoring of structure integrity and usage conditions
2) Mixing the information of the integrity monitoring sub-system with that of the usage monitoring sub-system and with the knowledge based on damage mechanics and behavior laws makes it possible to determine the prognosis (residual life) and the health management of the structure (organization of maintenance, repair operations, etc.)
3) Similar structure management systems related to other structures which constitute a type of super system (a fleet of aircraft, a group of power stations, etc.) make possible the health management of the super system.

Workable systems can be set up at any level described above. Obviously, the SHM system organization presented by Balageas can be improved by incorporating the usage condition data into the integrity monitoring function, so that the diagnosis ability of the system can be further improved.

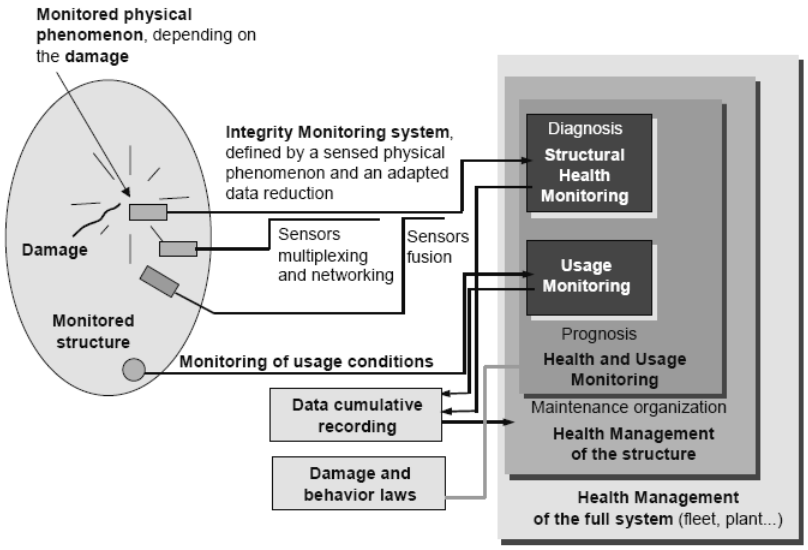

Figure 2.1 Principle and organization of a SHM system (Balageas 2006)

2.1.2 Motivations of SHM

Life-safety and economic impact are two major motivations for the development of SHM techniques. Knowing the integrity of in-service structures on a continuous, real-time basis is important for manufacturers, end-users and maintenance teams. In effect, SHM:

- allows an optimal use of the structure, a minimized downtime, and the avoidance of catastrophic failures,
- gives information needed to improve the products,

– changes the work organization of maintenance services:
    i) replace scheduled and periodic maintenance inspection with performance-based (or condition-based) maintenance (long term) or at least (short term) by reducing the present maintenance labor, in particular by avoiding dismounting parts where there is no hidden defect;
    ii) Dramatically minimize the human involvement, and consequently reducing labor, downtime and human errors, and thus improving safety and reliability.

When applied in civil infrastructure community, Ross (1995) and Mita (1999) identified some cases where SHM may be required:

1) Modifications to an existing structure,
2) Monitoring of structures affected by external works,
3) Monitoring during demolition,
4) Structures subject to long-term movement or degradation of materials,
5) Feedback loop to improve future design based on experience,
6) Fatigue assessment,
7) Novel systems of construction,
8) Assessment of post-earthquake structural integrity,
9) Decline in construction and growth in maintenance needs, and
10) The move towards performance-based design philosophy.

Within the last two decades, long-term SHM of bridges has been increasing dramatically due to the factors (Pines 2001; Farrar 1997):

1) Aging of bridge infrastructure
2) Bridge failures
3) Realization of the ineffectiveness of visual inspection
4) Technology development

2.1.3 Brief History of SHM in Bridge Engineering

As the worldwide civil infrastructure is rapidly aging, much recent attention had been focused on bridge SHM. It is impossible to identify the first form of SHM that had been applied in bridge engineering, but discounting simple periodic visual inspection, formal structural monitoring and

interpretation using recording instruments began in the latter half of the last century and accelerated with the use of electric data storage and computer data acquisition (Brownjohn 2007).

Bridge monitoring programs have been historically implemented for the purpose of understanding and eventually calibrating models of the load-structure response chain (Bampton 1986; Barr 1987; Brownjohn et al. 1994; Farrar 1994; Cheung 1997; Koh et al. 2003; Wang 2003). One of the earliest documented systematic bridge monitoring exercises, by Carder (1937), was conducted on the Golden Gate and Bay Bridges in San Francisco in an elaborate program of measuring periods of the various components during their construction to learn about the dynamic behavior and possible consequences of an earthquake. Another early stage bridge monitoring project was conducted by University of Washington (1954). The monitoring of Tacoma Narrows Bridge over its short life before it collapsed due to wind-induced instability, again, focused on vibration measurements, but with an obviously warranted concern for the health of the structure.

In the last two decades, permanent bridge monitoring programs have evolved into formal modern SHM systems, which have been implemented in major bridge projects in North America (Farrer 1994; Seible 1996; Catbas 2001), Japan (Nagayama 2004; Fujino 2003; Wu 2003), Hong Kong (Wong 2000; Wong 2003; Ni 2002; Ko 2002), and mainland China (Ou 2003). These projects benefitted not only the bridge owners but the SHM research community dramatically. Through these projects, numerous damage detection approaches were developed and some of them were verified by field test.

In parallel to the development of SHM systems for long-span bridges, short-span bridge monitoring was also widely studied. For smaller bridges, global response is more sensitive to defects, visual inspection is less frequent and SHM systems have made a more realistic contribution (Alampalli 1994) to bridge owners and end users. Full-scale testing for short-span highway bridge assessment (Salane 1981; Bakht 1990; Xia 2005) is relatively easy to perform. In European the BRIMOS system (Geier 2002) has been used to track bridge dynamic characteristics. Studies in Australia have focused on the typical very short-span highway and railway bridges; in one case leading to a commercial product of the ‘Bridge Health Monitor’ (Heywood 2000), which is programmed to record selected waveforms of vehicle-induced response while logging statistics of strains due to such events.

SHM also recently applied in bridge management programs (Yanev 2003). In managing the transportation system, it is essential to understand the true state of health and rate of degradation of each significant bridge of the transportation system at large, which often cannot be determined from visual inspections only (Aktan 2001; Catbas 2001). Verifying the effectiveness of bridge upgrading project can also involved SHM. Examples include the Severn and Wye Bridge Refurbishment (Flint 1992), Tamar Bridge (List 2004) in the UK and Pioneer Bridge, Singapore (Brownjohn 2003a & b).

2.2 Damage Detection in SHM

As discussed above, applications of modern SHM have gone beyond damage detection. Nevertheless, detecting damages/deterioration as early as possible is still one of the most essential functions of SHM systems and it is far from fully addressed. Numerous damage detection methods are discussed in the literature. They can be classified according to many different standards.

According to the monitoring measurements, they can be classified into non-destructive evaluation (NDE) based method, and non-NDE based method. Overall, SHM can be viewed as an extension and improvement of NDE. However, NDE-based methods are used here to refer to methods developed directly from classic NDE techniques. In bridge monitoring, ultrasonic and acoustic emission (AE) are the most popular NDE techniques that have been converted into SHM systems. Damage detection approaches belong to this category are briefly reviewed in Section2.2.1. For non-NDE based methods, they can be further grouped into dynamic-based and static-based methods according to the selected damage evaluation matrix.

Damage detection approaches can also be classified into model-based or model free methods. Methods which involved mathematical analysis model of the monitored system, such as finite element model (FEM), are called model-based methods. These methods typically solve the damage detection through system identification or model updating. On the other hand, if damage detection approaches were developed based on pure time domain structural response data, they are referred as model-free approaches. For model-free methods, damage detection problems were mainly solved by statistical approaches including control theory and process automation (Fritzen 1998; Sohn 2003).

The research described herein focuses on the development of a model free damage detection approach which uses the residual obtained from quasi-static strain as the damage evaluation matrix and statistical control chart was employed as the pattern recognition tool. Therefore, in this report, more efforts were put on the review of works pertaining to this including the static-based damage detection and model-free statistical pattern recognition approaches, special efforts were put on the application of control chart in damage detections. To be complete, other methods are also briefly discussed.

2.2.1 NDE Based Methods

NDE and NDE-based SHM have long been developing in parallel. Several classic NDE techniques can be converted into SHM system by integrating sensors and actuators inside the monitored structures. Unlike classic NDE, for which, the excitation is generally achieved using an external device. The excitation for NDE-based SHM system is generated by the build-in actuators. Applications of NDE based damage detection are more popular in mechanical and aerospace industries than in bridge engineering. For mechanical and aerospace structures, knowledge of the damage prone areas is more readily available. When applied in bridge engineering, ultrasonic and Acoustic Emission (AE) techniques are mainly utilized.

Traditional ultrasonic testing can be easily converted into acousto-ultrasonic SHM system using embedded or surface mounted piezoelectric patches. Ihn (2004a and b) used ultrasonic guided Lamb waves to maximize measurements at the receiving sensors. It was assumed that that any change in the received signal from the constant transmitted signal was due to a change in structural condition. Testing on a notched aluminum plate and riveted fuselage joint showed good damage detection results.

AE methods are famous for the ability to detect a crack growing in real-time (Prine 1995). Since the inception back in the 1970's AE monitoring has developed into a reliable and widely used monitoring tool on both small rural bridges and large highway bridges. Examples include:

1) Wisconsin Department of Transportation Bridge B-5-158 is located in the city of Green Bay in Brown County, Wisconsin (Prine 1995)
2) Caltrans Structure B-28-153, Benicia Martinez, CA (Prine 1995)
3) Texas DOT Fred Hartman stay-cable Bridge (Kowalik; Higgins 2006)

More AE based damage detection methods were thoroughly reviewed by Flannigan (2005).

In civil infrastructures monitoring, the NDE-based damage detection approaches faced the criticism that users have to know the damage vicinity in advance and damage prone areas have to be readily accessible.

2.2.2 Non-NDE Based Methods

For long-term SHM, the original data volume is typically huge. Extracting useful information from the data is important. Converting the original monitoring data, such as acceleration or strain data, into system dynamic property parameters including natural model frequencies, mode shapes, and curvature of mode shapes, has been widely used. These methods are usually refereed as dynamic-based methods. Some authors also named them as second order methods, since the parameters have to be obtained from first order data through major data transform action (Li and Zhang 2006). On the other hand, the static-based method typically uses the monitoring data directly or with a simple transform to increase the damage sensitivity. These two types of methods will be reviewed in the following and focus was laid on static strain-based algorithms.

2.2.2.1 Dynamic Based Approaches

Dynamic based methods were originally developed in mechanical engineering and aerospace engineering communities, and are widely applied in bridge monitoring currently. They are attractive since the free vibration characters of a structure are generally independent of the excitation source. Dynamic-based damage detection approaches showed a certain degree of success in many projects (Kim 1995; Wong 2000; Ni 2002). Much more were thoroughly reviewed and very well documented in (Doebling 1998; Sohn 2003; Doornink 2006). However, large bias toward its application in long-term bridge SHM existed in the literature. As many researchers pointed out (Doebling 1998; Sohn 2003; Farrar 1997):

1) Damage is a local phenomenon which can only be captured with higher natural frequencies and mode shapes. Typically, accurate higher frequencies and mode shapes are difficult to obtain due to the great modal density and coupling between modes. Additionally, ambient traffic can hardly excite the higher modes, so outside excitation has to be applied.
2) The modal properties are second level measurements; they have to be estimated from first level monitoring data. Acceleration is one of the most common first level measurements

used in dynamic based SHM system. Errors in the estimation procedure and within the original data potentially lead to inaccurate, even, misleading results.

3) The variation in excitation or environment conditions can hardly compensate and can easily mask the damage caused variation.

Be aware of these, static-based damage detection gained increasing attention in the last few years.

2.2.2.2 Static Based Approaches

Static-based damage detection approaches typically measure responses of displacement or strains. Comparing these two, strain-based approaches are more popular since the techniques for strain measurement are very mature and strain data can be easily used for multiple purpose monitoring (Jarkko 2003). Strain-based methods are more related to this research so it is thoroughly reviewed in this section.

Supervised learning method

Most static strain-based damage detection approaches use supervised learning method, so data for damaged structure are required for the system training. In practice, the damaged structural data are typically unavailable; therefore, finite element or other theoretical analysis models have to be created to generate the training data sets. This type of methods showed some degree of success in lab tests or numerical studies. However, the requirement of an analytical model could be a big hurdle for the development of general purpose damage detection algorithms. Some examples of such algorithms were reviewed in the following.

Jarkko et al (2003) showed the damage detection potential of strain data for modern military aircrafts. A series of finite element analysis were completed for different damage cases to predict the output of strain gauges in crack affected area. FEA results were used to determine the sensor location and orientations. The results were also used to determine the damage alarm threshold. Damage detection was performed by comparing the strain data directly. Results from two fatigue tests show that strain gauges can detect cracks early enough to maintain flight safety. In this research, the damage prone areas were assumed to be known, and no live load variation was involved.

Gope and Ramadas (2005) trained ANNs with simulated strain data to detect damage at the middle of a cantilever beam. The damage feature vector was defined as $1-\frac{\varepsilon_{damage}}{\varepsilon_{undamage}}$. The smallest detectable damage achieved by this work was a 5 percent cross section area reduction, which is equivalent to an 18.6 percent reduction in the moment of inertia. Supervised learning is used and a structural damage feature database has to be generated from finite element analysis with this method.

Kesavan et al (2005) implemented a static-based damage detection method via ANNs which is trained by FEA for various damage conditions. Synthetic delaminating damage with the size of 75mm for a simply supported composite beam was then detected by the trained ANNs. The proposed approach required a very dense sensor array; the distance between two sensors can not be larger than 50mm.

Lu and Phares (2006) presented a static-based damage detection approach, which can detect small damage with a relative small number of strain sensors by using a special damage indicator called the event-based Cumulative Live Load Strain Energy Density (CLLSED). Feed-forward back-propagation supervised ANNs were trained to predict structural damage severity and location in three stages. First, an ANN was used to predict live load condition represented by truck type and truck weight. Secondly, the live load condition together with CLLSED was used to predict the damage occurrence and damage severity. Finally, all the obtained information was fed to an ANN to determine the damage location. This research indicated that by including live load information the damage detection power can be improved.

Fujimoto (2005) proposed a method of estimating the depth of a surface crack based on the measurement of the crack opening deformation (COD) using strain gauges. COD obtained from target sensor installed right above crack line was normalized against the strain data collected by sensors bonded farther from the crack. The normalized COD was multiplied by a factor calculated from FEA results, and then used to estimate crack depth through a numerical iteration method. The data normalization is showed to be important to reduce the excitation uncertainty.

Hu (2003) used a static-based dead load redistribution method to determine the location and severity of damage in a two-span continuous beam. Since dead load was used as the excitation, the

strain response measurements are static, and the load is constant. The damage detection problem was formulated as a constrained optimization problem, and it was solved with a generic algorithm. Finite element model was involved to create the damage database. Results show that this method can detect damage location well. However, the damage severity detection accuracy is not so high.

Unsupervised learning method

Only a few unsupervised static strain-based damage detection methods can be found in the literature.

Idriss (1995) presented the field testing results for the I-40 bridge over the Rio Grande before it was razed in mid 1993. The bridge was instrumented with strain gages to monitor the positive and negative moments in the girders, forces in the cross bracing, and moments in the floor beams in the vicinity of a crack. Dead load strains and static live load strains were measured before and after damage creation. Results indicated that force redistribution did not occur until the bottom flange was completely cut. The girder bottom sensors that were installed near the damage experienced a strain surge as the damage level increases. However, other sensors showed very little strain change until the final cut. The short term field control testing concluded that damage was directly detectable through strain monitoring. However, this work is far from a field applicable damage detection method that can satisfy the requirement of long term SHM.

Wipf and et al (2006) developed a long term remote monitoring system for a bridge constructed with high performance steel. With this system, strains were collected using 40 fiber optic sensors at a frequency of 31.25Hz. Conventional design parameters, including distribution factors (DF), neutral axis (NA), end restraint (ER), were calculated in real-time from the collected data to evaluate the performance of the bridge and to look for changes with time. The prototype system developed in this project was proved to be effective and efficient. The system successfully solved data management and communication problems. However, since the bridge performed well, and no synthetic damage was introduced, there is no chance to verify the effectives of this system, and no systematical comparison algorithm was developed.

The SHM system developed by Doornink (2006) is probably the most sophisticated long term highway bridge monitoring system which collected strain data and used them in the structural states

evaluation. The damage detection approach discussed in this dissertation is an extension and improvement of Doornink's work. It will be reviewed in details in Section2.4

2.3 The Application of Statistical Control Chart in Structural Damage Detection

Since Farrar and Doebling (1999) defined the SHM process as a statistical pattern recognition problem, more and more damage detection algorithms using statistical analysis tools have been proposed in the literature. When data are available from both the undamaged and damaged structure, the supervised statistical pattern recognition algorithms can be applied. Some examples of the supervised learning approaches have been reviewed in Section 2.2.2.2. On the other hand, the unsupervised learning approaches involved data from undamaged structure only. With the unsupervised learning approach, some form of outlier analysis must be applied. They can be unsupervised neural networks, hypothesis testing, outlier detection, and control chart analysis. Since the control chart analysis method has been used in this research, the review present here will focus on this type of method. Other statistical based damage detection methods are very well documented in (Sohn 2003).

2.3.1 Early Stage Control Chart Based Damage Detection Methods

The major objective of early stage research works include: 1) prove the effectiveness of applying the control chart technique in structural damage detection, and 2) provide a general framework for control chart based damage detection approach. Among the literature summarized in this section, none addressed the environmental or operational variation induced structural response changes, and the damage location detection was not studied neither.

The first paper that introduced control charts into structural damage detection is presented by Sohn and et al (2000). In this paper X-bar control chart was employed to analyze acceleration data collected by forty sensors installed on a reinforced-concrete column which was originally designed for the research of a seismically retrofit. A series of quasi-static cyclic tests were performed on the column to create progressive damage, and at intermittent stages during the testing, vibration tests were performed to collect the data. The coefficients of autoregressive (AR) models were selected as the damage sensitive feature. The study includes three major parts. First, the applicability of control chart to the damage detection problem was demonstrated using individual time series obtained from different measurement points. AR models were constructed using the measured time history

data and the first AR coefficient was used in the X-bar control chart analysis. The demonstration provides a framework for using x-bar control chart in damage detection. In the second part, linear and quadratic projections were applied to map the multidimensional AR coefficient into a 1D feature space, and control chart analysis was performed on the transformed damage indicator. The robustness of the proposed approach against false-positive was verified. Finally, principle component analysis (PCA) was employed by including the data collected by all forty sensors. The data are first projected onto the first principle component of the covariance matrix, and then feature selection is performed using the compressed data. Analysis results indicated that using the projection of multiple coefficients is better than using only the first AR coefficient. When combining the PCA analysis with the projection technique, the damage detection results were slightly improved. This work verified the effectiveness and provided the framework of solving damage detection problem with control chart. However, since the data used in this research were collected from control testing, when applied in practice, the excitation variance and environmental variance issue would have to be addressed. In addition, this work only addressed the identification of damage existence; the damage location problem was not studied.

In a follow up research work (Fugate 2001), a new damage sensitive feature, the residual of the AR(5) model, was proposed. The x-control chart and s-control chart analysis were carried out to compare the residual matrix for undamaged structure and damaged structure for one selected sensor. The data used in this research is the same as those used in the previous work. Analysis results show that for all damage levels, both x-control chart and s-control chart indicated some system anomaly. The effectiveness of the proposed damage indicator was verified through this research. Same as the previous work, the damage location detection was not discussed, and the live load variance or environmental variance is not involved in this work.

In another project conducted by Sohn (2001), the control chart analysis based damage detection approach was applied to the strain data obtained from a surface-effect fast patrol boat. In this work, the residuals of the AR model was, first, used as the damage indictor, and the control chart analysis result did not indicate the damage successfully. Later, a complicated damage sensitive feature which normalized the data and removed operational and/or operational effects was created. Successful damage detection was achieved by analyzing the complicated damage sensitive feature with a supervised learning approach. However, the control chart analysis was not performed against the

new damage indicator. Nevertheless, it can still be seen that, when live load and environmental variance were involved, the data preprocessing and damage indictor selection are crucial.

Kuallaa (2003) studied the Z24 Bridge in Switzerland using the data collected by four sensors from three damage configurations (undamaged, and pier settlement of 40 and 95mm). Different control charts analysis approaches (Univariate and multivariate Shewart, x, CUSUM, and EWMA) were investigated by using different dynamic features (natural frequencies, mode shapes, and damping ratios). Results showed that all control charts can detect the damages. However, each chart has its advantages and disadvantages. Hotelling T is insensitive to small response shift; therefore, if the false alarm is the primary concern, it can be a good choice. CUSUM and EWMA are sensitive to small shifts and, such, may cause frequent false alarm too. Schewart control chart was found to be the most reliable analysis tool for on-line damage detection. The natural frequencies and mode shapes were shown to be reliable damage indicator, whereas damping ratios were inaccurate or insensitive for damage detection. Because it is usually not known in advance which features is more sensitive to damage, it was suggested to use a high-dimensional feature vector, and then simplified with PCA. The environmental uncertainty was not addressed in this research.

The research work carried out by Sun and Chang (2004) indicated that wavelet packet transform (WPT) has the ability of extracting minute abnormality from vibration signals. As a demonstration, an experimental study on a steel cantilever I beam under a repeated pulse force was performed. Four damage cases, involving line cuts of different severities in the flanges at one cross section, are introduced. The structural performance data were recorded by accelerometers installed at the free end of the beam. Two damage indicators (e.g. sum of absolute difference (SAD) and square sum of difference (SSD)) were studied; the x-bar control chart analysis results indicated that both of them are sensitive to damage and yet insensitive to noise. In this research, the trend of the damage induced change was known in advance, so only one side control limits was used in the control chart construction. The experimental study did not consider the possible excitation and environmental variance.

2.3.2 Applying Control Chart Analysis after the Elimination of Temperature Effect

Most of the control-chart based damaged detection approaches reviewed above using the dynamic features of a structure as the damage indicator. In practical application, the temperature effect,

which is the most frequently reported environmental factor that influence the dynamic properties of civil structures, has to be eliminated, otherwise, it can mask the structural damage easily. Much research has been carried out to address the temperature effect issue while using control chart as the data analysis tool to determine the occurrence of damages. These efforts are summarized in the following.

In the work conducted by Kuallaa (2003), factor analysis technique was used to eliminate the temperature effect without the requirement of measuring the temperature. Schewart control charts were employed to verify the effectiveness of the proposed method using simulation data which resembled the observations of the Z24 Bridge. Although this work was carried out to find a solution to address the issue of temperature induced structural response variations, the results proved the effectiveness of using control chart in damage detection as well.

Also to address the damage detection problem under varying temperatures, Yan and et al (2005) proposed a PCA based method. Two examples were employed to verify the method: 1) A 3-span bridge simulated by 32 beam elements. Damages were introduced by reduce the stiffness of selected elements. 2) A wooden bridge. Artificial damages were created by adding different lumped masses. The natural frequencies were chosen as the damage indicator. PCA was first applied to the vibration features in reference state to capture the temperature effect. Using the established model, the residual error of the prediction of current feature remains small if no damage happens. On the other hand, if damage occurs, significant residual increase can be seen from the control chart analysis. This method is very straightforward and verified to be powerful by the examples.

The first problem (A 3-span bridge simulated by 32 beam finite elements) solved in the previous work was further studied by Deraemaeke and et al (2008). Damage indicators, including: 1) natural frequencies; 2) mode shapes; 3) peak indictors extracted from the output of Fourier transform of modal filters, were compared. The effects of temperature are treated using the factor analysis technique. Multivariate Shewart-T control charts were employed as the data analysis tool to determine the damages. Results indicated that when no noise present in the measurement, the features can be ranked in terms of increasing damage sensitivity: natural frequencies, lower order mode shapes, higher order model shapes, and the peak indictor extracted from the model filters. However, when noises exist, mode shapes are ideal damage indictor.

2.3.3 Summary

The researches reviewed above all concluded that Schewart control chart is a possible statistical analysis tool that can be used to solve the structural damage detection problem. It has been revealed that the selection of damage indicator and the elimination of environmental effect are essential for the damage sensitivities. The frame work of applying control charts in damage detection was established by these efforts. The control chart based damage detection approach is attractive for the development of an automated continuous monitoring system because of its simplicity, less interaction with users, and no analysis model was involved. However, most of these efforts are based on data obtained from controlled lab testing and/or finite element analysis. When applied in long term field monitoring, many improvements must still be made. First, the excitation variance induced structural response change may be significant, especially when the collected data were used directly without converting to structural dynamic features. None of these efforts addressed the damage location detection problem, and none of the reviewed work has successfully applied the control chart based damage detection approach with strain data. Being aware of the advantages of control chart based damage detection approach and the limitations of existing efforts, a strain based damage detection approach was developed at the BEC (Doornink, 2006) using the concept of control chart. As mentioned before, it is the foundation for the work described in this thesis. Important details of this work are reviewed in the following.

2.4 The Strain Based Damage Detection Method Developed in BEC

Upon the request of Iowa DOT, the BEC developed a long term SHM system for two-girder fracture-critical bridges in 2006. As a demonstration, the system was installed at the US 30 south skunk bridge. Forty fiber optic strain sensors were installed along the bridge framing system to collect the response strains resulting from ambient traffics. The major objective of this system is to detect the formation of fatigue cracks in the girder web cut-back areas. Sensors that were installed in the damage prone areas were named TS (Target Sensor) and other sensors are named NTS (Non Target Sensor). The strain data collected by all the sensors are first zeroed and filtered to remove the temperature effects and dynamic effects, and then, the maximum or minimum strains were roughly detected for each vehicle event. With the extreme strains, match relationships can be developed between TSs and NTSs with training data sets. An example of such match relationships is shown in Fig. 2. 2a.

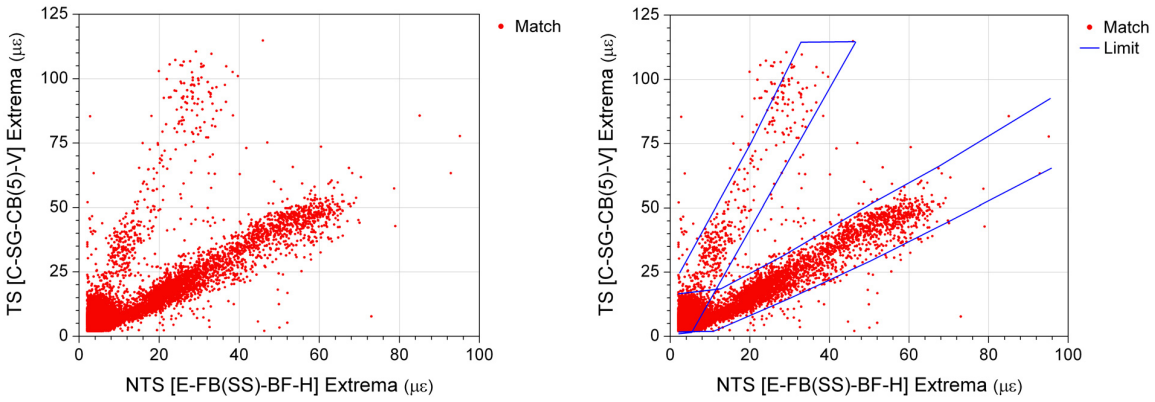

a. one example of the match relationships b. control limits for the match relationship

Figure 2.2 A typical example of the match relationship and the control limits

Among the 1200 possible match relationships, 415 were considered to be useful and further evaluated to determine damage occurrence. The baseline performance of the bridge was defined through the upper and lower control limits similar to those used by control chart analysis. In this work, the limits were defined manually. Figure 2.2b illustrates the control limits for the match relationship shown in Fig. 2.2a.

After the match relationships and control limits were established, they are used to evaluate the data obtained from an unknown structural state. During the evaluation, the match relationships were created and compared with the control limits. Data within the control limits were assessed as “Pass”, otherwise, they were assessed as “Fail”. For each event, the relationship pass percentage (RPP) was calculated for each TS using Eq2.1. At the end of a specified evaluation period, the RPP assessments are summarized in histograms. An example of the histograms is shown in Fig. 2.3a. The structural damage occurrence was expected to be evidently shown in the histogram. The expected histogram change caused by structural damage is shown in Fig. 2.3b.

$$RPP\ (\%) = \frac{Number\ of\ "pass"assessments}{Total\ number\ of\ assessments}(100) \qquad \text{Eq. 2.1}$$

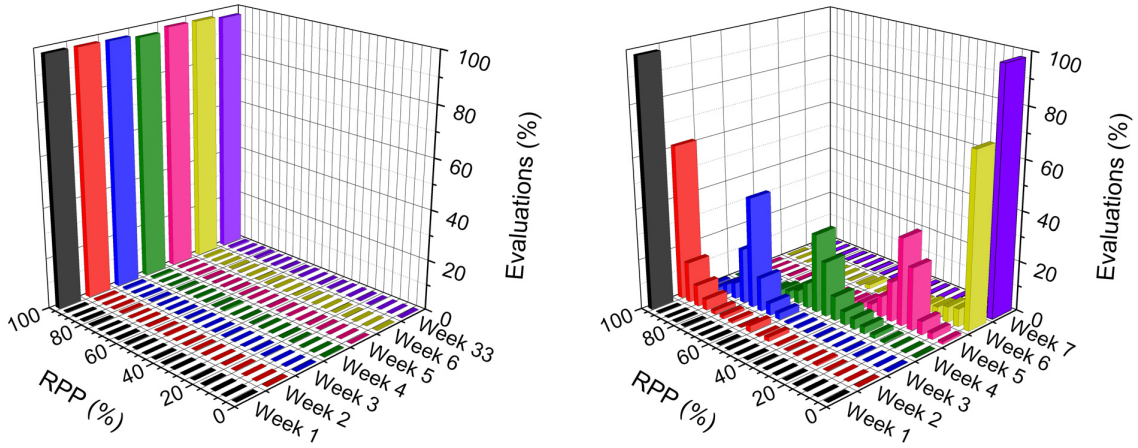

a. RPP histogram for undamaged structure

b. Expected RPP histogram for damaged structure

Figure 2.3 Example of the RPP histogram

This system enables bridge owners to remotely monitor bridges for damage formation in the damage prone areas. The strain-based SHM system is trained with measured performance data to identify typical bridge responses when subjected to ambient traffic loads, and the knowledge that is learned during the training is used to evaluate newly collected data. Evaluation reports can be generated automatically at specified intervals. The system is probably the most sophisticated strain-based SHM system that can be found in the literature. However, reviewing of this system, many limitations can still be found:

1) The manually defined control limits are subjective, with which, the false alarm rate is hard to control. In addition, the required personal interaction prevented the training procedure to be realized automatically.
2) The final structural performance report was generated in the format of the RPP histogram. It does not show the damage directly, further knowledge based interpretation of the report is necessary.
3) The extreme strain values used in the evaluation were not based on an exact vehicular event detection results. Therefore, the matches could be created between points that were not produced by the same vehicle.
4) All the strain peaks were used in the evaluation. The different relationship patterns resulting from the different load conditions can reduce the damage sensitivity of the method.
5) To apply the system, the damage prone areas have to be known in advance.

6) No verification was performed for the proposed damage detection algorithm.

To address these limitations, a new strain-based damage detection approach was proposed in this work.

CHAPTER 3 SHM SYSTEM HARDWARE AND DEMONSTRATION BRIDGE

The basic SHM hardware installed at the US Highway 30 (US30) bridge during previous research was used in this project after integrating additional sensors. Figure3.1 illustrates the general configuration of the SHM system hardware. The bridge site components (i.e. those components residing at the bridge) consist of a strategically deployed fiber Bragg grating (FBG) strain sensor network and the data collection, analysis and management components which includes: Micron Optical Si425-500 interrogator, a Linksys router, and a desktop computer. The interrogator, computer, and router were located in an environmentally controlled cabinet. The data collected by sensors and interrogator are relayed through the router to the computer where they are temporarily stored and immediately processed. The processed results can be sent back to the remote office computer through the long range antennas.

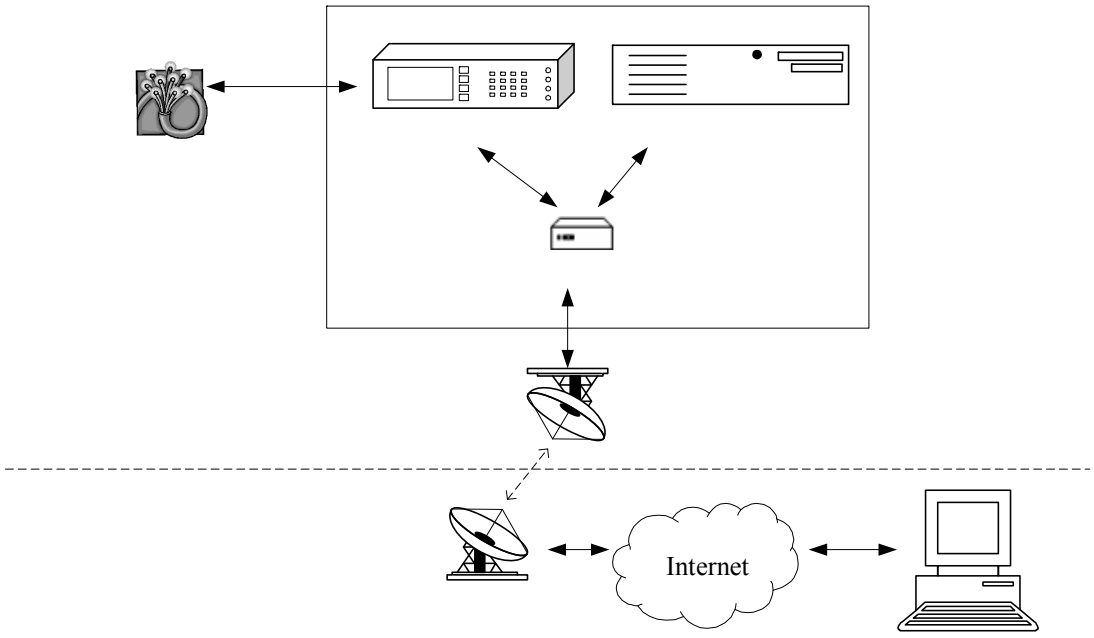

Figure 3.1 Schematic of the SHM system

Details about the demonstration bridge, the sensor network and the communication network are discussed in the remaining part of the chapter. In some cases further information may be found in Chapter 4.

3.1 Demonstration Bridge

3.1.1 General Information

The US Highway 30 (US30) bridge crossing the South Skunk River near Ames, IA (Fig. 3.2) was selected to demonstrate the developed SHM system primarily because this work built on work previously completed. The three-span 320ft long 30 ft wide bridge carries two east bound traffic lanes with a posted speed limit of 65mph. The 7.25in thick cast-in-place reinforced concrete slab deck is supported by a framing system consisting of two stringers, 19 floor beams, and two welded plate girders. The plate girders are continuous over the three spans (97'-6" end spans and a 125'-0" main span), while the stringers are continuous over the floor beams. Figure 3.3 illustrates the layout, typical cross section and the size of the structural components of the bridge. The girder flanges taper from 28"×1.5" to 13"×1.5" within the negative moment region (Fig. 3.3-1c) and the girders are spliced at locations 30ft from both piers. The bridge supports were designed to be roller at both abutments and at the east pier and pined supported at west pier. The abutments are stub reinforced concrete and the piers are monolithic concrete.

a. Side view b. Bottom view

Figure 3.2 US30 South Skunk Bridge

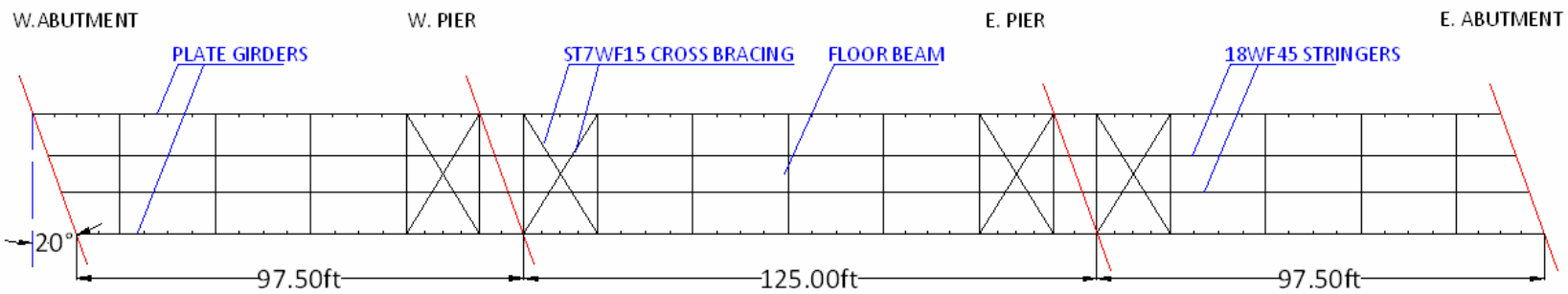

a. Layout

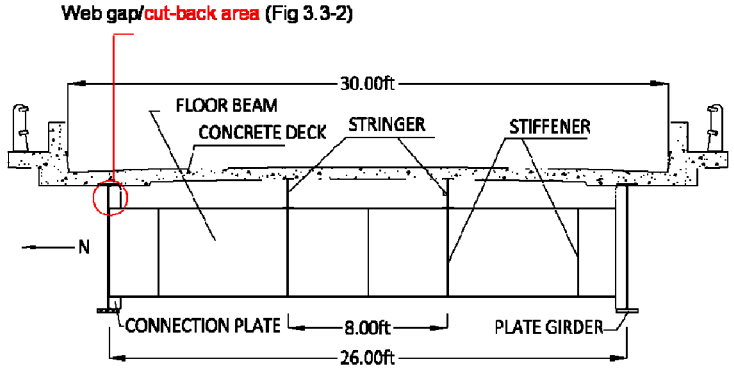

b. Typical cross section

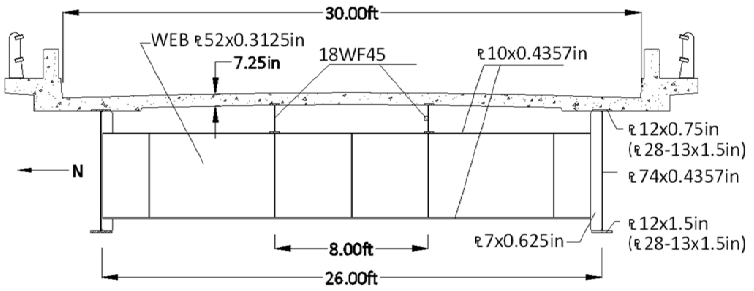

c. Sizes of structural components

Figure 3.3-1 Layout and cross section of US30 bridge

3.1.2 Fatigue Damage in the Cut Back Regions

Under traffic loads, the vertical deflections of adjacent girders are different (primarily due to the bridge skew), which in turn leads to an overall rotation of the floor-beams. As shown in Fig. 3.3-2a, the web stiffener was not welded to the girder top flange and as such, it is able to rotate with the floor beam. However, due to the concrete deck the top un-stiffened portion of the girder web is constrained from free rotation, and thus, a double curvature out-of-plane distortion is produced in the small segment of the web between the top flange and the top of the connection plate (Fig. 3.3-2 b). As a result, the web gap region experiences high stress levels under traffic loading which can result in the development of fatigue cracks. This type of out-of-plane induced fatigue damages has been found in many welded plate steel bridges at locations where transverse structural members are connected to the longitudinal girders (Fisher 1984; Roddis 2003). As a retrofit on the bridges of this type in Iowa, the connection plates were cut back (Fig. 3.3-2c) to reduce the out-of-plane bending stresses. The retrofit slowed but did not completely eliminate the development of fatigue damage at the cut back areas. The desire to detect this damage is what led to the work previously completed and that described herein.

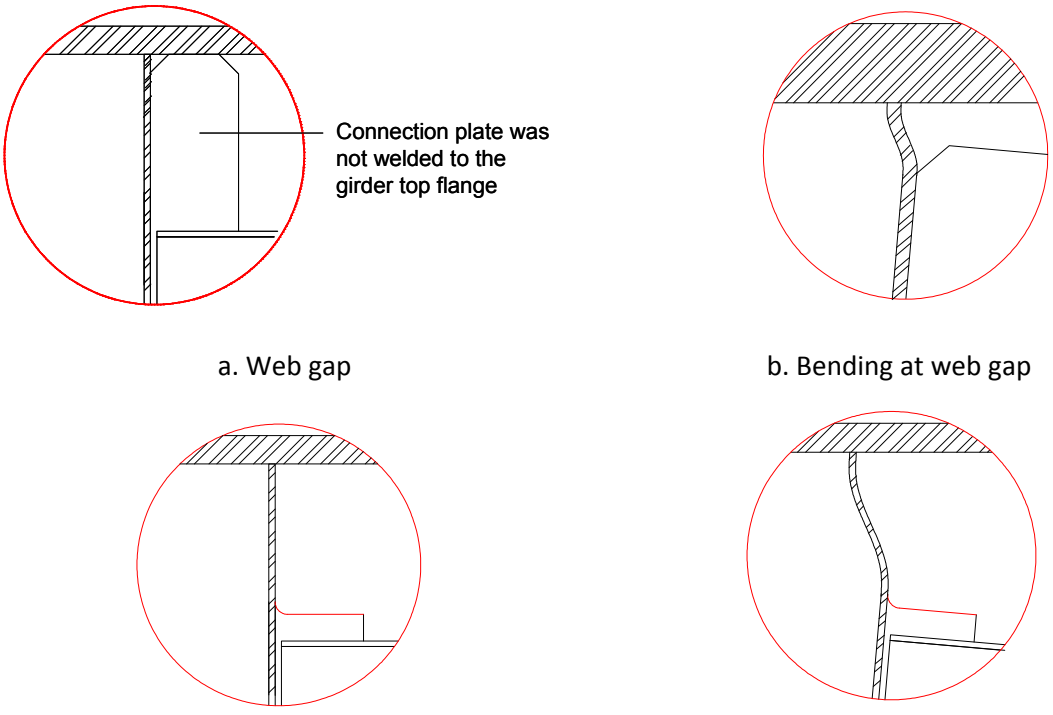

a. Web gap

b. Bending at web gap

c. Cut-back area

d. Bending at cut-back area

Figure 3.3-2 The web gap and cut-back area details and out-of-plate bending

3.2 Fiber Optic Sensor Network

3.2.1 Sensor Selection and Installation

The developed SHM system utilizes FBG sensors to collect performance and live load data. Fiber optic sensors (FOS) out perform other strain transducers in long term application due to their ability to multiplex, sensor stability, and longevity in harsh environments (Schulz 1998). Previous SHM research (Wipf 2006) and laboratory testing conducted by the BEC demonstrated the long term performance and reliability of surface mountable sensors (SMS), and they were used in this project as well. Figure 3.4 is a photograph of a 10mm FGB, which is embedded in a $210 \times 20 \times 1mm$ CFRP package. The packaging protects the sensor and provides more surface bonding. The fiber pigtails exiting from each side of the packaging (entry fiber and exit fiber) consist of SMF simplex cable (3mm jacketing) and FC/APC mechanical connectors. The built in FC/APC connectors of the standard FGB packages provided a convenient way to connect the sensors in series. Figure 3.5 presents the typical FC/APC mechanical connections and how they were connected via a mating sleeve. In this project, adjacent FGBs within one series were selected to have a 5nm center wavelength separation to allow for an adequate strain range. Detailed sensor specifications can be found in Appendix C.

The standard FBGs (10mm long) are sufficient for strain data collection at locations where strain fields are relatively uniform. However, for locations with complicated strain fields, shorter sensors are needed. The complicated non-uniform strain field at cut back regions, which result from the previously described reverse curvature condition, were measured by two special designed 5mm FBG packages: 1) Single 5mm FBG in a 15×20×1mm small form factor CFRP packaging; 2) an array of five 5mm FGB embedded in a single 220×20×1mm CFRP package.

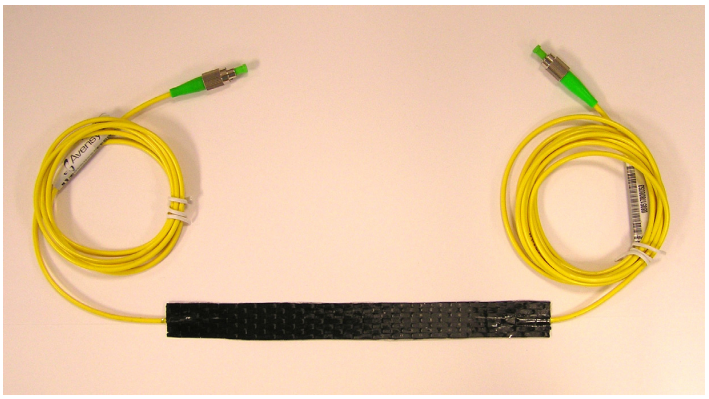

Figure 3.3 The standard FBG SMS

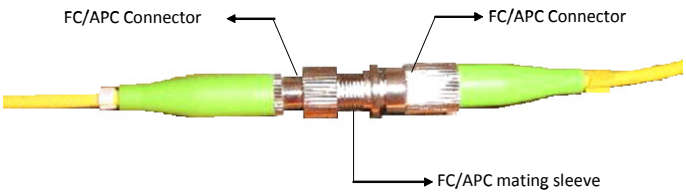

Figure 3.5 FC/APC mating sleeve connecting two fibers

The 40 existing Fiber Bragg Grating (FBG) strain sensors distributed along the bridge framing system including the girders, floor beams and stringers were employed to monitor the performance of the bridge. Additionally, eight new strain sensors were installed at the bottom surface of the concrete deck to obtain the live load condition information.

3.2.2 Layout of the Sensor Network

3.2.2.1 Existing Sensors

The 40 previously installed FBG sensors were distributed in six cross sections (indentified as Section A through F in Fig. 3.6). These sensors can be classified into two categories according to the sensor orientation:

1) Horizontal: bottom flanges of girders within positive (Section A, Section B, Section D, and Section F) and negative(Section C and Section E) moment regions, stringers, and floor beams;
2) Vertical: cut-back regions and stringer webs above floor beams support points.

Figure 3.7 presents the locations and orientations of the sensors at each section. To be consistent, the sensor naming convention was inherited from previous work. Each sensor is named in the format: Section-Member-Part-Orientation, in which, Section can be “A” to “F”; descriptions of Member, Part and Orientation are listed in Table 3.1. For example, B-SG-BF-H means Section B south girder bottom flange horizontal sensor.

Table 3.1 Name convention for sensors located at the bridge frame system

Member	Description	**Part**	Description	**Orientation**	Description
NG/SG	North Girder /South girder	BF	Bottom flange	H	Horizontal
NS/SS	North Stringer /South stringer	CB	Cut-back region	V	Vertical
FB	Floor Beam	WB	Web		

3.2.2.2 New Deck-Bottom Sensors

Two lines of deck-bottom sensors (10mm FBG strain sensor with the $210 \times 20 \times 1mm$ FRP packaging) were installed at Section A and the section above the fifth floor beam. The longitudinal and transverse locations of the sensors are illustrated by Fig. 3.6 and Fig. 3.8, respectively.

3.3 Communication Network Configuration

Figure 3.10 illustrates the communication networking topology and configurations of the SHM system. The bridge site subnet managed by the Linksys router enables data communication between the interrogator and the bridge site computer. Using long-range antennas and the accompanying radio modems, the bridge site subnet was connected to the CTRE network wirelessly. As shown in Fig. 3.10, two radios were involved in this system, the remote one was connected to the LinkSYS router while the master radio was connected to the CTRE internet switch. Each was assigned with a fixed public IP address. Information is transferred via electromagnetic energy radiated by one antenna and received by the second. This setup provides internet access for the bridge site computer and, thus, enabled data communication between the bridge-site computer and any other internet accessible computer.

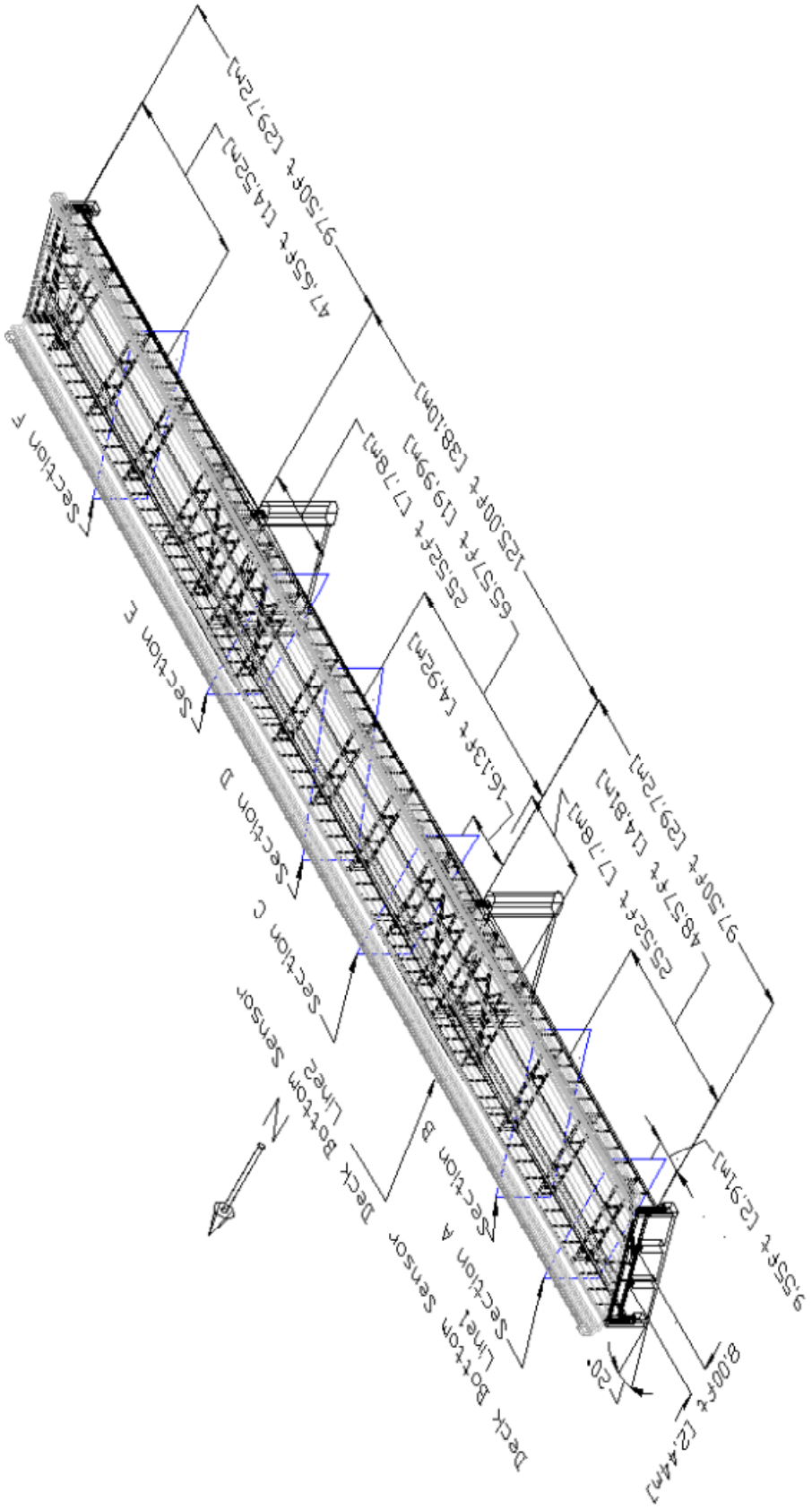

Figure 3.6 FOS longitudinal positions

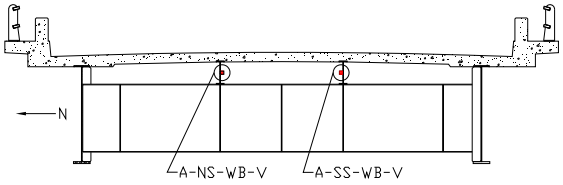

a. Section A

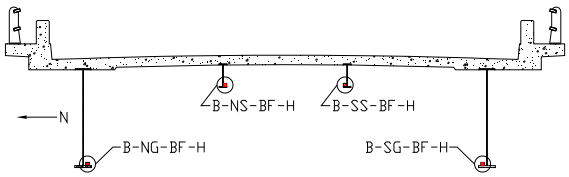

b. Section B

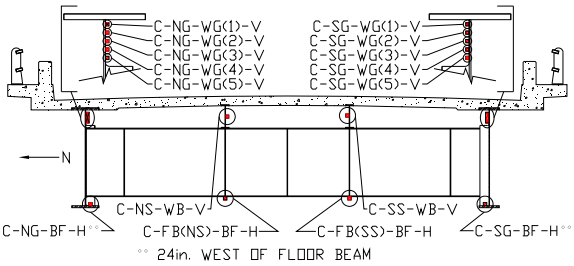

c. Section C

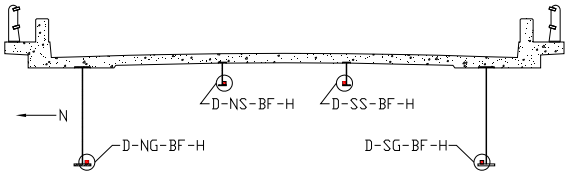

d. Section D

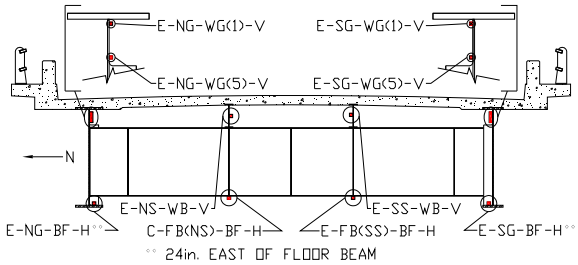

e. Section E

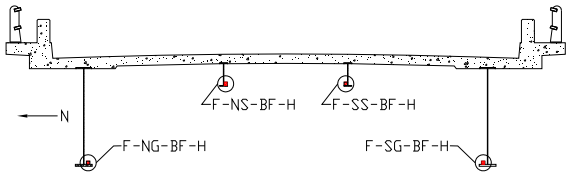

f. Section F

Figure 3.7 Sensors located at the bridge frame system

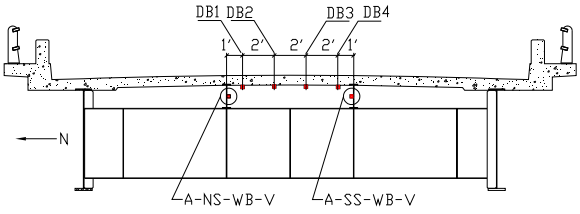

a. The first line of the deck-bottom sensors

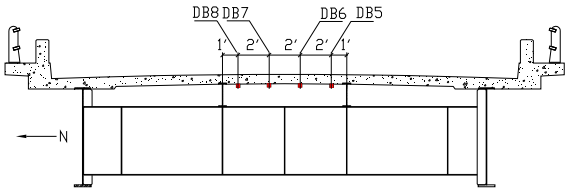

b. The second line of the deck-bottom sensors

Figure 3.8 Sensors located at the bridge deck bottom

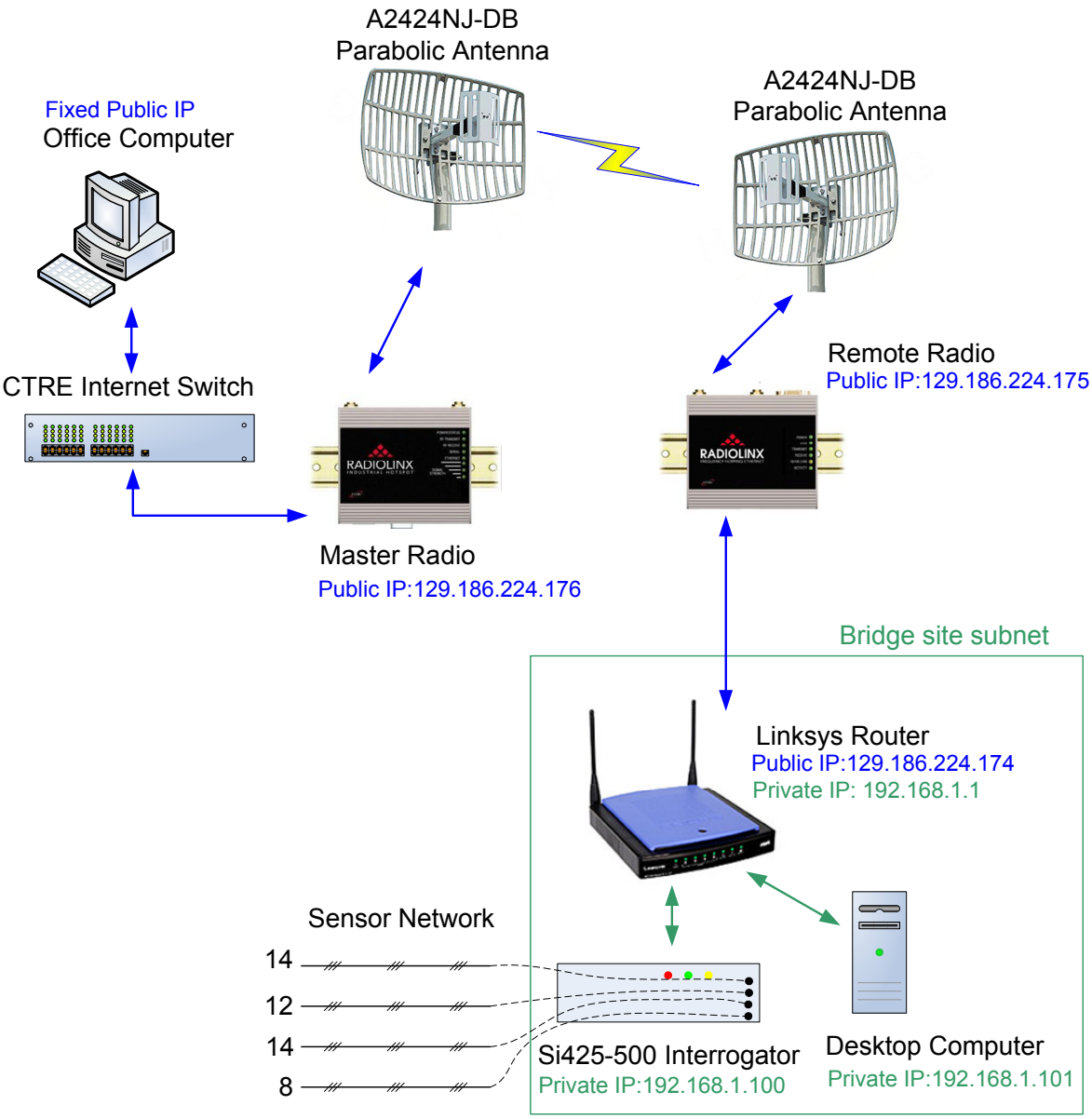

Figure 3.9 The networking setup and IP configuration of the SHM system

CHAPTER 4 DATA PREPROCESSING

During normal operation, highway bridges are subjected to many changing environmental and operational conditions that can impact measured structural performance metrics. If the variances caused by these conditions are not properly addressed, they can either mask the subtle changes caused by structural damage and reduce the sensitivity of the damage detection approach or result in undesirable false alarms.

Three major environmental and operational factors were identified and addressed to improve the sensitivity of the developed damage detection algorithm. First, an effective temperature effect remove algorithm created in previous related research was used in this work (Doornink 2006). Secondly, the dynamic effects caused by truck vibration and its interaction with the bridge can cause significant uncertainty in the collected strain data. Using a pseudo static strain response instead of the original data is an effective way to reduce the variances, and it was realized through specially designed digital filters (Doornink 2006). In addition, variations in bridge response to a variety of vehicle configurations were also found to be a significant source of uncertainty. To address this, a strain-based truck parameter detection algorithm, which enabled further data selection, was developed in this research. Using data from select truck load conditions can reduce strain variances significantly. The developed data selection procedure also fulfilled the function of extracting the most useful information from the original data.

Truck parameters that affect strain measurements were identified through observations and basic structured engineering concepts. Figure 4.1 illustrates a typical example of such strain relationships. The horizontal axis represents the maximum event strain of a girder bottom sensor, and the vertical axis is the minimum event strain of a sensor located at the cut-back area. Two obvious groups can be identified from the data points. The one with fewer points was thought to represent left lane events (i.e. those with the vehicle in the left lane), while the other one represents right lane events (i.e. those with the vehicle in the right lane). The remaining points which do not appear to belong to the lane groups may have resulted from concurrent truck events (i.e. two or more vehicles on the bridge) or truck lane switching (i.e. a vehicle changes lane while on the bridge). These patterns indicate that the transverse truck position affects the strain relationships. Additionally, slight

deviations of the relationship can be observed within each lane group (i.e. it is not perfectly linear). They can be likely attributed to different truck weights and geometry combinations. In short, truck parameters including travel lane, number of axles, axle spacings, and truck weight were considered to be important for the extreme event strain relationship and, thus, needed to be detected/ calculated. To avoid confusion in the following discussion it should be pointed out that the calculation of axle spacings requires the truck speed be known; so truck speed is also included in the developed truck parameter detection approach.

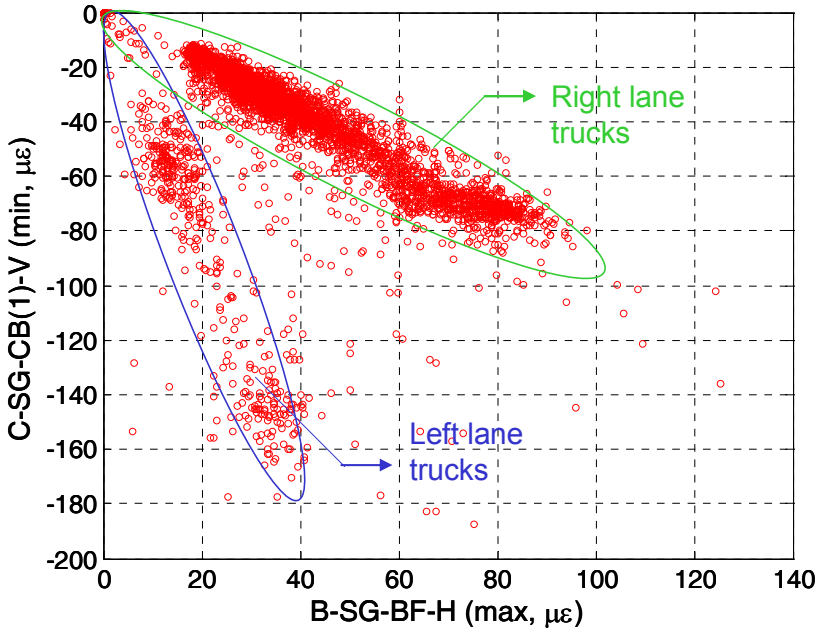

Figure 4.1 An example of the extreme event strain relations for two selected sensors

In summary, a three step data preprocessing procedure was developed in this work to separate the strain changes caused by operational (e.g. truck parameters and bridge parameters) and environmental (e.g. temperature) variances from the interested structural changes.

Step 1, remove the temperature induce strain through a process referred to as data zeroing.

Step 2, remove the dynamic strain response with lowpass frequency digital filters, which are unique to each sensor.

Step 3, remove the strain variance caused by different live load conditions through data selection. In particular, data produced by only right lane, five-axle, trucks were selected to feed into the damage detection procedure.

Details of the data zeroing, data filtering, and data selection procedures are described in the following sections.

4.1 Data Zeroing

For highway bridges the mechanical strains resulting from ambient traffic loadings have much higher frequencies than temperature-induced strains. Thus, it can be assumed that the temperature change within a sufficiently short time period is neglectable. Therefore, by segmenting the monitoring data into small size files, a constant baseline thermal strain can be determined in each file for each sensor. Previous research (Doornink 2006) showed that segments of data collected every 27 seconds are sufficient to ensure the correctness of the assumption for all sensors.

The baseline thermal strain (i.e. the offset from zero strain) for each sensor was determined by finding the mode from each data segment. In statistics, the mode is defined as the value that occurs the most frequently in a data set or a probability distribution. However, when the data contains noise, it is more practical to take the mode as the center value of the histogram bin that contains the most values. In practice, it is difficult, if not impossible, to find a predetermined bin size that would be successful for every strain record. Therefore, instead of using a fixed bin size, an iterative approach was used to calculate a satisfactory mode value. After all baselines have been established, the raw data for each sensor are zeroed by subtracting the baseline strain from each strain value in the raw data. In this way the zeroed data consists of only the mechanical strains and noise. For example, as shown in Fig. 4.2, the green line represents the raw strain data for sensor B-SG-BF-H obtained from a right lane truck event. The zeroed data were computed by subtracting the mode value (136 $\mu\varepsilon$) from each data point of the raw data.

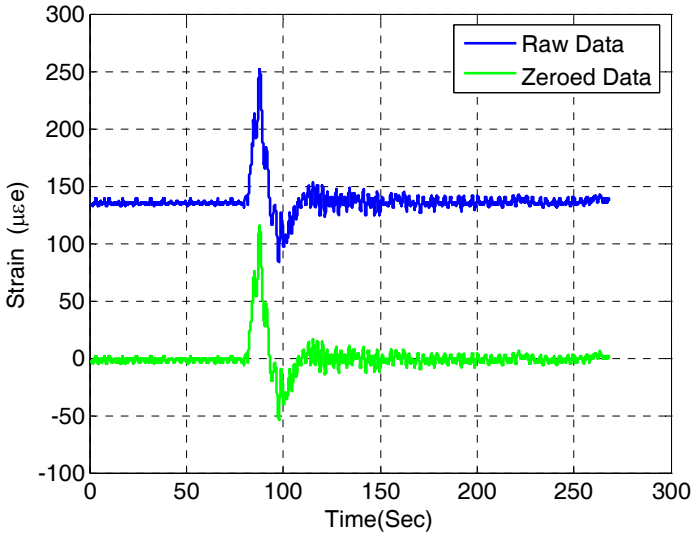

Figure 4.2 An example of raw data and zeroed data

4.2 Data Filtering

The zeroed data still contains three components: 1) quasi-static strain response, 2) dynamic effects, and 3) noise. Among the three components, only the quasi-static strain is the desirable part for this work. The frequencies of dynamic effects are much higher than that of the quasi-static strain response, so appropriately designed lowpass digital filters can be applied to remove the dynamic effects and some high frequency noise.

The Chebyshev filter was considered to be superior to other filters due to its ability to minimize peak detection error while using relatively less processing time. To determine the frequencies of the quasi-static events for each sensor, a one hour data set that was collected during dense traffic was investigated. A Fast Fourier Transform (FFT) was used to generate a power spectral density (PSD) plot for each sensor. As an example presented in Fig. 4.3 is the PSD plot for sensor B-SG-BF-H. As marked in the figure, the frequency of the quasi-static response has been identified as well as the fundamental frequency. It can be seen that the quasi-static response of vehicular event has lower frequency but larger contribution than the natural frequency of the bridge. Although this phenomenon can be observed in all sensors, PSD plots are different for each and, as a result, the design of the filter for each sensor was different. In particular, the quasi-static frequency of each sensor is selected as the cut-off frequency of the corresponding filter. The passband allowable error (PAE) was set to 1% for all filters and the passband ripple was calculated as follows:

$$ripple\ (\text{dB}) = \left| 20 \times \log\left(\frac{100 - PAE}{100} \right) \right|$$

Owing to the noise contained in the zeroed strain data, the filtered data often has slight offset from zero. To adjust the baseline point to zero, the data zeroing procedure was carried out again to complete the data filtering.

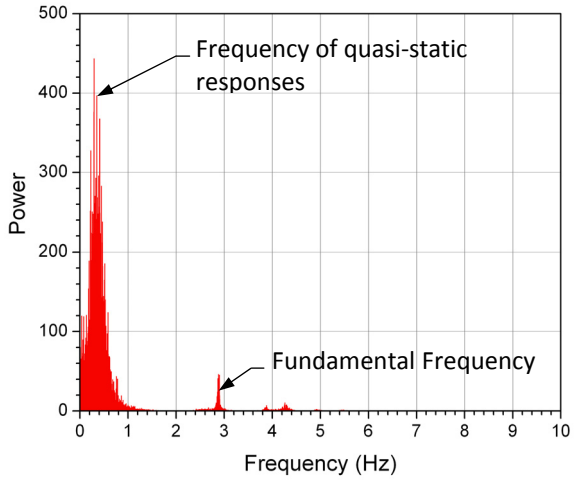

Figure 4.3 An example of PSD plot

Figure 4.4 presents the filtered strain for the data used to create Fig. 4.3. To obtain the quasi-static response sketched in Fig. 4.4, the parameters of the Chebyshev filter were set as the follows: the cutoff frequency equal to 0.35Hz, and Passband Ripple is 0.0873dB. The filtered data are plotted in red. The smoothness of the line indicates that most dynamic effects and high frequency noise were removed. Due to the nature of the digital filter, the filtered data shows a phase delay from the original data. Compensations for the phase shift in SHM are widely discussed in the literature (Fraser 2006, Wang 2006). In the proposed damage detection approach, since only the event strain peaks are needed, the shift can be simply ignored without impacting the overall results.

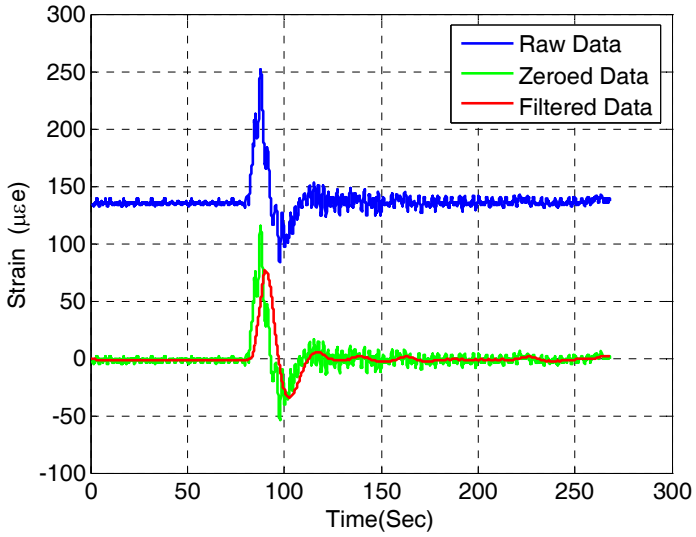

Figure 4.4 An example of raw data, zeroed data, and filtered data

4.3 Truck Parameter Detection

For highway bridges, it usually is difficult to distinguish between the response changes caused by the variability in ambient live load conditions (e.g. truck weight, geometry, etc) and those induced by structural damage. In this work, two approaches were deployed to reduce the live load condition induced variability. First, utilizing a strategically defined damage indicator (discussed in Chapter 5); secondly, including truck parameters into the base-line model. Specifically with regarding to the truck parameters, only the strain data that are produced by select truck load conditions are utilized in the damage detection procedure. To realize the data selection, a strain based truck parameter detection sub-system was developed. The sub-system can detect/calculate/estimate the relevant truck parameters, which include the travel lane, number of axles, speed, axle spacings, event start and end times, and truck weight group.

When the work described here was initiated, forty FOSs installed on the demonstration bridge (girders, floor-beams, and stringers) existed already. It would have, thus, been ideal if some of those sensors could be utilized in the truck parameter detection sub-system. In this way, the strain patterns of the sensors were studied, and the results revealed that the girder bottom sensors are capable of detecting truck event and the travel lane. However, none of the existing sensors could collect enough information about the truck axles, which is a key parameter to calculate all other parameters. Therefore, new sensors were needed. Figure 4.5 represents the conceptual live load transfer path of the demonstration bridge. The deck system collects the traffic loads and distributes

most of the load to the stringers with very little transferred to the girders directly. The stringers pass the loads to the floor beams and eventually to the girders. Finally, through the girders, all forces are transferred to the bearings that are supported by the abutments and/or piers. In general, structural components located at the bottom of the load path show more globalized character in their strain response. The strain responses of these components are more relevant to truck GVW (gross vehicle weight) and travel lane than truck geometry configuration. On the other hand, the structural components located at the top of the load path show a more localized strain response pattern due to their vicinity to the load. Therefore, the deck bottom sensors were considered to be a possible option for the truck axle detection. Previous experiences had shown this to be true. To further verify the effectiveness of the deck bottom sensors and determine their proper locations and orientations, FEA and controlled load tests were carried out before installation of additional FOSs.

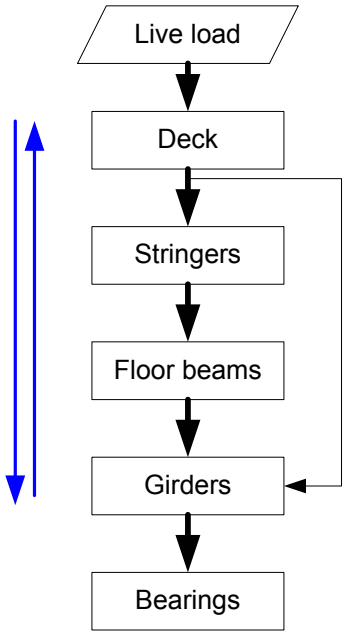

Figure 4.5 Load path of the demonstration bridge

4.3.1 Sensors Employed for Truck Parameter Detection

Although many existing commercial systems can detect the truck axles, traveling lanes, and truck weight, they are either very expensive or can not be practically integrated into the existing FOS-based strain monitoring system. Further, the synchronization of components in a heterogeneous system is difficult especially when the monitoring is time sensitive. To address these issues, a pure

FOS strain based truck parameter detection subsystem was developed and integrated into the existing system.

Determining truck parameters from strain data is a reverse problem. Solving a reverse problem is hard, in general. However, the solution can be dramatically simplified if a one-to-one mapping between the variables and responses can be established. In this research, efforts were carried out to search for such mapping between the strains and the object truck parameters. Both the existing sensors and new sensors were studied.

4.3.1.1 Existing Sensor Study

The originally installed sensors can be classified into four categories: girder bottom sensors, floor beams sensors, and horizontal and vertical stringer sensors. In Fig. 4.6, an example of the strains produced by a five-axle semi truck (Fig. 4.6a) and a dump truck (Fig. 4.6b), both in the right lane, are shown for four selected sensors: B-SG-BF-H, B-SS-BF-H, C-FB(SS)-BF-H, C-SS-WB-V. These sensors represent typical behaviors for the four sensor categories. Comparing Fig. 4.6c with Fig. 4.6d, the strains produced by the semi and the dump truck show the same general pattern for the girder bottom sensor B-SG-BF-H, which is located at the middle of the first south girder span. The “Positive peak 1” occurred when the truck was in the same span as the sensor, while the “Positive peak 2” occurred when the truck was travelling in the third span. The magnitude of the first peak is significantly larger than the second peak. Therefore, by properly selecting a peak magnitude threshold, only one peak would be detected, and such, a one-to-one mapping can be established between a positive strain peak and a truck event.

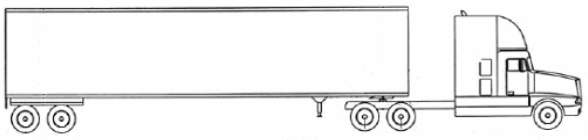

a. 5-axle semi truck

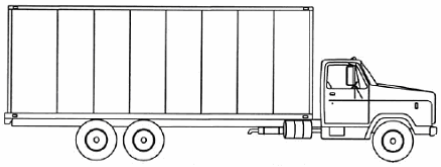

b. dump truck

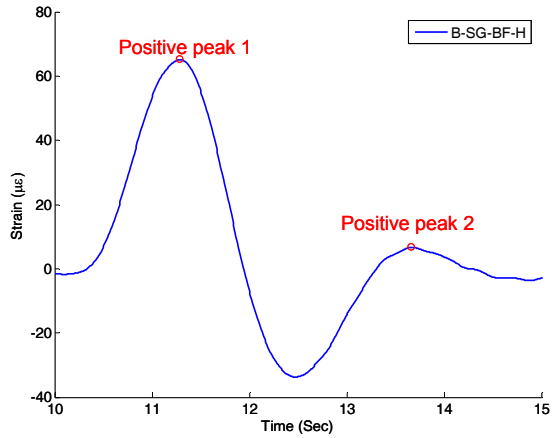

c. Strain at mid-girder-bottom (5-axle semi truck)

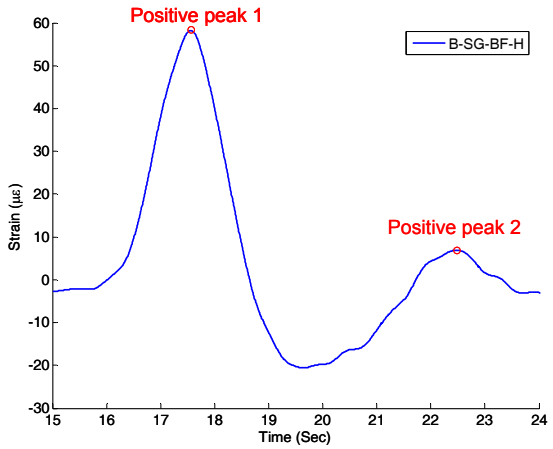

d. Strain at mid-girder-bottom (dump truck)

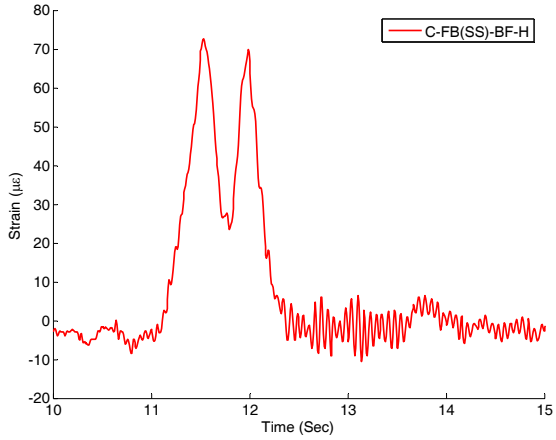

e. Strain of floor-beam (5-axle semi truck)

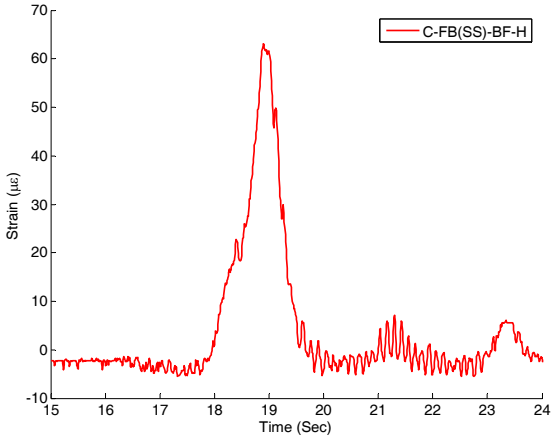

f. Strain of floor-beam (dump truck)

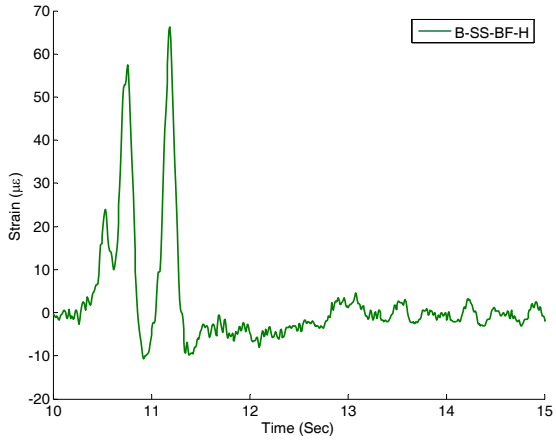

g. Horizontal strain of stringer (5-axle semi truck)

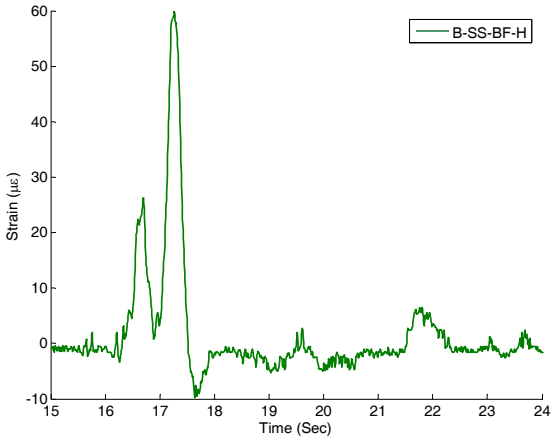

h. Horizontal strain of stringer (dump truck)

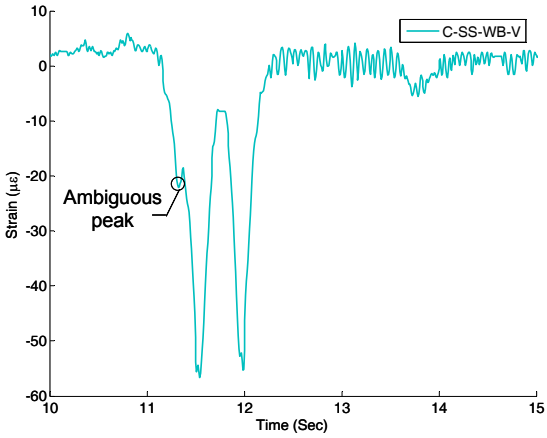

i. Vertical strain of stringer (5-axle semi truck)

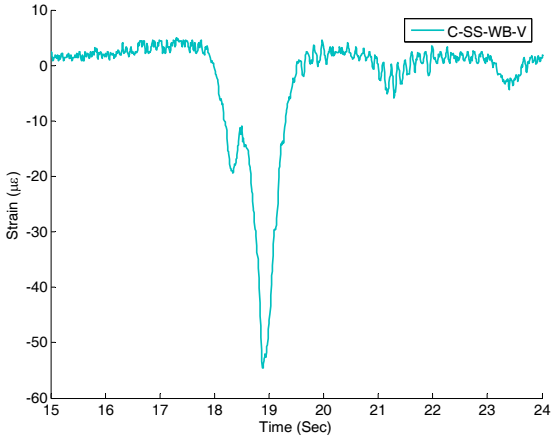

j. Vertical strain of stringer (dump truck)

Figure 4.6 Strain patterns for the frame sensors produced by five-axle semi and dump trucks

In terms of truck axle detection, the strain patterns for the floor beam sensors and the stringer sensors were studied. In Fig. 4.6e, the two peaks shown in the strain of the floor beam sensor C-FB(SS)-BF-H represent the two tandem groups of the five-axle truck. Similarly, the only peak produced by the tandem group of the dump truck was shown in Fig. 4.6f. In both cases, the floor beam sensor failed to detect the steering axle, and the axles within an axle group can not be differentiated from one another.

Comparing the horizontal (Figs. 4.6e and 4.6f) and vertical (Figs. 4.6i and 4.6j) stringer sensors, it can be seen that both can detect not only the tandem groups but also the steering axle. Figure 4.6i presents the strain produced by the five-axle truck and recorded by the vertical stringer sensor C-SS-WB-V. Implementing an algorithm that can ensure the detection and differentiation of such peaks is, if not impossible, very hard. On contrast, the strains for the horizontal sensor (B-SS-BF-H) rarely include such ambiguous peaks. Therefore, among the existing sensors, the horizontal stringer sensors collected the most information about the truck geometry. Nevertheless, the differentiation of axles within an axle group was still believed to be hard to achieve.

4.3.1.2 New Sensor Investigation and Installation

Since no existing sensor can easily satisfy truck axle detection needs, studies were performed to determine the positions and orientations of new sensors. Attached to the most localized structural component, deck bottom sensors should be able to collect more information about truck axles. FEA

and control load tests were carried out to verify the effectiveness and determine the proper locations and orientations of the sensors.

4.3.1.2.1 Finite Element Analysis

A FEA was carried out to identify the correlation between the deck-bottom strain peaks and the truck axles. A three-dimensional finite element model was constructed for the demonstration bridge using the ANSYS software package. The steel frame of the bridge model is shown in Fig. 4.7(a). Figure 4.7 (b) shows a typical cross section including the steel frame, deck, and barrier system. The entire model contains approximately 79,423 active nodes and 72,811 elements. With the exception of the cross braces, two-dimensional quadratic shell elements were used to model all steel and concrete All elements were placed at the centerline of the true geometric positions, so gaps, such as the one between the curb and deck shown in Fig. 4.7b, can be formed between actually connected components. Rigid links were used to connect such components. They were also used to connect the deck elements to the girder and stringer elements to simulate composite action. The boundary conditions were modeled to simulate the bridge support conditions. The entire width of the girders bottom flanges are restrained in all three degree of translation freedom (pinned support) at the east pier; longitudinal movement is allowed (roller supported) at the abutments and west pier.

In practice, strain peaks produced by a truck crossing over can be captured only when the truck speed is low or the data collection frequency is high. In either case, the ratio of move-distance/load-step should be sufficiently small. In this study, for simulation simplicity, the single truck passing over the bridge was simulated to be moving wheel forces which were always applied to nodes directly. Owing to this simulation approach, the value of move-distance/load-step is controlled by the size of deck element along the traffic direction. A finer mesh ensured better peak capture results at the cost of computation resources. As a compromise, the deck mesh size was selected to be 6 in.×6 in. . So for each load step, the truck position could move in increments of six inches. This scenario simulates a truck moving at a speed of 42.6mph with a data collection frequency of 125Hz, or it can also represent truck speed of 85.2mph with the data collection frequency of 250Hz and so on.

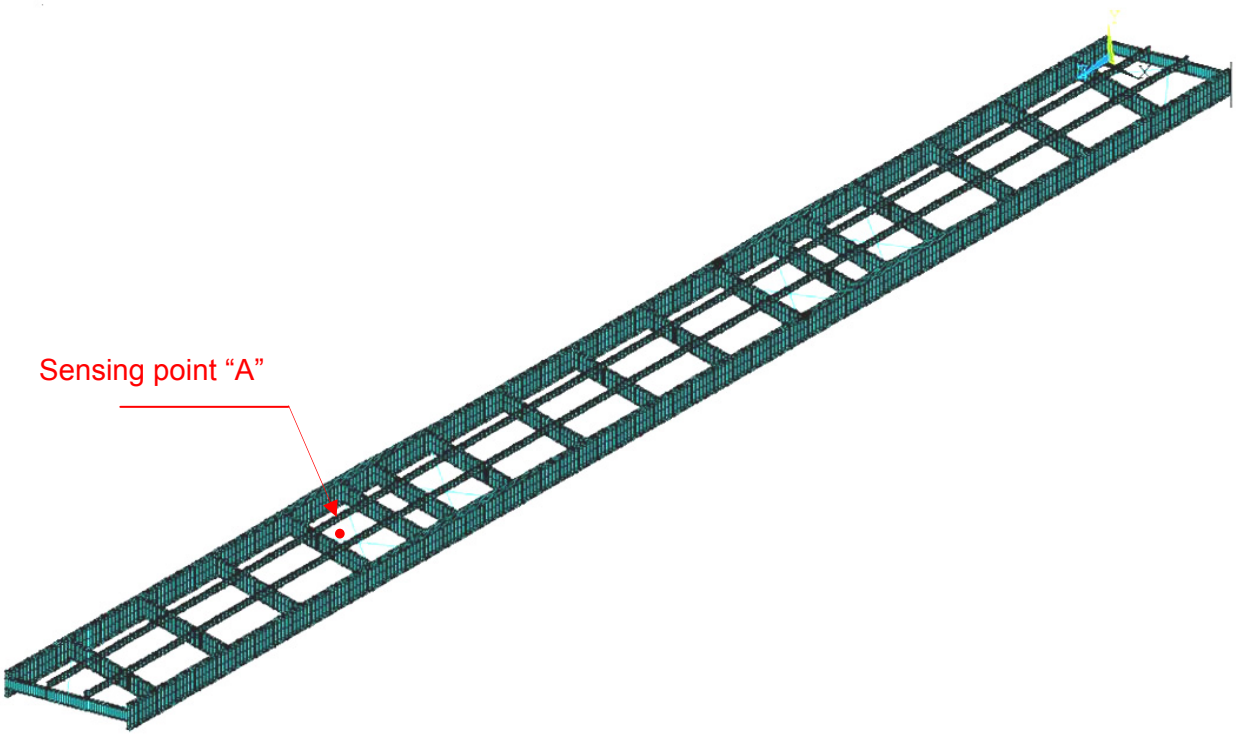

a. The frame system of the bridgemodel

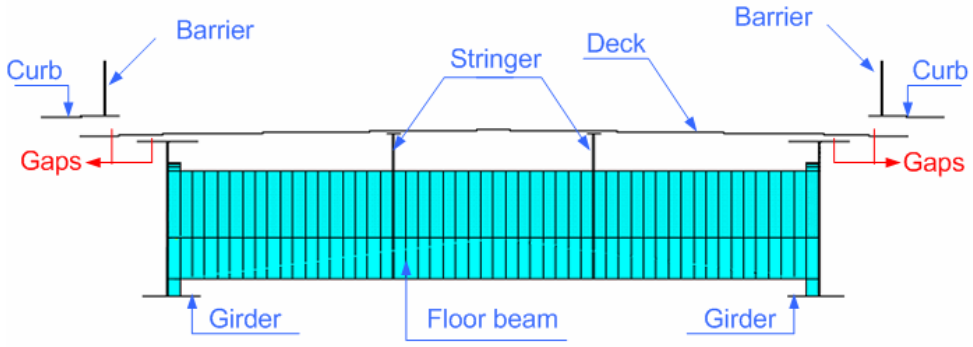

b. The cross section of the bridge model

Figure 4.7 The finite element model of the bridge

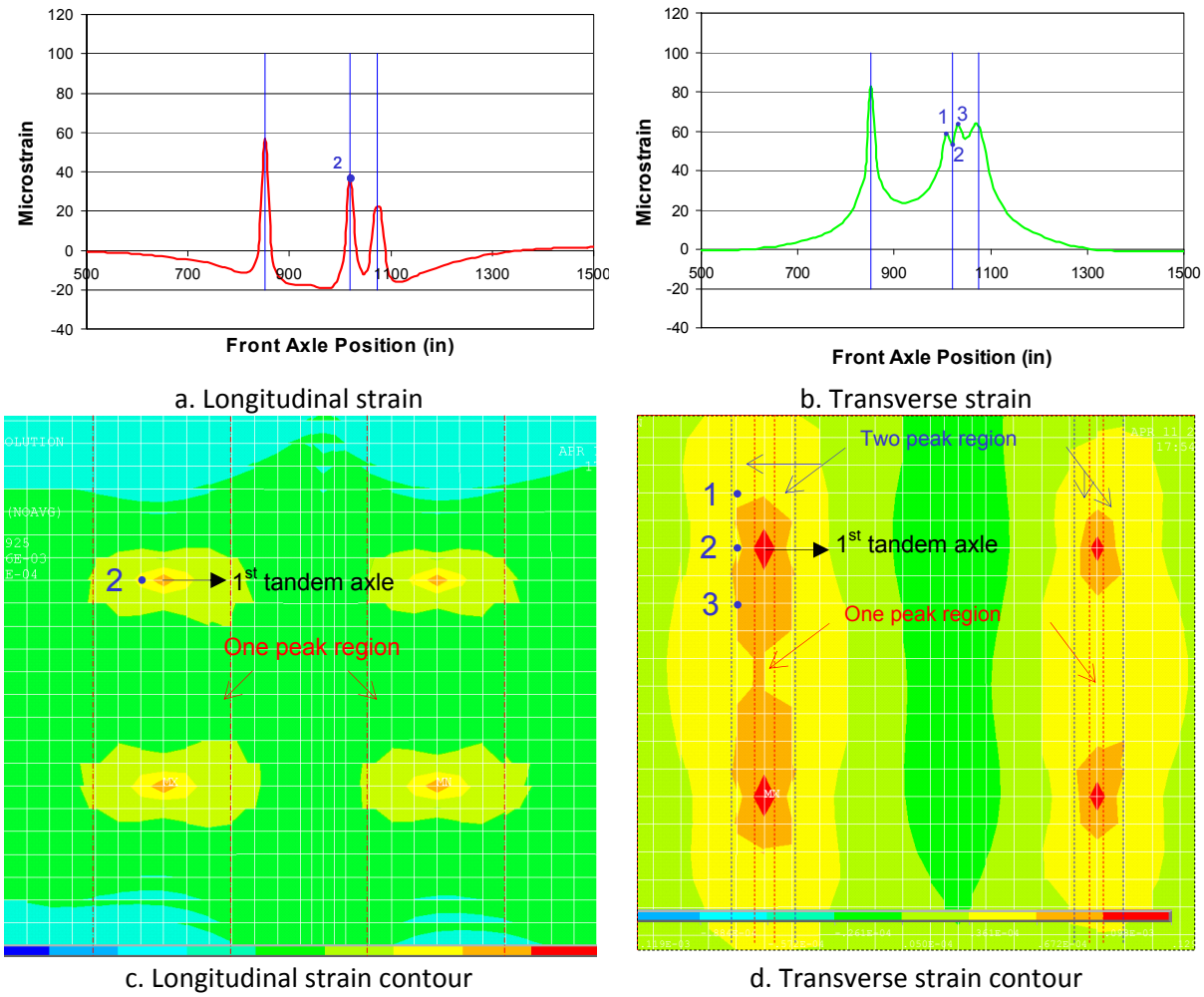

Figure 4.8 The comparison of longitudinal and transverse strain of point "A"

The FEA results were also utilized to study the sensor orientations and associated sensitivities. As an example, Fig. 4.8 presents strains produced by a 3-axle dump truck at sensing point "A" shown in Fig. 4.7a (located at the deck-bottom, one foot west of the deck center line, and above the fifth floor beam). The resulting longitudinal and transverse strains are shown in Fig. 4.8a&b, respectively. The blue vertical lines illustrate the truck positions for which one of the truck axles were aligned with the sensing point. Figure 4.8a reveals a good correlation between the longitudinal strain peaks and the truck axles. However, for the transverse strain the correlation does not always exist. The two peaks marked as 1 and 3 in Fig. 4.8b were produced by a single truck axle. Strain contours shown in Fig. 4.8c&d can explain the different peak patterns of the longitudinal and transverse strains. In Fig. 4.8d, the centers of the four red areas indicate the four tandem wheels of the dump truck. The points marked with 1, 2, 3 show the relative positions between the sensing point and the 1st tandem axle for three continues load steps. Strain at point 2 is smaller than that at point 1 and 3, and as such,

two peaks, peak1 and peak3 in Fig. 4.8b, were formed. As long as the sensing point is located in the two peak regions (Fig. 4.8d), one truck axle will always produce two strain peaks. Only when the sensor is located within the one peak region, can the correlation of the strain peak and truck axles be established. Due to the narrow bandwidth of the one peak region (Fig. 4.8d) and the existence of wide two peak regions, the transverse strain was determined to be inappropriate for truck axle detection. By contrast, the longitudinal strain contour is always convex along the traffic direction, so there is no two peak region. As shown in Fig. 4.8c, the width of the one peak region is as large as 3ft. Including the width of truck wheels into consideration, truck axles are detectable when the sensors are spaced no more than 2ft away from the typical truck wheel line.

Notice that, in the simulation described above, the load step was selected to be 12in. to study the data collection frequency needs. A 12in. step is equivalent to a truck speed of 127.8mph and data collection frequency of 125Hz. The strain peaks shown in Fig. 4.8a indicate, therefore, that 125Hz is adequate for axle detection at highway speeds.

In summary, the FEA study concluded that: 1) deck bottom strain sensors can detect truck axles; 2) sensors must be oriented in the longitudinal direction; 3) sensors must be located within one peak regions, and no more than 2ft from the truck wheel-lines; 4) 125Hz data acquisition frequency is adequate to capture strain peaks produced by highway speed trucks.

4.3.1.2.2 Control Load Test

The FEA results indicated that the longitudinal deck-bottom sensors can detect the truck axles. However, random effects like the unavoidable cracks in concrete structural components and noise caused by the data acquisition system are hard to simulate. So a controlled load test was performed to verify the truck parameter detection ability of the selected sensors in an operational environment.

4.3.2.2.2.1 Testing Instrumentation

Data acquisition system

BDI strain transducers together with the MegaDAC (model 3415AC, Fig. 4.9) general purpose data logger were utilized in the controlled test. The BDI strain transducer, shown in Fig. 4.10, is manufactured by Bridge Diagnostics, Inc. The overall size is 4.375 in x 1.25 in x 0.5 in with an effective gage length of 3.0in.

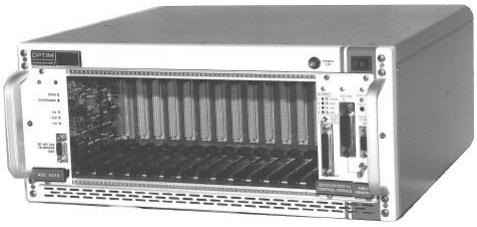

Figure 4.9 MegaDAC model 3415AC

Figure 4.10 BDI strain transducer

BDI sensor installation

Thirty BDI sensors were installed in the west span of the demonstration bridge. As shown in Fig. 4.11, among the 30 BDI sensors, 24 were located on the deck-bottom; and the other six were located on the girder bottom flange with the intention of calculating the truck weight using weight in motion (WIM) concepts. In addition, the two mid-span girder bottom sensors were also used to detect truck event and travelling lane.

4.3.2.2.2.2 Testing Procedure

A three-axle dump truck and a six-axle truck were employed as the control trucks in this testing. The axle configurations of the two trucks are illustrated in Fig. 4.12a & b, respectively. Table 4.1 & 4.2 summarize the axle weight and the total weight of the trucks. During the test, the right lane was first closed for testing and then the left lane. While one lane was closed, the other lane was kept open to normal traffic. Dump1-4 (Table 4.1) were used for right-lane testing and Dump4-7 were used for left-lane testing. For each lane, testing was conducted at both highway speed and crawl speed (twice at each speed). Note that, only right-lane testing was performed with the semi truck.

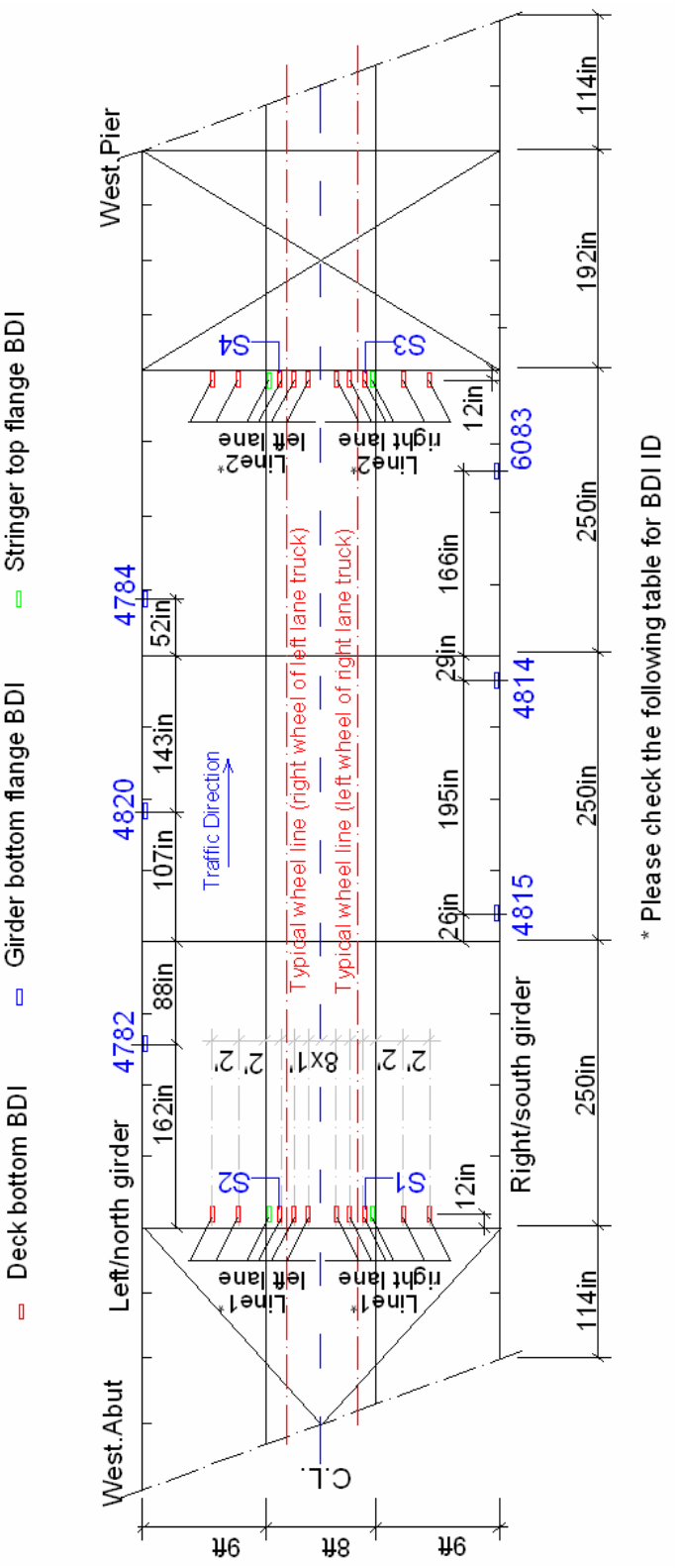

Line1, right lane (right to left)	BDI4696	BDI4805	BDI4703	BDI4785 (S1)	BDI4829	BDI4780
Line1, left lane (left to right)	BDI4816	BDI8708	BDI4781	BDI6084 (S2)	BDI4810	BDI4781
Line2, right lane (right to left)	BDI4825	BDI4812	BDI4821	BDI4692 (S3)	BDI4824	BDI2111
Line2, left lane (left to right)	BDI6079	BDI4807	BDI4787	BDI4811 (S4)	BDI4863	BDI1177
Right/south girder (west to east)	BDI4815	BDI4814	BDI6083			
Left/north girder (west to east)	BDI4782	BDI4820	BDI4784			

Figure 3.3-1 Layout and cross section of US30 bridge

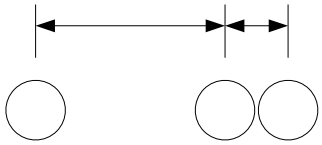

a. Dump truck

b. Semi truck

Figure 4.11 Axle configurations for the testing trucks

Table 4.1 The weights of the dump truck

Truck designation	Weight (k)		
	1st axle	2nd axle group	GVW
Dump 1	11.28	14.24	25.52
Dump 2	13.08	23.94	37.02
Dump 3	12.34	27.54	39.88
Dump 4	13.60	38.78	52.38
Dump 5	11.66	18.16	29.82
Dump 6	11.10	13.98	25.08
Dump 7	12.58	24.40	36.98

Table 4.2 The weights of the semi truck

Truck designation	Weight (k)			
	1st axle	2nd axle group	3rd axle group	Total
Semi 1	44.76	71.96	37.24	153.96
Semi 2	42.06	67.30	34.88	144.24

167

4.3.2.2.2.3 Test Results

Girder bottom sensors

Among the six girder bottom BDIs, BDI4814 and BDI4820 were located at the middle of the first span of the south girder and north girder. They can be used for truck event occurrence and travelling lane detection. Figure 4.13 presents the filtered data for them produced by a right lane truck (Dump2 travelling at 62.25mph). As discussed before, for each mid-span girder sensor, if a threshold is properly defined, one truck event should produce at most one positive peak whose magnitude is

larger than the threshold. Further, the truck's travel lane can be determined by comparing the maximum event-strain values of the two sensors. Figure 4.13 shows a representative truck event and travel lane detection example. The large positive peak in the figure represents a detection of a truck event. It is determined to be a right-lane event since the magnitude of the strain peak of BDI4814 is larger than that of BDI4820, which is consistent with the test conditions. Similar analysis of the data was performed for all control testing. The results demonstrated the effectiveness of the mid-span girder bottom sensors in terms of truck event and travel lane detection.

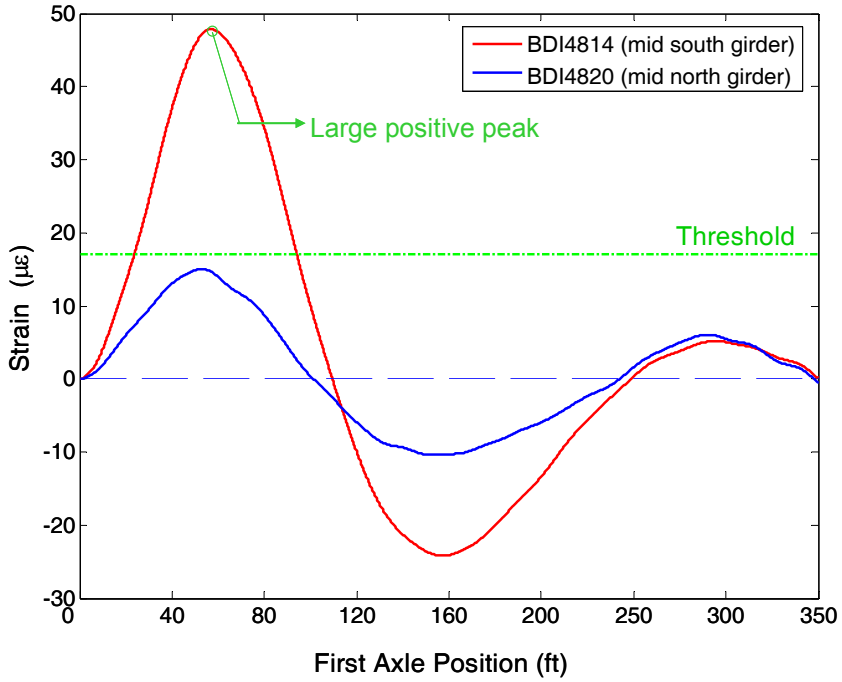

Figure 4.12 The global strains produced by Dump2 at the speed of 62.25mph

deck-bottom sensors

The first deck-bottom sensor line (BDI4703, 4785, 4829, and 4780 in Fig. 4.11) were positioned so that at least one would be sufficiently near to the typical left wheel line of right lane trucks. At the same transverse positions, a second deck-bottom BDI line (BDI4821, 4692, 4824, and 1112), were deployed. The test results showed that the typical left wheel line of right lane truck is located between BDI4785 and 4829. As an example, Fig. 4.14 depicts the strains from the eight deck-bottom sensors. Figures 4.14a&b were generated from the data of Dump2 (Table 4.1), while Figs. 4.14c&d were generated from a random semi truck. In these plots, sensor BDI4785 (referred to as "S1" in the

remainder of the report) and BDI4692 (S3) consistently show the best truck axle detection ability except for Fig. 4.12(d), in which, the strain peaks of BDI112 is sharper than S3. This may have been caused by a slight transverse location shift of the random truck. Nevertheless, S3 is still sufficient for truck axle detection. The strains of left lane trucks were also studied, and the results indicate that BDI6084 (S2) and BDI 4811(S4) are the best deck-bottom sensors for left vehicles.

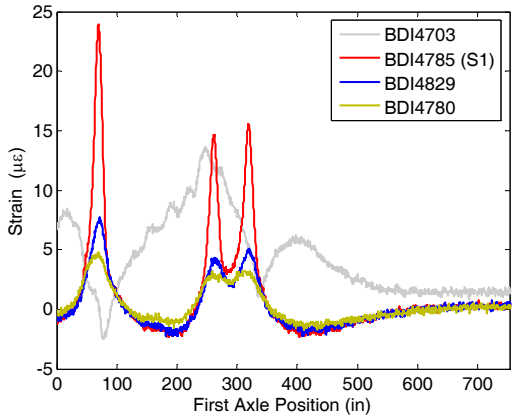

a. Control dump truck (the first sensor line)

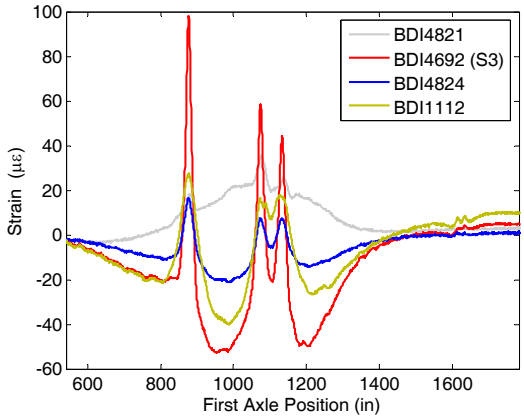

b. Control dump truck (the second sensor line)

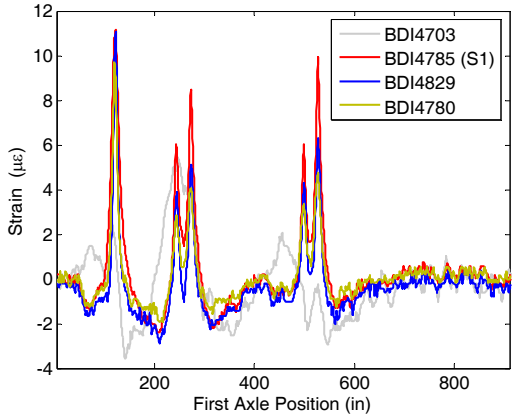

c. Ambient semi truck (the first sensor line)

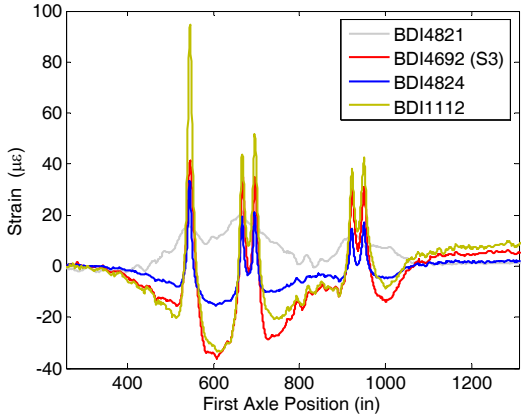

d. Ambient semi truck (the second sensor line)

Figure 4.13 The example of right lane truck strains

The strains of S1 and S3 produced by Dump2 with different travel speeds are compared in Fig. 4.15. The slow1 and slow2 speeds are estimated to be 6mph and 7mph respectively, while fast1 and fast2 are estimated to be 62mph and 58mph. In the figure, the magnitudes of the strain peaks obtained from fast trucks are smaller than that of crawl speed trucks. This indicated that the data collection rate (250Hz) does not ensure the capture of the exact maximum strain peaks for fast trucks. However, as long as the stain peak pattern can show the truck axles, the data collection rate may

still be sufficient. To determine if the data collection frequency can be further reduced without impacting the detection results. The strains shown in Figs. 4.15a&b were processed to simulate data collection rates of 125Hz, 62.5Hz and 31.25Hz. The resulting strains are plotted in Figs. 4.15c & d for

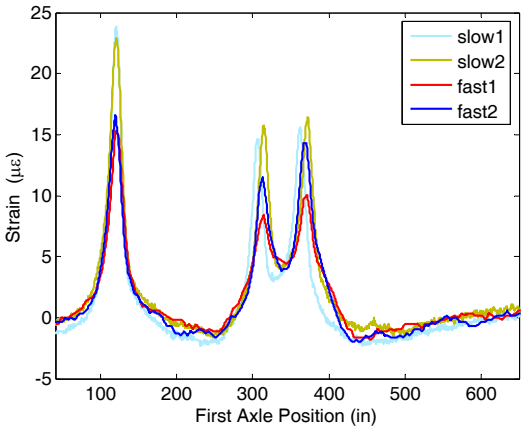

a. Strain of S1 (250Hz)

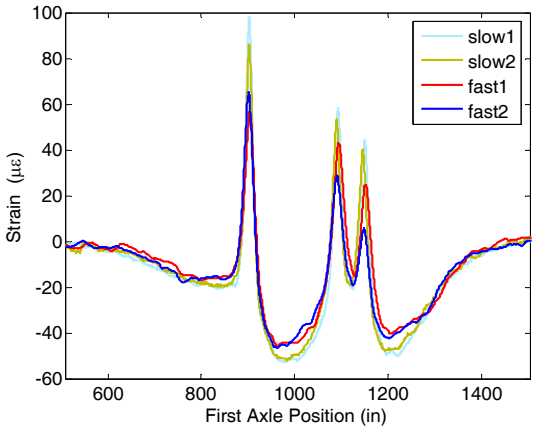

b. Strain of S3 (250Hz)

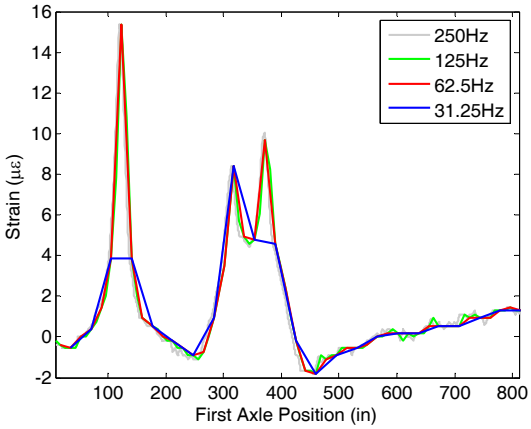

c. S1 truck speed 62.25mph

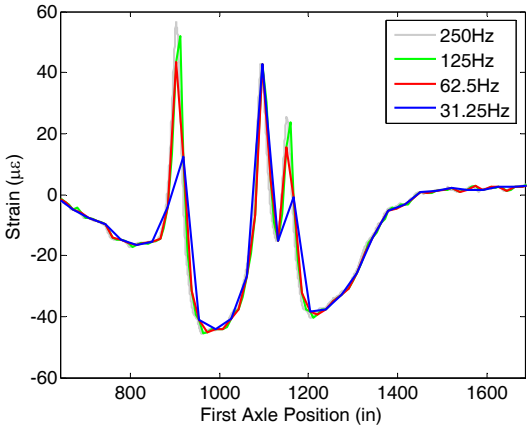

d. S3 truck speed 62.25mph

Figure 4.14 Example of the deck-bottom strain produced by right lane dump truck (dump2)

S1 and S3, respectively. From the graphs one can see that when the frequency was reduced to 31.25Hz, S1 failed to capture all the strain peaks, and as a result, truck axles could be missed. Study with other data sets showed that missed peaks can occur for frequency as high as 50Hz. Note that the current data acquisition system required frequencies be 250Hz/n, where n is an integer. Therefore, 62.5Hz is considered to be the minimum data acquisition frequency for axle detection. In summary, the controlled testing further showed that the mid-span girder bottom sensors can detect truck events and the travel lane and that deck-bottom sensors are capable of detecting truck

axles. The position of deck-bottom sensors should be near to sensors S1, S2, S3 and S4 (Fig. 4.11). The data acquisition rate should not be lower than 62.5Hz.

4.3.1.2.3 New FOS Installation

After verified by FEA and control load tests, eight FOSs (DB1-DB8) were installed at the deck bottom for integration into the long-term structural monitoring system. The FOS locations were selected to be near the identified typical wheel lines (as shown in Figs. 3.5 and 3.7), and the sensors were positioned in the traffic direction.

Figure 4.16 presents a truck axle detection example using the deck-bottom FOSs. The strains shown in the figure were produced by the same semi and dump trucks that produced Fig. 4.6. Figure 4.16 shows a very good correlation between the truck axles and the strain peaks. However, further studies indicated that there are cases that the truck axles are not as easy to detect as those shown in Fig. 4.16. In instances when this happen, a double checking algorithm (will be discussed shortly) is proposed to improve the axle detection results.

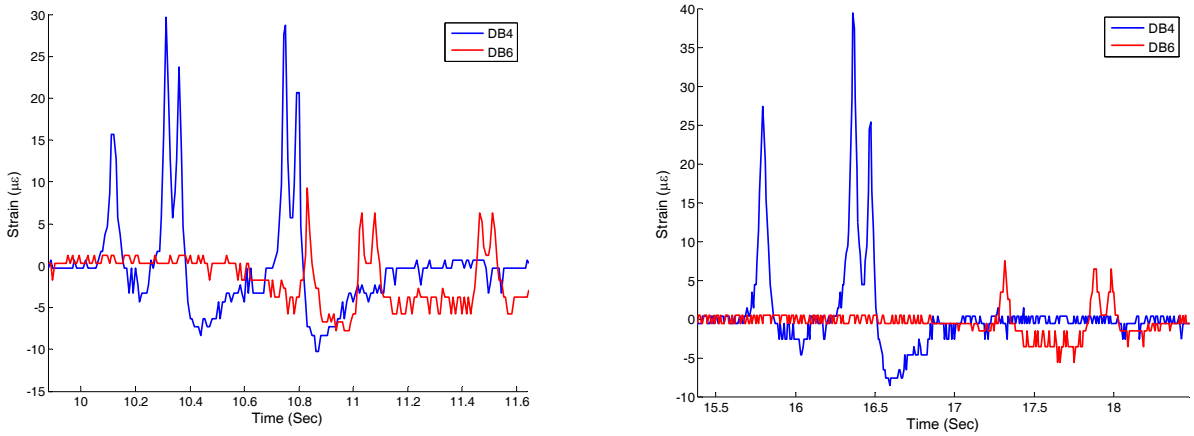

a. Strains produced by five-axle semi truck b. Strains produced by dump truck

Figure 4.15 Strain of deck-bottom FOSs

4.3.2 Truck Parameter Detection and Calculation

The global sensors, B-SG-BF-H and B-NG-BF-H, and local sensors, DB1-DB8, are all involved in the truck parameter detection/calculation procedure. Before implementing the final truck detection component for the long term SHM system, conceptual functions were developed using the control

load tests data and/or FEA results to verify the proposed methodology. The results indicated that parameters of travelling lane, truck axles, speed, axle distances, and event start and end times can be detected/calculated very well. However, for truck weight calculation, the error was considered to be unacceptable. Therefore, in the SHM system implementation, instead of trying to calculate the exact truck weight, trucks were roughly classified into two weight categories: heavy or light.

The truck detection program was implemented in a two stage hierarchical way. First, selected global sensor data were scanned to screen for truck events and to estimate the event time window; then, the data from the deck-bottom sensors within the roughly estimated time window were further analyzed to confirm the event and calculate the parameters including number of axles, speed, axle spacings, and event start and end time. For each truck event, the start and end time are compared with that of other truck event to determine if it is a concurrent event (i.e. multiple trucks on the bridge at once).

The following sections present the methodology and implementation of the truck parameter detection function. Details of the truck weight calculation procedure, including the WIM concept, FEA feasibility verification, and controlled test verification are documented in Appendix A.

4.3.2.1 Event Occurrence and Travel Lane Detection

The procedure for truck event and travel lane detection is illustrated in Fig. 4.17. When a collected data set accumulates to the size of one mega-bite, a new data file is created and it automatically triggers the event detection procedure. The data for sensor B-SG-BF-H and B-NG-BF-H are zeroed and filtered before being fed to peak detection function. The “south/north peaks” in Fig. 4.17 refer to the positive peaks for the south/north girder bottom sensor data and their magnitude must be larger than a predefined threshold value; the threshold was determined to be 17 $\mu\varepsilon$ for the demonstration bridge. As discussed before, the peaks are indications of truck events. If the truck was detected by only one sensor (Case3 or Case4 in Fig. 4.17), the travel lane is directly determined.

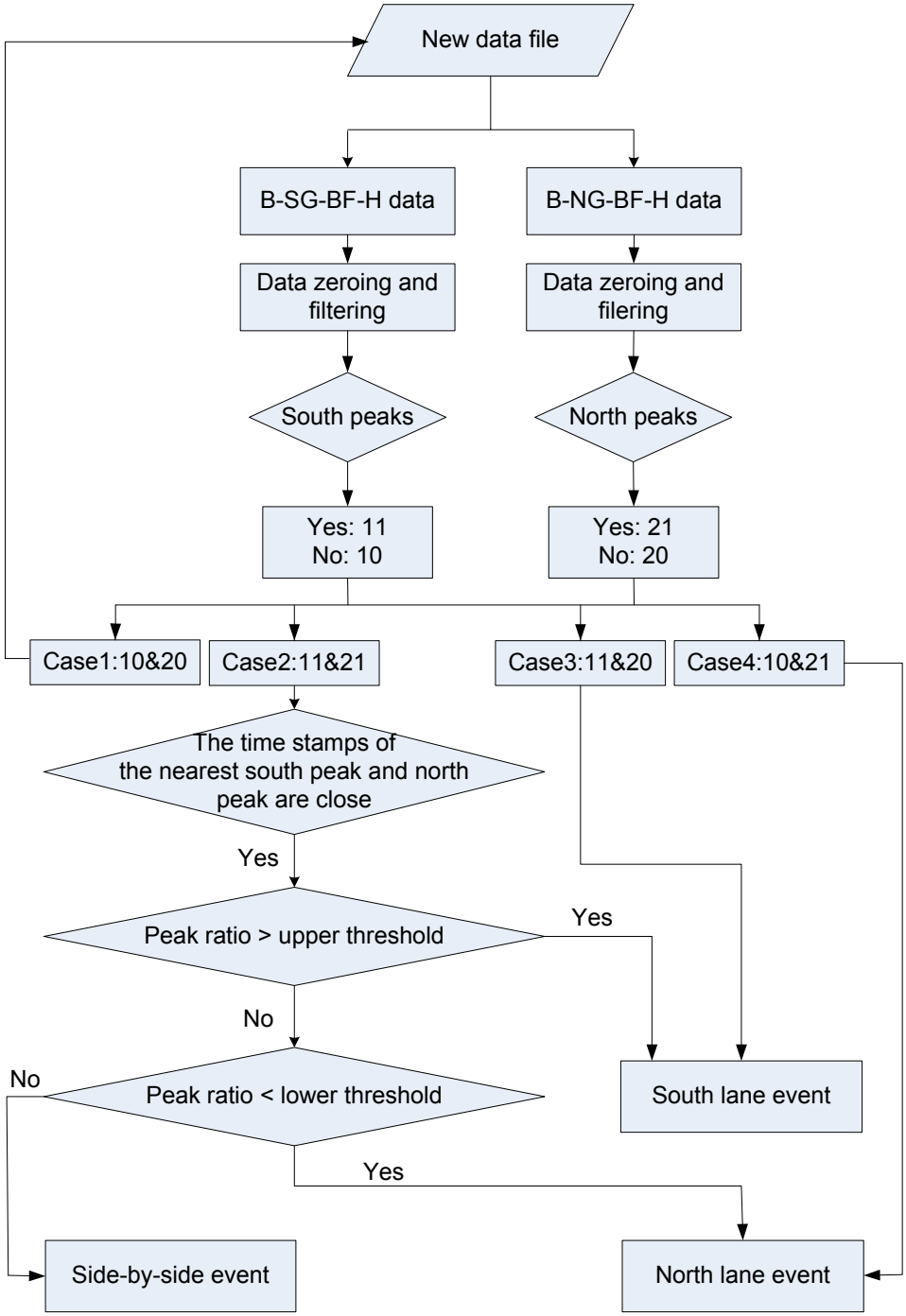

Figure 4.16 Truck event and travel lane detection procedure

For example, the peak1 in Fig. 4.18 represents a right lane event. If an event is detected by both sensors (Case2 in Fig. 4.17), such as the peak2 & 3 shown in Fig. 4.18, it could be a side by side event,

or it could simply be a heavy truck. These two cases (e.g. side by side event or heavy truck event) can be differentiated by comparing the relative magnitudes of the two peaks (peak2 & 3 in Fig. 4.18). If they are close to each other, to be more specific, the ratio of the south peak over the north peak is within the range of 0.52 to 1.6, the peaks are considered to be produced by side by side event at the screening level. Otherwise, if the magnitudes of the two peaks are significantly different so that the peak ratio is outside of the range shown in Fig. 4.19, the event should be either a south-lane event or a north-lane event dependent upon which peak is larger. Following the described side-by-side event and single-lane event differentiation rule, the event represented by peak2&3 in Fig. 4.18 would be determined to be a south-lane event.

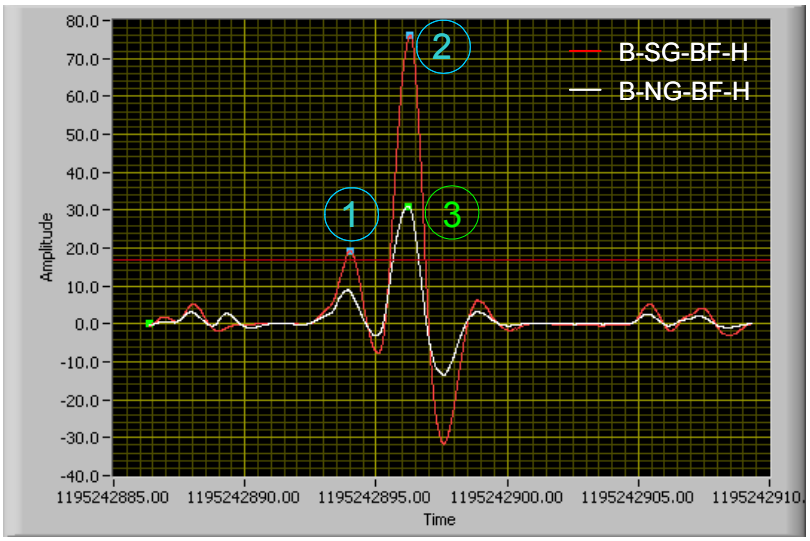

event lane, time sequency, time stamp, maximum 2

1	1
953	1240
1195242894.004	1195242896.3
19.28296279907	76.15962219238

Figure 4.17 Truck event screening and travelling lane detection

The peak-ratio-thresholds used above (i.e., 0.52 and 1.6) were determined from the peak ratio histogram data shown in Fig. 4.19 and a simple analytical study of two extreme cases: 1) Assuming a very heavy truck on the right lane and a very light truck on the left lane; 2) The reverse of case 1. Heavy truck on the left lane and light truck on right lane. Fig. 4.19 is generated from one week training data sets. The two obvious peaks (shown by green lines) in the histogram show the peak ratio of typical right lane and left lane single truck events and they are approximately 2.1 and 0.4, respectively. For the first case, the heavy truck was assumed to produce a 120 $\mu\varepsilon$ peak strain at B-SG-BF-H and thus a 57 $\mu\varepsilon$ ($120\mu\varepsilon / 2.1 = 57\mu\varepsilon$) peak strain might be produced at B-NG-BF-H; at the same time, the light truck on the left lane was assumed to produce a peak strain of 20 $\mu\varepsilon$ for B-NG-

BF-H and 8 $\mu\varepsilon$ for B-SG-BF-H. Summing the peak strains results in a total peak of 128 $\mu\varepsilon$ for B-SG-H and 77 $\mu\varepsilon$ for B-SG-H. Thus the peak ratio for this situation is equal to 128/77 = 1.6, which is the upper threshold for side-by-side events. Repeating the same analysis for case 2, assuming the heavy truck produce a 120 $\mu\varepsilon$ peak strain for the north girder sensor (B-NG-BF-H) and the light truck produce a 20 $\mu\varepsilon$ peak strain for south girder sensor (B-SG-BF-H). The peak ratio is calculated to be 0.52, and it is used as the lower threshold for a side-by-side event.

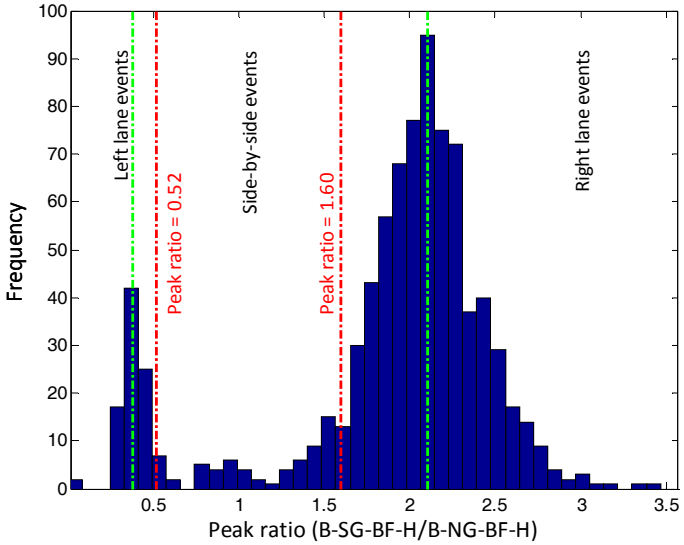

Figure 4.18 Histogram of the peak ratio obtained from one day data

After the truck event was initially detected, the data from the deck-bottom sensors within a roughly estimated time window are used to determine the number of truck axle, speed, axle spacings, and the event start and end time (i.e. when the tuck entered and exits the bridge, respectively). In the case that a side-by-side event was detected, the data for all deck-bottom sensor data are further processed. For single lane events, analyses need to be performed for select sensor data only. With the screening step mentioned above, only a small part of the deck-bottom sensor data are selected to be further processed and as such saves significant computation time and resources.

4.3.2.2 Number of Truck Axles, Speed and Axle Spacings Calculation

After the event screening, select deck-bottom sensor data are passed to a second function to determine the number of truck axles, which is a key step for other parameter calculations. Once the truck axles and the associated time of occurrence are determined, the duration that it takes an axle

to reach the first and second line of deck-bottom sensors can be calculated. As the distance between the two sensor lines was known, the truck speed is that distance divided by the time duration. With the truck speed known, calculation of the axle spacings, and the event starts and end time is straightforward.

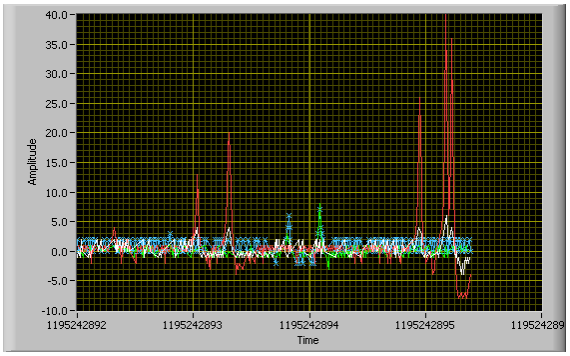

a. Peak1 event

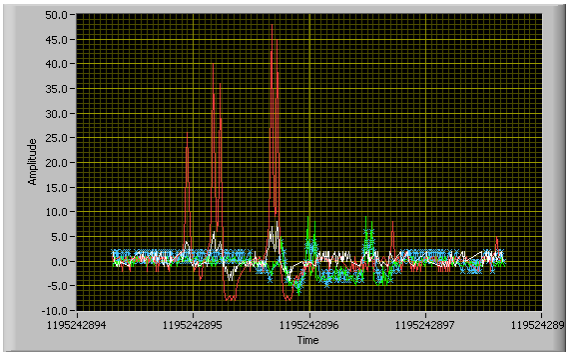

b. Peak2 & 3 event

1	1
19.28296279907	76.15962219238
1195242893.028	1195242894.94
1195242897.228	1195242899.772
2	5
21.4646429275	60.04901347207
53.80509641873	52.22259358289
831	1070
1356	1674
21.4646429275	17.76959820121
0	3.676478038816
0	33.70098477485
0	4.901952457194

c. The calculated parameters

Figure 4.19 The strain plot of the deck bottom sensor data

4.3.2.2.1 Detection of Truck Axles

When the truck is relatively heavy and near a sensor, the peak strains measured by the deck-bottom sensors represent the passage of a truck axle very well. As an example, Figs. 4.20a & b depict deck-bottom sensor strain patterns associated with the events denoted by Peak1 and Peak2&3 in Fig. 4.18. The table in Fig. 4.20c lists the calculated parameters which include: travel lane, maximum first mid-span girder bottom strain, event start time, event end time, number of axles, total truck length, speed, start point ID, end point ID, and axle spacings. The results indicated that the first truck (Fig. 4.20a) has two axles while the second one (Fig. 4.20b) has five axles. The detected number of truck axles is consistent with the number of strain peaks. Here a strain peak was considered to be

detected only when its magnitude is larger than the predefined threshold value (3 $\mu\varepsilon$). Peaks detected in this way were referred as strong peaks and such detection are called strong detection. In this example, truck axles were determined by strong peak detection results.

However, the axle detection may not be always as simple as strain peak detection. There are cases that the strain peaks are not as ideal as those shown in Fig. 4.20. Figure 4.21 presents a less than ideal example in which the first line of deck-bottom sensors failed to detect one axle of the second tandem group of the five-axle semi truck. Observations indicated that missing peaks is not a rare occurrence. To solve this problem, a three step data processing strategy was developed:

1) Lower the peak detection requirement. In the example described above, only strong detections were allowed. Doing this can avoid the detection of false-peaks (Fig. 4.21) caused by the sensitivity ($\pm 2\mu\varepsilon$) limitation of the FOSs. However, in less than ideal situations, the use of strong peaks alone can miss some peaks that were produced by truck axles. Therefore, peaks with the magnitude larger than the upper bound of zero readings and smaller than the strong peak threshold value (3 $\mu\varepsilon$) are allowed. These peaks are called weak peaks and such detection is referred as weak detection. Upper bound of zero readings (one example is shown in Fig. 4.21) is the maximum strain reading of a sensor when the true strain value is zero. It can be determined by finding the modes of positive strains of the sensor in a collected data file.

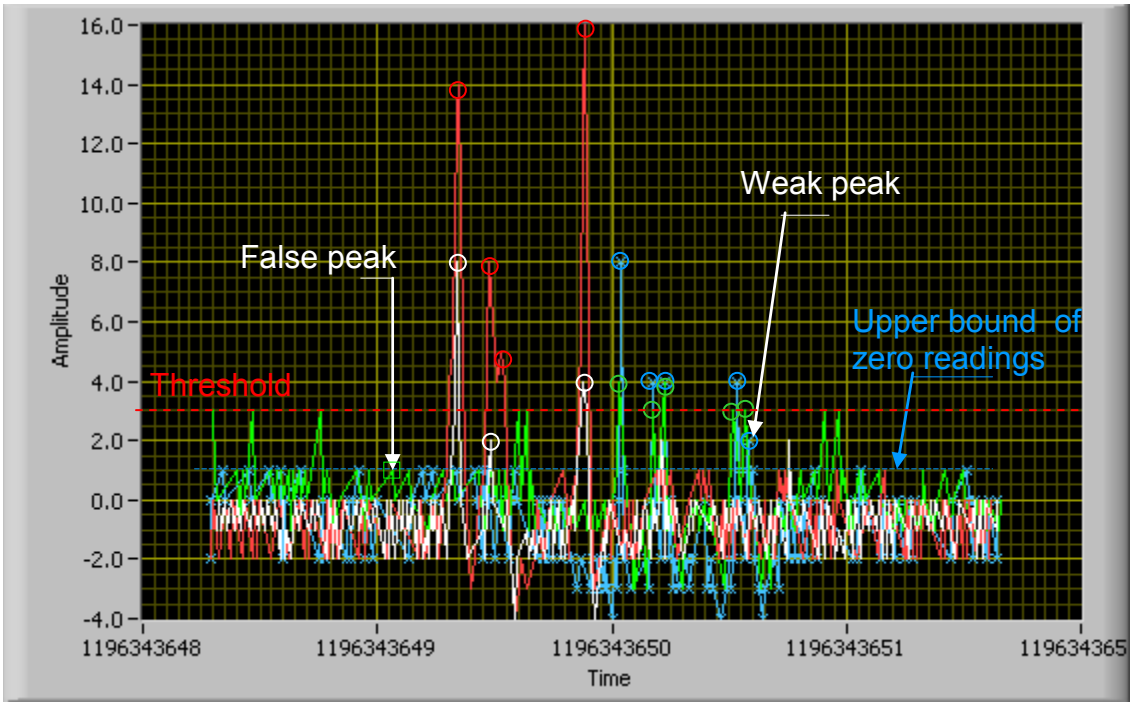

Figure 4.20 An imperfect truck axle detection example

Table 4.3 The number of strong detections and weak detection received by each truck axle (for the example shown in Fig. 4.21)

Axles	Number of strong detections	Number of weak detections
1st axle	4	0
2nd axle	2	2
3rd axle	3	0
4th axle	1	1
5th axle	2	2

2) Create a polling strategy to cross check the peak detection results among the sensors. After the strong peaks and weak peaks were detected for all involved deck-bottom sensors, they are combined to form two peak-groups, one for each sensor line. The time stamps associated with each peak are then used to calculate the t (see Fig. 4.22), which is the time duration that a truck moved from the first sensor line to the second. As shown in Fig. 4.22, T_0 is the time stamp when the first axle of the truck aligned with the first sensor line, and T_1 is the time stamp when the axle moved to the second sensor line. The difference between T_1 and T_0 is the time duration of t. In the similar way, t can be calculated using any axle of a truck. If assumes that the truck does not appreciably change speed on the bridge, t will be

same for all truck axles. Its value can be determined by finding the most common time-stamp difference between any two peaks, and one from each peak-group. The detailed steps of the calculation are described in Appedix B. After t was calculated, the two peak groups can be further combined into one. To do this, the time-stamp of each peak in the second group was shifted with t . The peak detection results obtained from both the first and the second sensor lines were then cross checked through a polling procedure. A peak can be confirmed when it receives at least two detections, and at least one of them is a strong detection. Only peaks passing the checking procedure are considered to be truck axle indications. For an example, if a south-lane event is detected, four deck-bottom sensors will be involved in the axle detection procedure. In an ideal situation, one sensor creates a strong detection for one axle, and thus, each axle can receive four strong detections during the polling. For another example, for the data shown in Fig. 4.21, the number of strong detections and weak detections received by each truck axle were presented in Table 4.3. The polling results indicated that all five truck axles passed the cross checking. The axle that failed to be detected by the first sensor line was, as such, confirmed without introducing any false detection.

3) In addition to the cross checking procedure, other knowledge based constraints, such as, the reasonable ranges of axle spacings, truck speeds and so on, were also applied to ensure correct truck axle detections.

4.3.2.2.2 Calculation of Speed, Axle Spacings, and Other parameters

During the truck axle detection discussed above, the time duration that the truck traveled from the first sensor line to the second (t in Fig. 4.22) was calculated. The distance between the two deck-bottom sensor lines was known after the sensors were installed, and it is denoted as d1 in Fig. 4.22. The truck speed can be simply calculated as the distance over the time duration (Eq.4.1).

$$Speed = \frac{d1}{t} \qquad \text{Eq.4. 1}$$

in which, d1 is the distance between the two sensor lines, and

t is the time difference of one axle on two sensor lines.

After the truck axles are identified, the time that a truck axle is located over a deck-bottom sensor line is known; therefore the difference between the time stamps for any two adjacent axles can be

calculated. As shown in Fig. 4.22, $t1$ is the time difference between the first and the second truck axles. The axle spacings are the speed multiplied by the time differences, and the total truck length is the sum of all axle distances (see Eq.4.2 and Eq.4.3).

$$Axle\ spacing_i = Speed \times t_i \qquad \text{Eq.4. 2}$$

$$Total\ truck\ length = \sum_{i=1}^{number\ of\ axles\ -1} Axle\ spacing_i \qquad \text{Eq.4. 3}$$

in which, t_i is the time difference between i-*th* and (i+1)-*th* axle, and

Speed is the truck speed calculated before.

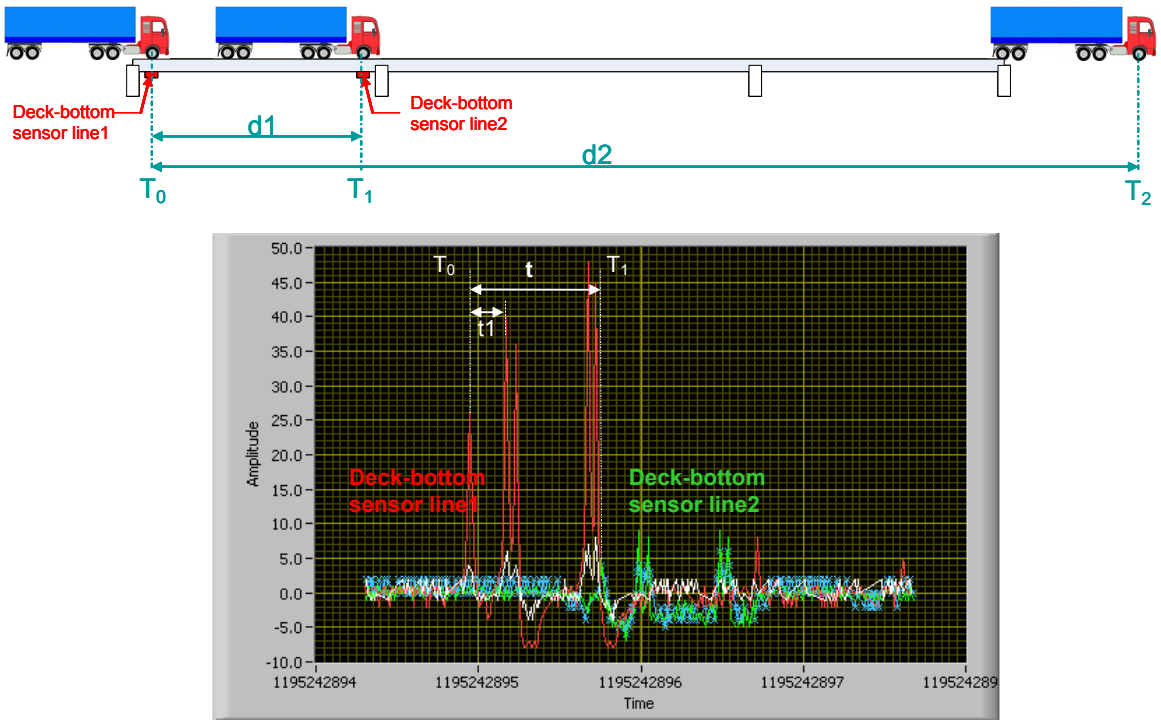

Figure 4. 21 Speed, axle spacings and other parameter calculation

The time when the first axle of a truck reaches the bridge is defined as the event start time. The first deck-bottom sensor line is taken as the start point of the bridge as it is very near to the west abutment, and thus, T_0 in Fig. 4.22 is the event start time. The event end time (T_2) is the time instance that the last axle of the truck is leaving the bridge. It can be estimated as following:

$$T_2 = T_0 + \frac{Bridge\ length + Total\ truck\ length}{Speed} \qquad \text{Eq.4. 4}$$

After obtaining the event start time and estimated event end time, the side-by-side events detected at the screening stage can be confirmed at the detection level. In addition, other concurrent truck events can also be detected by comparing the event start and end times associated with adjacent trucks. Figure 4.23 presents the four different concurrent event cases. Case (a) is the side-by-side event that can be detected at the screening stage. In this case, the two trucks are undifferentiable by the global sensors. Case (b) shows another side-by-side scenario, unlike case (a), the trucks produce different global peaks. So they are identified as two different events at the screening stage. Cases (c)& (d) illustrate two one-after-another truck events, which involved at least two trucks in the same lane simultaneously. Concurrent events data are included in the truck detection output report and they are not be used in the damage detection procedure.

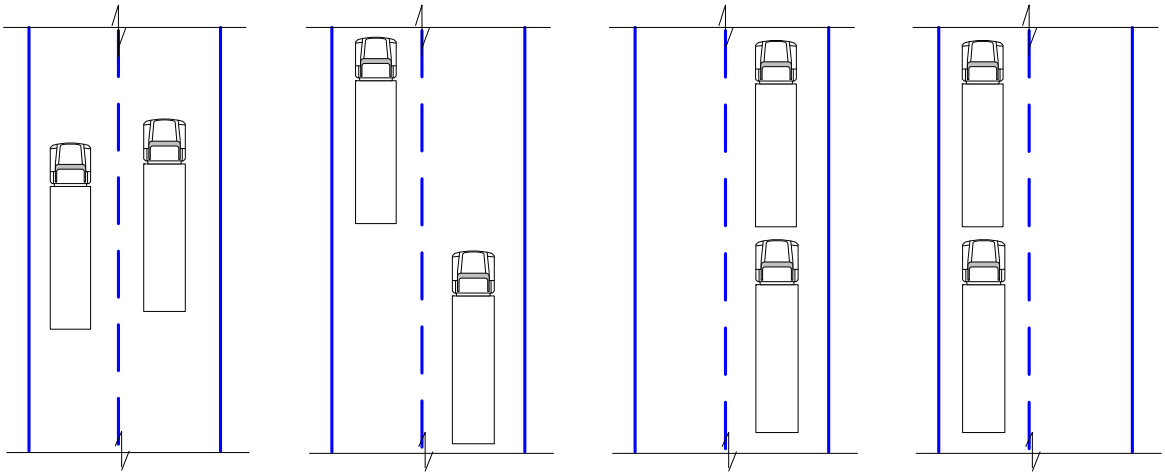

a. side-by-side b. side-by-side c. one-after-another d. one-after-another

Figure 4. 22 Concurrent events

4.3.2.2.3 Evaluation of the Truck Parameter Calculation Method

To evaluate the truck parameter calculation method, truck speed and axle distances calculated from the BDI test data were studied and selected examples are summarized in Tables 4.4 and 4.5. The examples were selected to cover as many different cases as possible, in particular, they included dump and semi trucks, left-lane and right-lane events, highway and crawl speeds. During the test, the base-line truck speed data were not collected, so direct evaluation of the speed results was not possible. However, the accuracy of speed calculation can be indirectly evaluated by the small errors in the calculated truck axle spacings. In fact, the small errors in truck axle spacings proved the performance of the entire truck parameter calculation procedure, because its calculation involved most other truck parameters such as speed, t , $t1$, etc.

Table 4.4 Speed and axle distances for right lane 6-axle semi truck (Semi2)

Speed (mph)	Axle distances (inch)					Error
		BDI4785&4692	BDI4829&4824	Average	Actual	
5.6	D1	167.0	161.9	164.4	167.0	-1.54%
	D2	52.8	51.6	52.2	56.0	-6.82%
	D3	338.7	333.2	335.9	336.0	-0.02%
	D4	49.2	49.2	49.2	49.0	0.47%
	D5	49.6	49.2	49.4	50.0	-1.15%
	Total	657.3	645.1	651.2	658.0	-1.03%
54.2	D1	164.0	164.0	164.0	167.0	-1.78%
	D2	53.4	53.4	53.4	56.0	-4.64%
	D3	339. 5	339. 5	339. 5	336.0	1.04%
	D4	49.6	49. 6	49. 6	49.0	1.20%
	D5	53.4	49. 6	51.5	50.0	2.99%
	Total	659.9	656.1	658.0	658.0	-0.001%

Table 4.5 Speed and axle distances for left lane dump truck (Dump5)

Speed (mph)	Axle distances (inch)					
		BDI6084&4810	BDI4811&4863	Average	Actual	Error
6.4	D1	180.9	178.3	179.6	176.0	2.04%
	D2	55.1	53.2	54.2	56.0	-3.24%
	Total	236.0	231.5	233.8	232.0	0.76%
55.0	D1	178.1	178.1	178.1	176.0	1.18%
	D2	55.4	55.4	55.4	56.0	-1.07%
	Total	233.5	233.5	233.5	232.0	0.64%

4.4 Data Selection

The calculated truck parameters along with the extreme event strain values, including both the maximum and minimum strains, for the 40 performance monitoring sensors were permanently saved for each truck event and they can be retrieved by other algorithms. The truck parameter results allowed the selection of the standard load condition that will be used in the structural condition evaluation. Obviously, the data selection procedure also served as the information extraction function for the SHM system, which reduced the size of collected data dramatically. A study of a randomly selected day shows that the data volume was reduced by more than 98.

After all identified parameters were determined, the data shown in Fig. 4.1 were re-plotted and shown in Fig. 4.24a (the concurrent event data were removed). In the figure, circles and triangles represent right lane and left lane events, respectively. The events are color coded according to the

truck type as determined by the number of axles. For example, a green circle represents a right lane, five-axle truck event. Figure 4.24a shows that the extreme strain relationships are highly correlated with truck types and travel lanes. As an example, Fig. 4.24b depicts the relationship created by five-axle truck data. The two significantly different data patterns indicate that for the same type of trucks, the travel lane can lead to different strain relationships. Further, as shown in Fig. 4.24c, trucks in the same travel lane but different geometry configurations can also produce different strain relationships. Figure 4.24d displays the extreme strain relationship produced by right-lane, five-axle trucks. Apparently, the linear pattern is more easily defined for this subset than for those shown in Fig. 4.24a to c. Even for the same lane and same truck type, the data in Fig. 4.24d can still be further roughly divided into two groups according to the strain-ranges of sensor B-SG-BF-H. This is more clearly shown in the maximum strain histogram plot (Fig. 4.25). Data with values smaller than 55 $\mu\varepsilon$ represented lightly loaded or empty trucks, while the others represented heavily loaded trucks. The slightly different extreme strain relationship patterns produced by the two truck groups (Fig. 4.24d) indicate that classifying the trucks into weight groups is necessary. The strain magnitude variance within each group can be explained by the linear model and will be further eliminated by a strategically selected damage indicator.

In this work, data from non-concurrent, right-lane, five-axle, heavy trucks were further analyzed to determine the structural status. This loading condition was selected for three reasons. First, it has the largest truck population. As shown in Fig. 4.24a, the number of five-axle trucks is much larger than that of any other truck. In any given time duration, using this type of truck can result in more data sets and thus reduce the damage detection time delay. Secondly, heavy five-axle semi trucks can produce larger absolute strains, which can be sensed with a lower percent error. In addition, heavy trucks likely lead to a more significant strain shift when damage does occur. In Chapter 5, the damage detection results obtained from different weight groups of right-lane, five-axle semis are compared to further verify the advantage of the utilization of the heavy truck group.

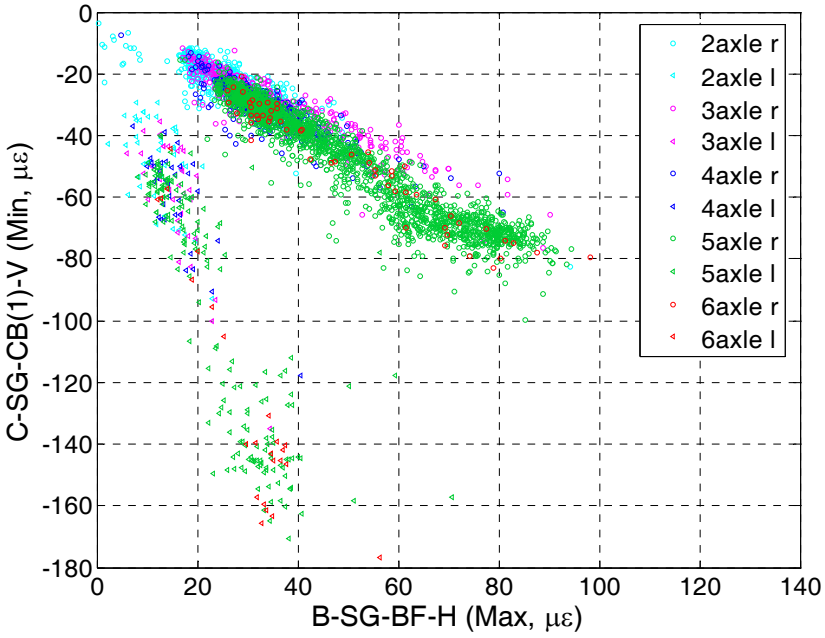

a. The relationships produced by all trucks and lanes combinations

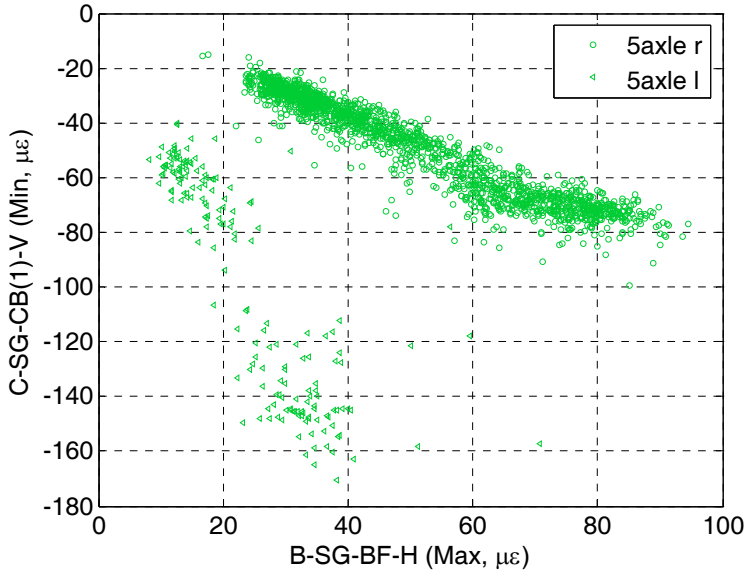

b. The relationships produced by right-lane 5-axle trucks and left-lane 5-axle trucks

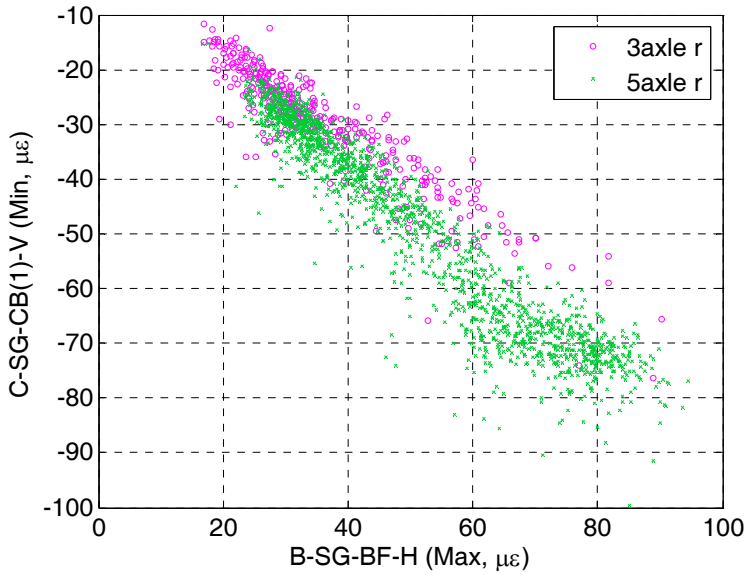

c. The relationships produced by right-lane 3-axle trucks and 5-axle trucks

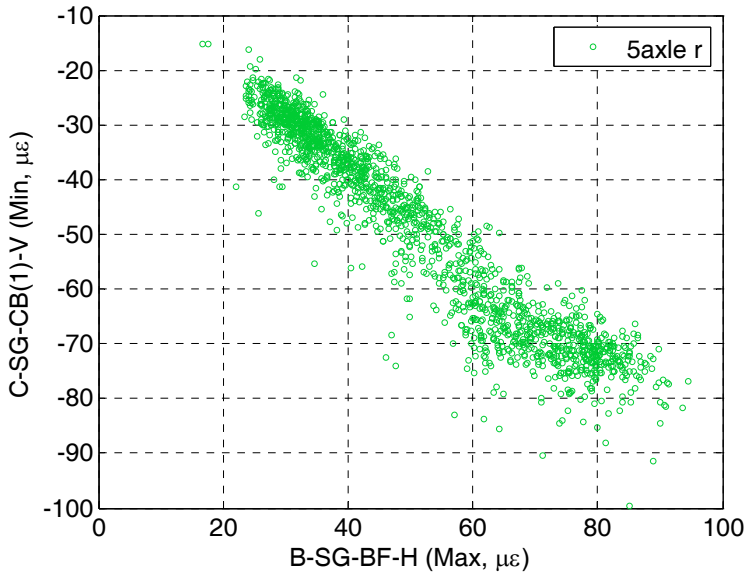

d. The relationship produced by right-lane 5-axle trucks only

Figure 4.23 An example of the typical relationship of extreme even strains of two sensors

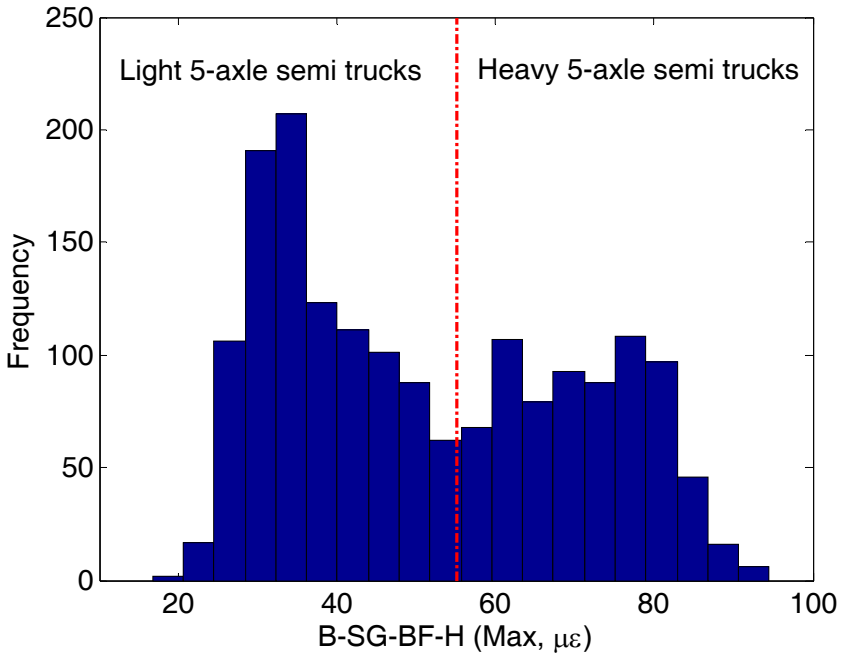

Figure 4.24 Histogram of the maximum event strain of B-SG-BF-H

CHAPTER 5 DAMAGE DETECTION ALGORITHM DEVELOPMENT AND EVALUATION

Damage can be defined as changes introduced into a system that adversely affects its current or future performance (Sohn 2003). For damage detection approaches which utilize time domain response data only, the comparison between two different states of the structural system is essential. One of the states should be the baseline which represents the performance of undamaged structure. Statistical pattern recognition has been shown to be an effective comparison tool by dynamic-based SHM systems. However, its application with time domain static (pseudo-static) strain data is very limited, if existing, at all.

5.1 Damage Detection Algorithm

In this work, new damage detection approaches, which primarily focus on the detection of relatively small local damages in highway bridges, were developed and studied. The approaches utilize event based extreme live load strains as the input data and statistical control chart philosophies were employed as the comparison tool. Intuitively, comparing the strain data recorded by each sensor can indicate the occurrence of damage and the sensor location can be used to indicate the damage areas. Further study, which is described herein, showed that residuals, which are defined as the difference between the collected strain data and the predicted data calculated from linear prediction models, are more sensitive to local damage than strain itself. This is likely due to fact that the strain variances caused by varying truck weights are removed during the residual calculation procedure. Two major prediction models were studied here:

1) One-to-one model: with this model, strains from combinations of two sensors in the sensor network are used to predict each other. For example, there are 40 performance monitoring sensors in the testbed SHM system. For each event, the strain data of any sensor “A” were used to predict the data of any other sensor “B”. For this system, 1600 prediction models can be created.
2) Many-to-one model: with this model, the strain for one sensor is predicted by involving all other sensors. For the demonstration system, the data for 39 sensors are used to predict the data for the remaining one sensor. Altogether, 40 such models can be created for the demonstration installation.

The size of the residual matrix/vector is determined by the prediction model type (e.g., one-to-one or many-to-one model). When the dimension equals the number of sensors (e.g. for the many-to-one model), one control chart can be created each one sensor and, thus, the control chart analysis results show the occurrence of damage and the damage location directly. In the case of the one-to-one model, two damage identification solutions are proposed:

1) Direct evaluation method. This method first simplifies the residual matrix into desirable dimensions by calculating the row-sum, column-sum or the combine-sum (equal to the row-sum minus column-sum). The obtained sum-residual matrix is then used as the damage metric with which control charts can be created to evaluate the structural condition. The control chart results show the structural state directly. As such, this method is referred to as direct evaluation method.
2) Two-level evaluation method. With this method, a first level control chart is created for all elements in the residual matrix. The first level evaluation results are then used to generate an evaluation matrix. The dimension of the evaluation matrix is the same as that of the residual matrix. Therefore, the simplification (row-sum, column-sum, combine-sum) is necessary. With the simplified evaluation matrix calculated, a second level control chart can be generated for each sensor and the control chart result indicates the structural status. Since two levels of control charts were involved here, this method is referred to as two-level evaluation method.

Although the implementation of the damage detection approach is slightly different when different prediction models and different damage indictors are used, the major steps are roughly the same, and they all include the training procedure and the monitoring procedure. The general steps involved are:

<u>Training procedure:</u>

1) Create linear prediction models from training data.
2) Calculate the residual matrix for each event.
3) Convert the residual matrix into the damage indicator.
4) Create the training stage control chart on the damage indicator

<u>Monitoring procedure:</u>

1) Calculate the residual matrix for each event using the linear prediction model created in the training stage.
2) Convert the residual matrix into the damage indicator.
3) Chart the damage indicator to determine the structural health state.

The proposed damage detection approaches use an unsupervised learning method. Only data from the undamaged structure are involved in the training. However, to verify the method, data of damaged structure is necessary. As the damage data are not available through field monitoring, finite element analysis was carried out to generate the needed synthetic data sets that represent the damaged condition.

In the remainder of this chapter, the FEA procedure, results and synthetic data generation are first presented in Section 5.2. Section 5.3 discusses the one-to-one model direct evaluation method. Different one-to-one models (e.g. max-max, max-min, min-max, min-min and range models) and different residual simplification procedures were compared. The best one-to-one model and residual simplification method is then recommended. Section 5.4 presents the two-level evaluation approach. Results of this approach were compared with the direct evaluation method. In this section, the two-level evaluation approach was also compared with the improved version of the method which was originally proposed in the previous research (Doornink,2006). Section 5.5 is dedicated to the many-to-one model approach. In Section 5.6, further studies to evaluate the relationship among the damage level, damage detection delay, and the group size selection for the direct evaluation method are described. Finally, this chapter is concluded with a brief summary.

5.2 FEA Procedure and Synthetic Data Generation

The finite element model described in Section 4.3.2 .2.1 was once again used in this portion of the work. The joint where the floor-beam was connected to the girder at Section C were re-meshed to accommodate small size cracks and to capture the complicated strain field at the cut-back areas more accurately. Figure 5.1 presents the refined mesh at the cut-back area of the south girder and the connection between the floor beam and the south girder. The north girder counterparts are symmetric. The finest mesh size was selected to be 0.25in. at the cut-back area.

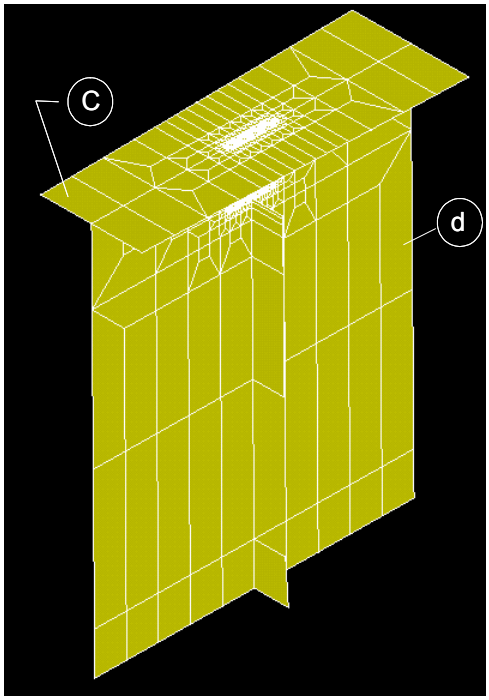

a. South girder at section C

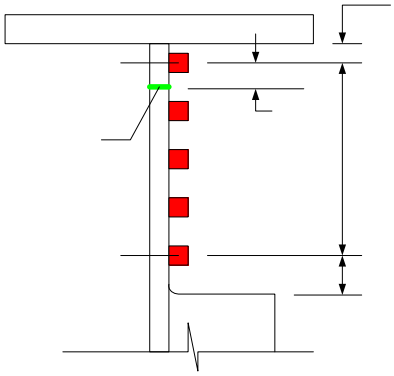

b. Position of the simulated cut-back area fatigue crack and sensing points

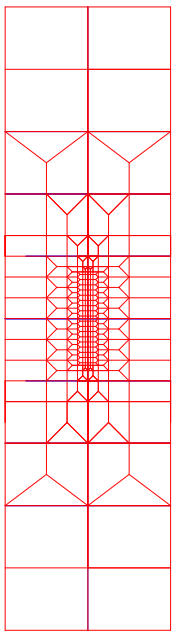

c. Mesh of the girder top flange

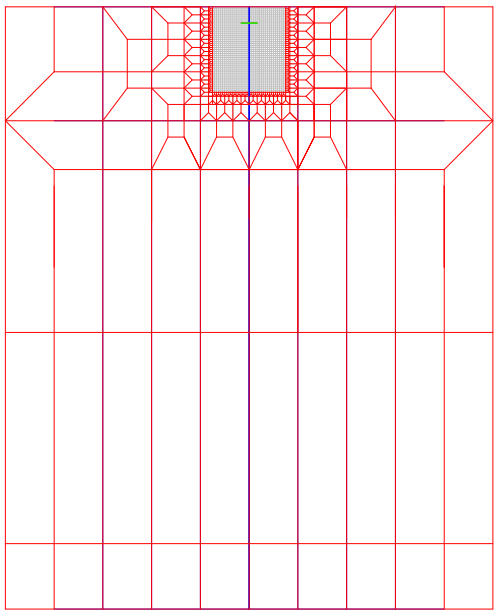

d. Mesh of the girder web

Figure 5.1 The refined model for the cut-back area at Section C

Before being used for the prediction of the damaged bridge response, the finite element model was verified for the undamaged state with field test data. The verification results are presented in

Section 5.2.1. After the verification, two types of damage, fatigue cracks at cut-back areas and corrosion damage at girder bottom, were introduced to the model. The details of the damage simulation procedure and the damage induced strain changes are discussed in Section5.2.2 and Section5.2.3.

5.2.1 Model Verification

The control dump truck (Dump4 in Table 4.1, Fig. 5.2 a) was simulated as six concentrated wheel loads (Fig. 5.2b). For simulation simplicity, the moving wheel loads were applied onto nodes of the model directly. Due to the mesh size of the bridge deck elements ($6in \times 6in$), instead of using the measured axle spacings (176in. and 56in.), spacings of 174in. and 54in. were used. In the following paragraphs, the field measured strains and the strains obtained from the FEA were compared for the girder bottom sensors, the floor-beam sensors, the horizontal and vertical stringer sensors, and the sensors located at the cut-back areas.

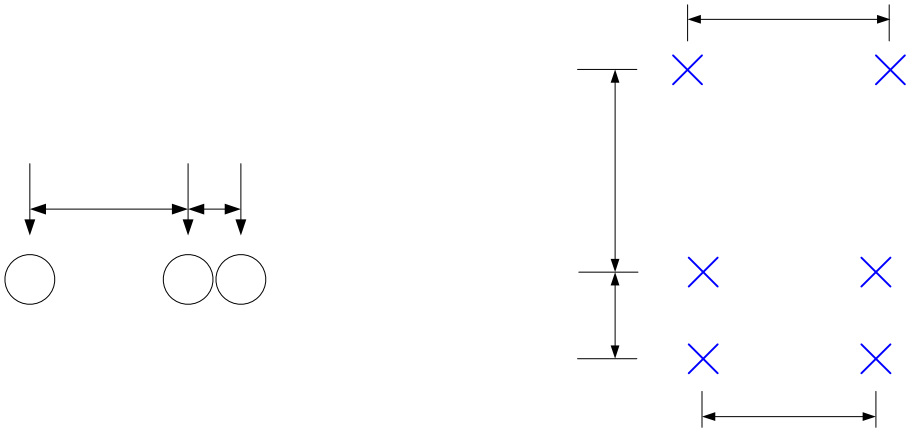

a. Control dump truck b. load model for the dump truck

Figure 5.2 Control dump truck and the load model

Girder bottom flange strains

The FEA results and the field data for the girder bottom sensors are plotted in Fig. 5.3. The field data set was produced at highway speeds as it was hard to find a crawl speed truck event when no other vehicles were on the bridge at the same time. The dynamic vibrations in the field data are obvious. However, the overall strain pattern and the magnitude of the extreme strains are generally well matched.

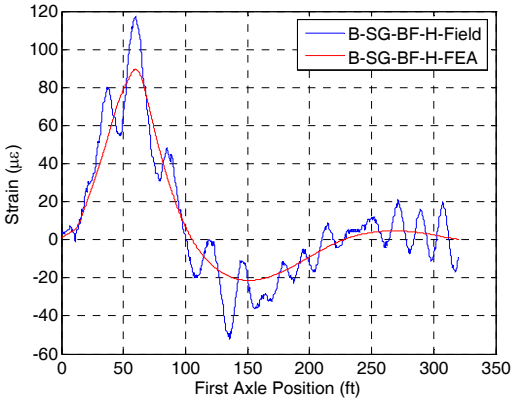

a. South girder Section B

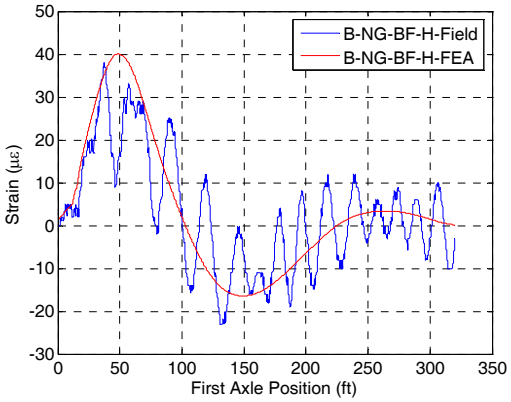

b. North girder Section B

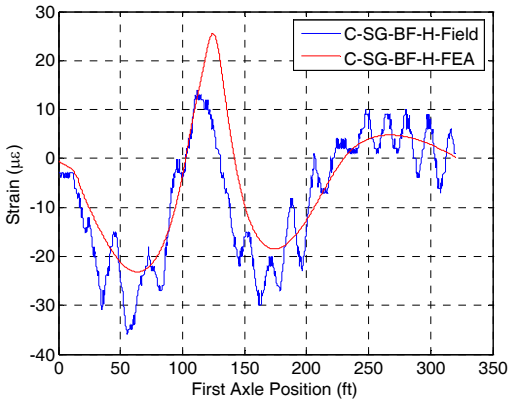

c. South girder Section C

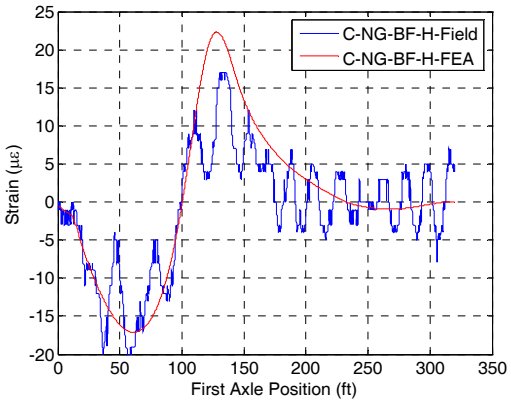

d. North girder Section C

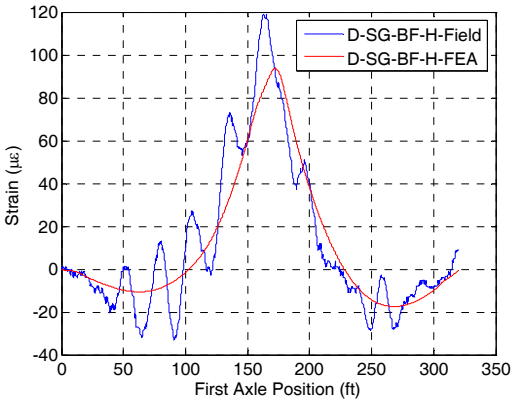

e. South girder Section D

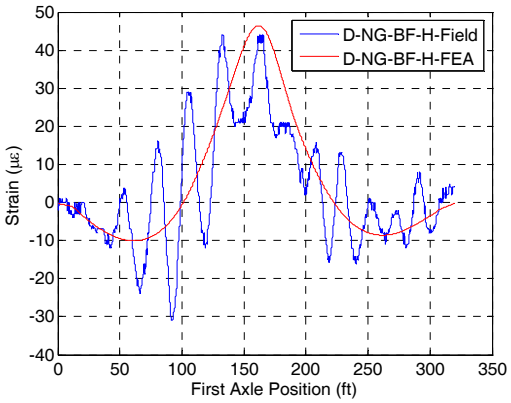

f. North girder Section D

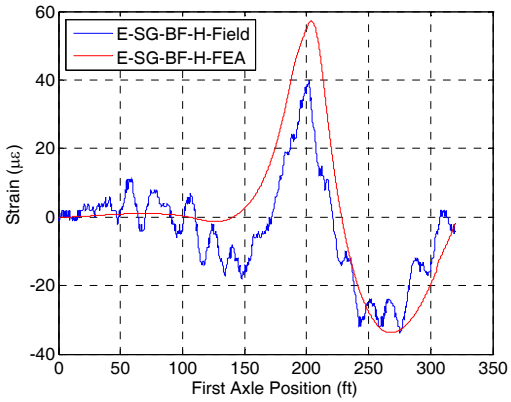

g. South girder Section E

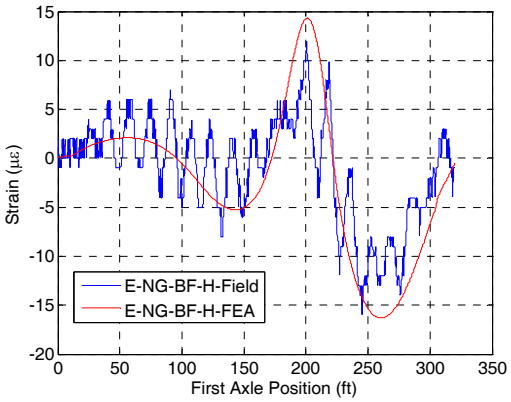

h. North girder Section E

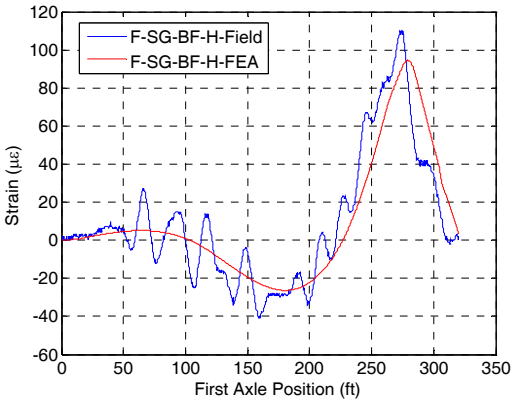

i. South girder Section F

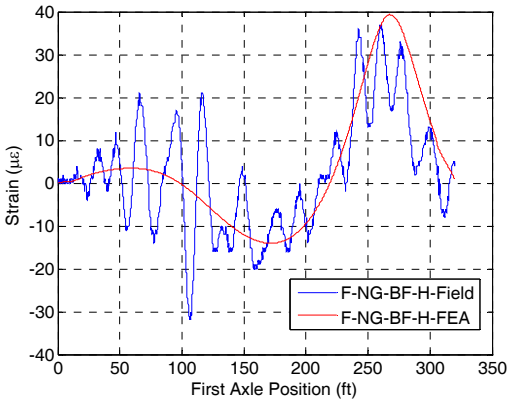

j. North girder Section F

Figure 5.3 The comparison of girder bottom flange strains

Floor beam strains

In Fig. 5.4, the field collected floor beam strains are compared with the FEA results. The sensors are located at Section C and Section E under the south stringer and north stringer, respectively. As can be seen from Fig. 5.4 a&c, the floor beam strains under south stringers match the FEA results very well. For the north side of the floor beams, the field collected data are approximately 50% of the theoretical data (Fig. 5.4 b&d). Many reasons can contribute to this. For example, the truck position in the model may not be exactly the same as its field position; the transverse wheel spacings of the truck model could be slight different to that of the real truck, and so on. As the difference is mainly caused by the load model, the overall performance of the bridge model is considered acceptable.

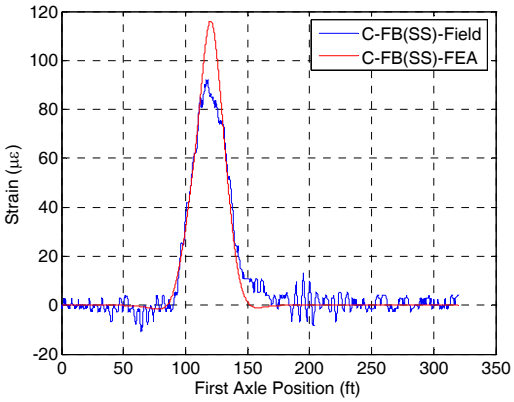

a. Section C floor beam under south stringer

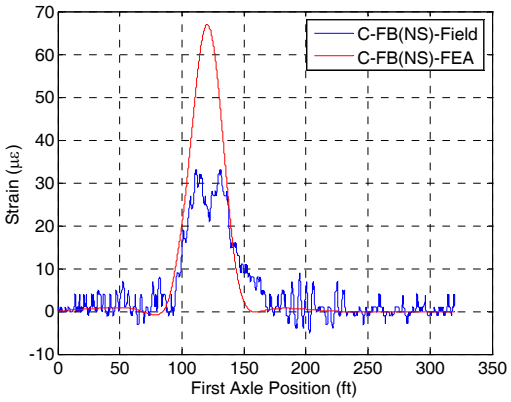

b. Section C floor beam under north stringer

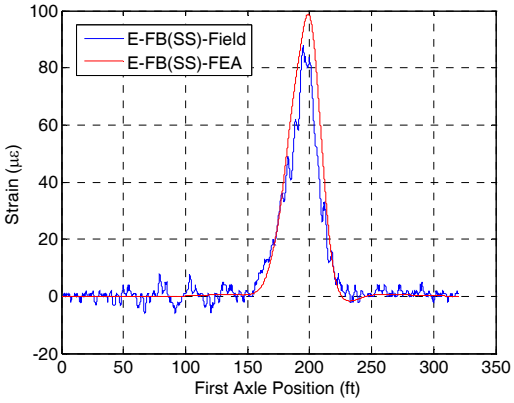

c. Section E floor beam under south stringer

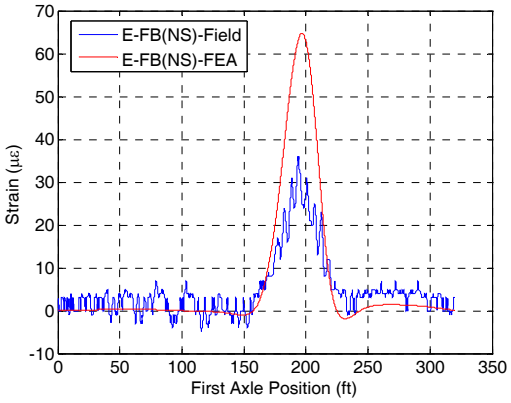

b. Section E floor beam under north stringer

Figure 5.4 The comparison of the strains for floor beams

Horizontal stringer strains

Figure 5.5 shows the strains collected by the bottom flange stringer sensors and the strains obtained from the FEA. It can be seen that the FEA results consistently show a slightly larger maximum event strain. This is because the composite action effects between the bridge deck and stringers are not perfectly simulated by the model. However, considering the good match of the overall strain patterns, the model is considered sufficient for stringer bottom flange strain analysis.

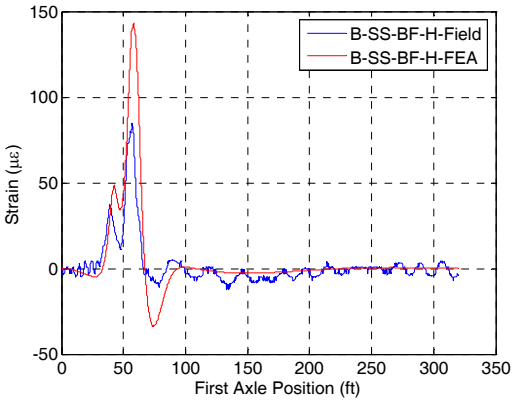

a. South stringer Section B

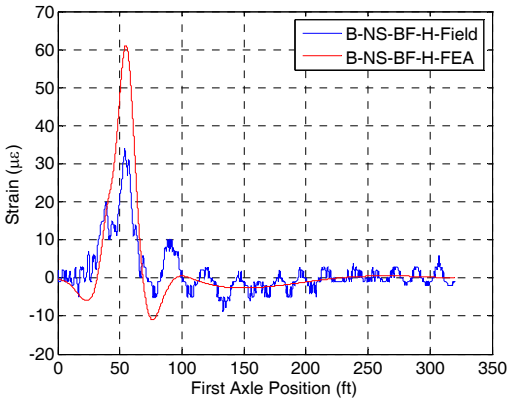

b. North stringer Section B

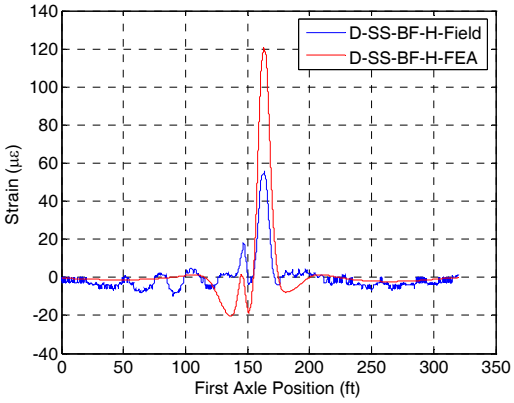

c. South stringer Section D

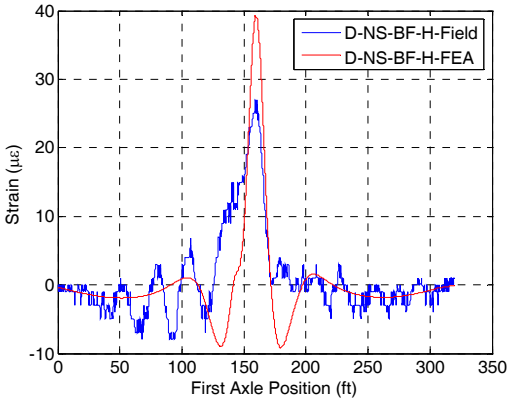

d. North stringer Section D

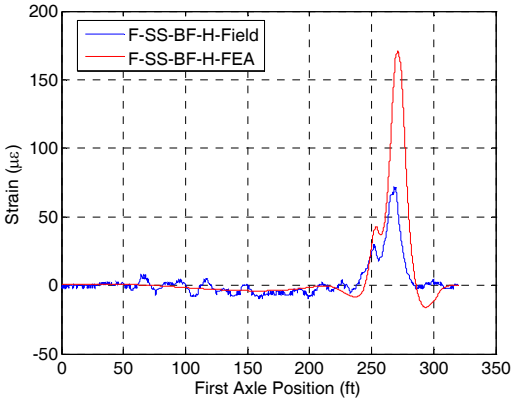

e. South stringer Section F

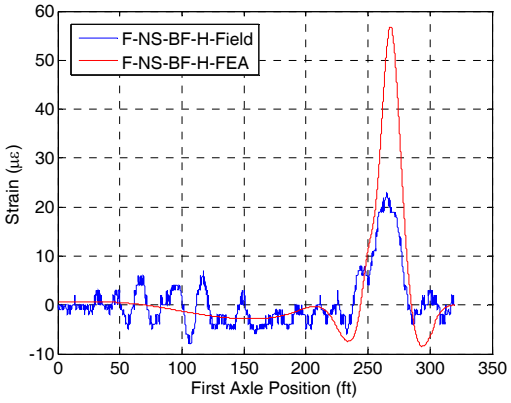

f. North stringer Section D

Figure 5.5 The comparison of stringer bottom flange strains

Vertical stringer strains

Figure 5.6 presents the strains collected by the sensors located at the web of the stringers and the vertical strains obtained from the FEA. The differences between the field collected data and the FEA results are quite large. It was observed that eh strain gradient in this area is quite large; as such a small difference between the actual sensor position and its nominal position can cause significant differences. In the simulation, the nominal sensor position data were used which may not necessarily represent the real sensor position well. Therefore, the inconsistency between the FEA results and the field collected data shown in Fig. 5.6 was not considered to be caused by the inaccuracy of the model.

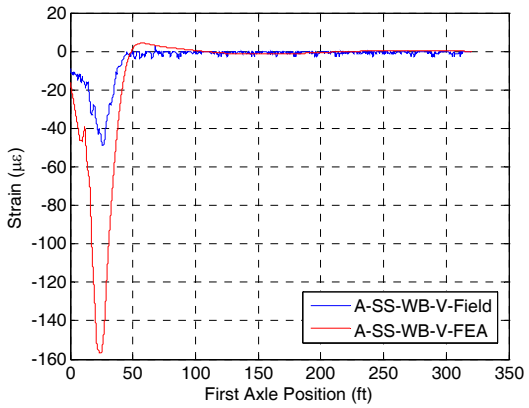

a. South stringer Section A

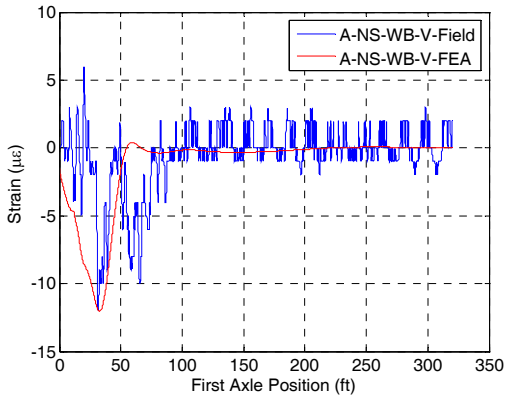

b. North stringer Section A

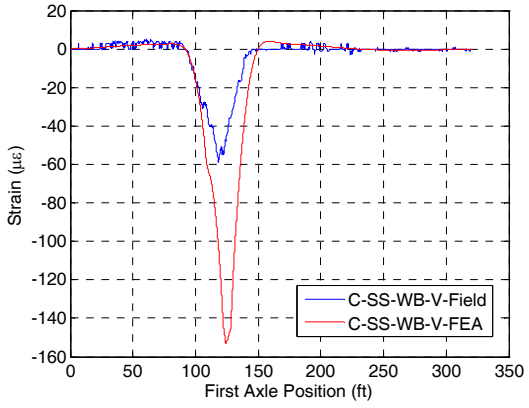

c. South stringer Section C

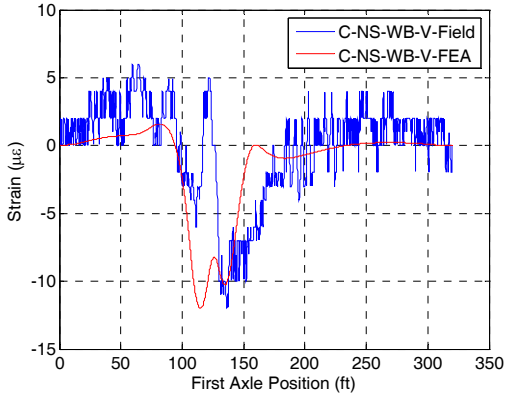

d. North stringer Section C

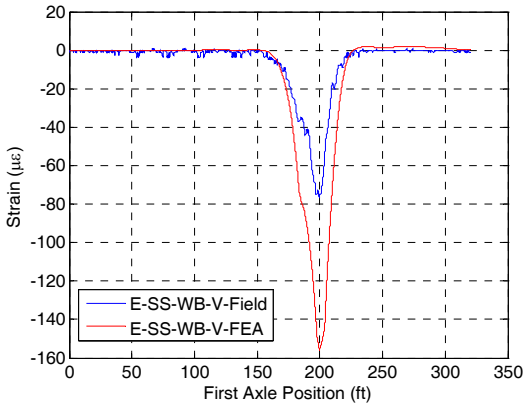

c. South stringer Section E

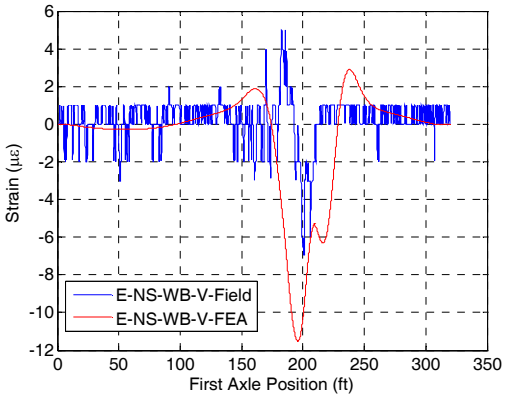

d. North stringer Section E

Figure 5.6 The comparison of vertical stringer web strains

Cut-back area strains

Figure 5.7 compares the cut-back area strains obtained from the FEA and the field test results. The figure shows that the theoretical strain patterns match the field data well. The difference between the magnitudes of the extreme strains can be caused by non-exact sensor position coupled with the complicated strain field at the cut-back areas. The comparison shows that the model can generally represent the structural performance at the cut-back areas.

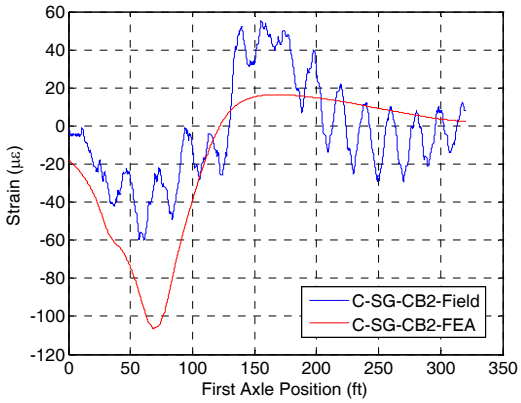

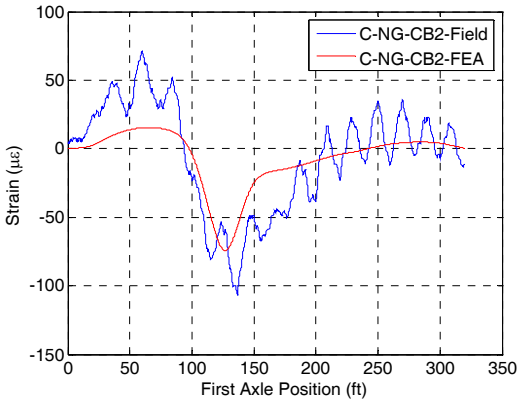

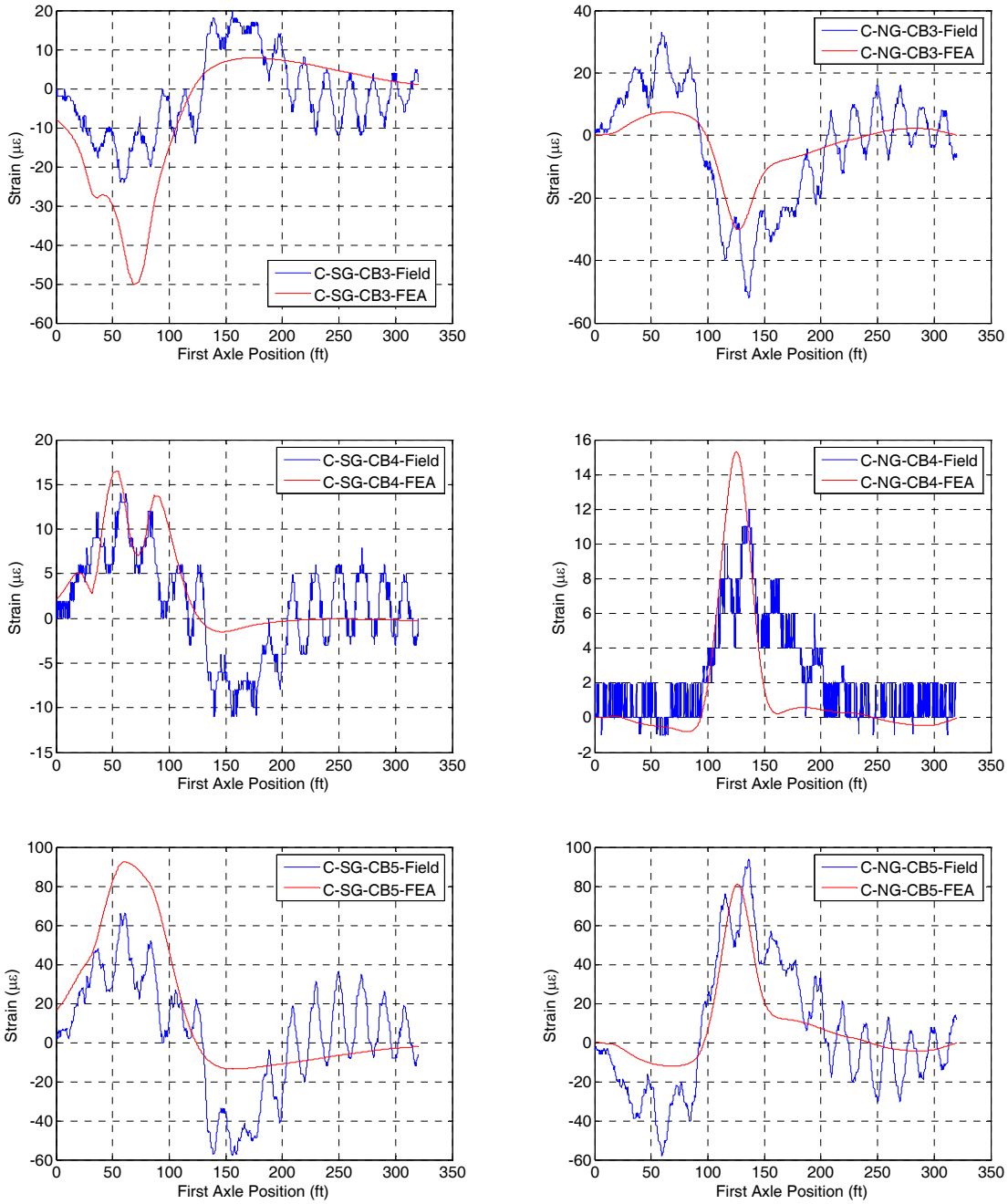

a. strains for the south cut-back area

b. strains for the north cut-back area

Figure 5.7 The comparison of strains at cut-back areas

In summary, the verification indicated that the over all performance of the finite element model can represent the bridge fairly well. Although the model does not provide the exact replication of the measured data, it can produce comparable data which may be used to test the various analysis algorithms.

5.2.2 Damage Simulation

During damage simulation, a right lane, five-axle, heavy, semi truck was modeled and used as the load condition for all structural states. In particular, the standard Iowa DOT 3S2A truck was used (Fig. 5.8). Two types of damage were simulated: 1) Fatigue crack with different sizes at the Section C cut-back area of south girder. 2) Corrosion damage at the south girder bottom flange near Section B.

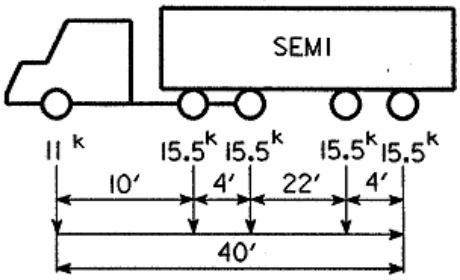

Figure 5.8 Load model used in the damage simulation

5.2.2.1 Fatigue Cracks at the Cut-back Area

Cracks, with size varying from 0in. to 2in. in 0.25in. increments, were introduced to the middle of C-SG-CB1 and C-SG-CB2 (Fig. 5.1b & d, 1in. away from both sensors). For all the simulated fatigue crack damage states, the strain responses associated with representative sensors are plotted in Figs. 5.9 to 5.13. Specifically, Fig. 5.9 shows the strains for the sensors located at both south and north cut-back areas; Figs. 5.10 to 5.13 show the strains for selected girder bottom sensors, floor beam bottom sensors, and horizontal and vertical stringer sensors. It can be seen that the cracks affected the strain responses at the sensors located neat the crack. For C-SG-CB(1)-V and C-SG-CB(2)-V, the damage caused strain changes are pretty significant while the changes are very small for C-SG-CB(3)-V and C-SG-CB(4)-V (Fig. 5.9). Generally, the introduced crack did not change the strain responses for other sensors (Fig. 5.9 to 5.13). As shown in Fig. 5.9 for sensors C-SG-CB(1-3)-V, as the crack size increases, the event maximum strain gets smaller while the event minimum strain gets larger. The opposite trend can be seen for sensor C-SG-CB(4)-V because it is located at the other side of the zero strain point. However, since sensor C-SG-CB(3)-V and C-SG-CB(4)-V are near to the neutral point, the absolute value of the extreme event strains are small, and in addition, the damage caused strain changes are pretty small for these two sensors. Among the simulated fatigue cracks, six were employed to illustrate and verify of the proposed damage detection approaches. The six damage states (Level0 to Level5) and the corresponding crack sizes are listed in Table 5.1. Table 5.2 summarizes the event extreme strains (maximum and minimum strains) for sensors C-SG-CB(1-5)-V

at the six different structural states. Table 5.3 shows the percentage of the strain changes with respect to the non-damaged strain.

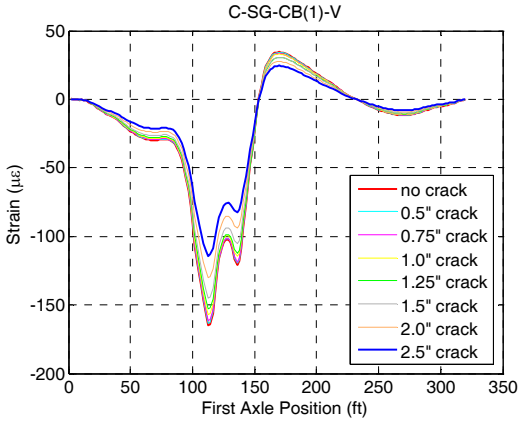

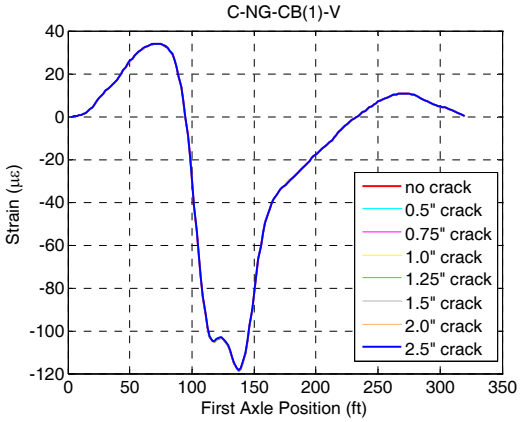

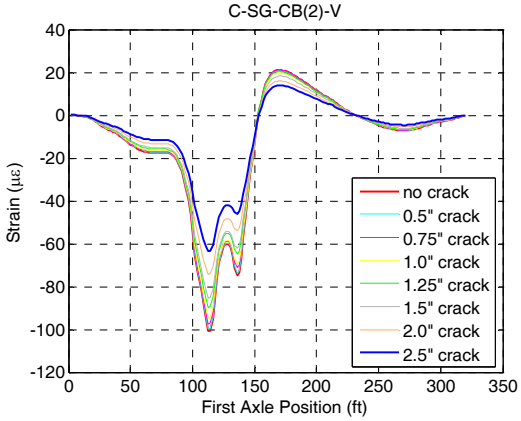

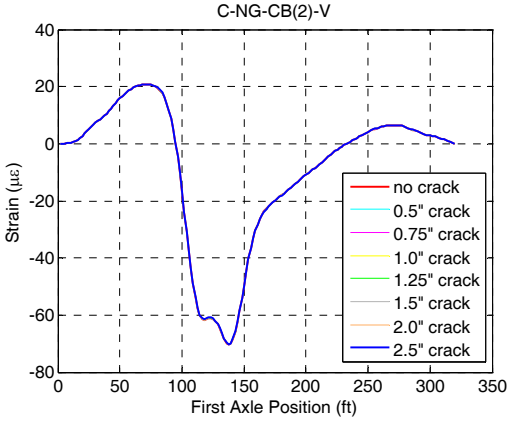

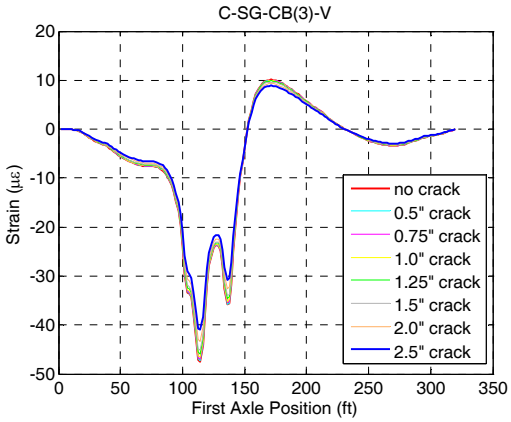

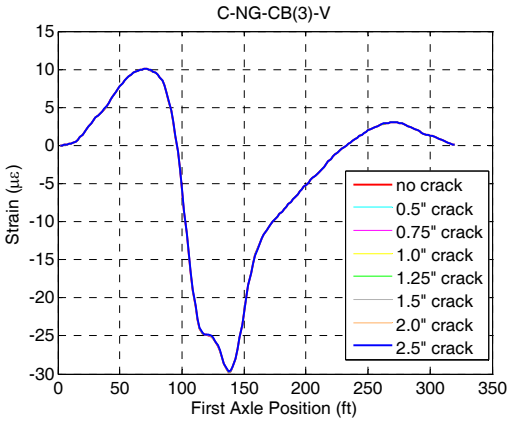

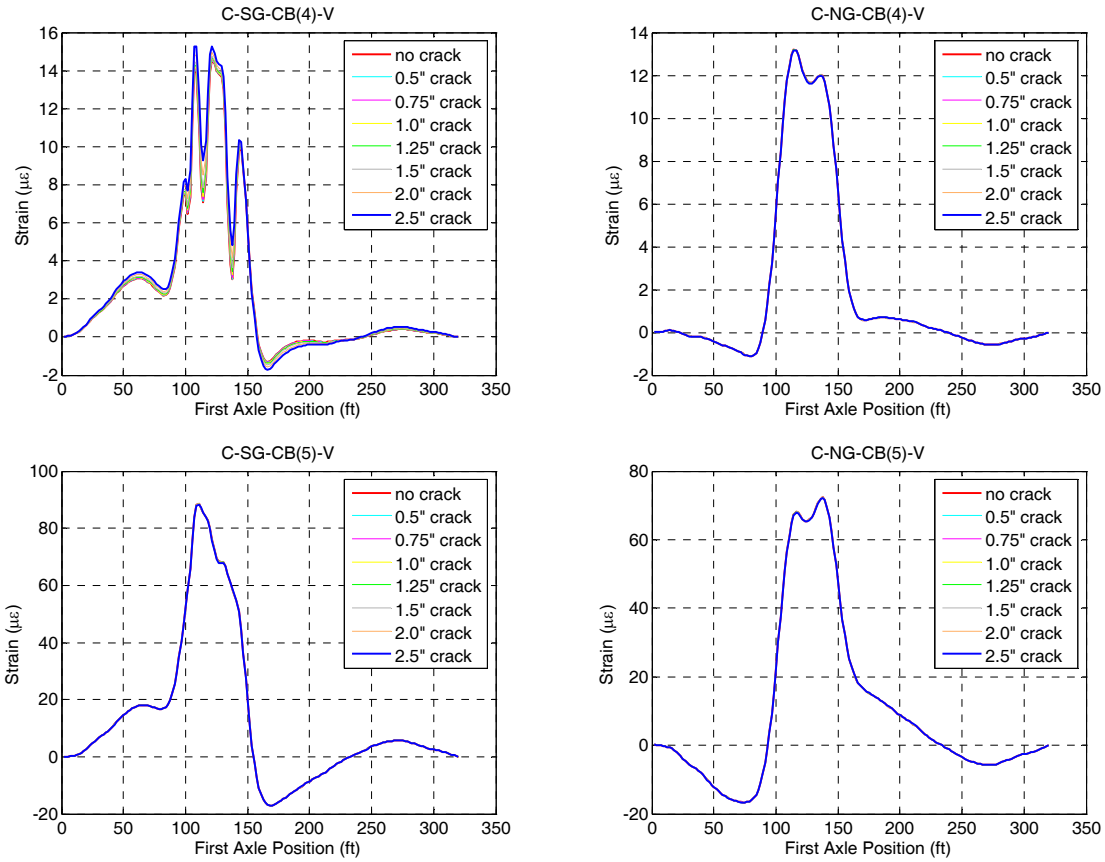

Figure 5.9 Strains associated for the cut-back area sensors

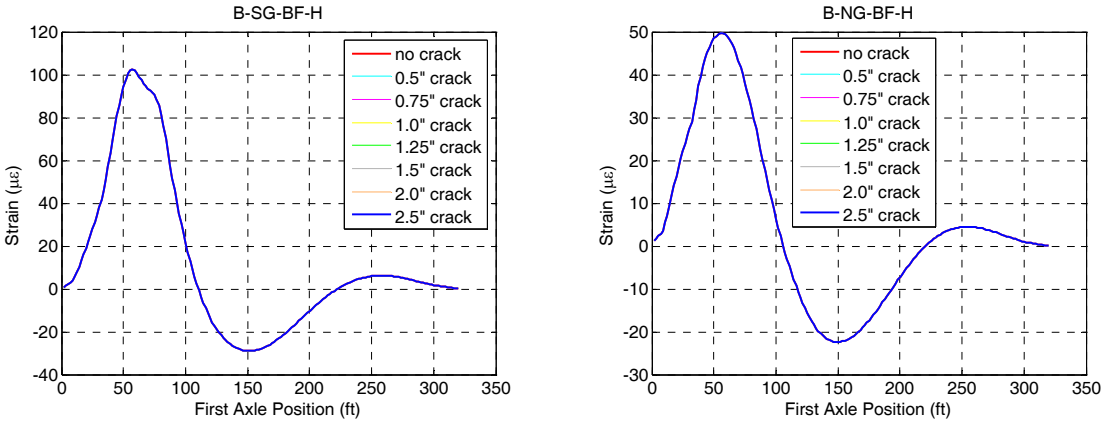

Figure 5.10 Strains for the selected girder bottom sensors

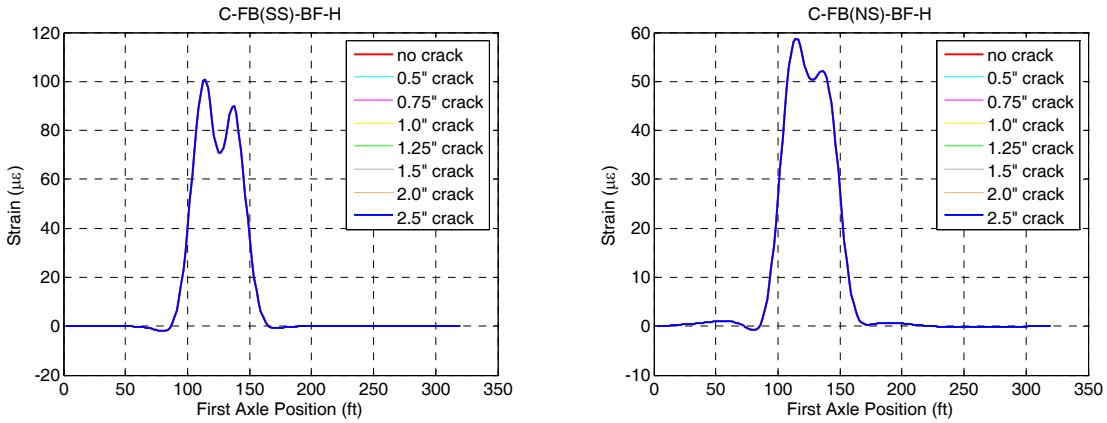

Figure 5.11 Strains for the selected floor beam bottom sensors

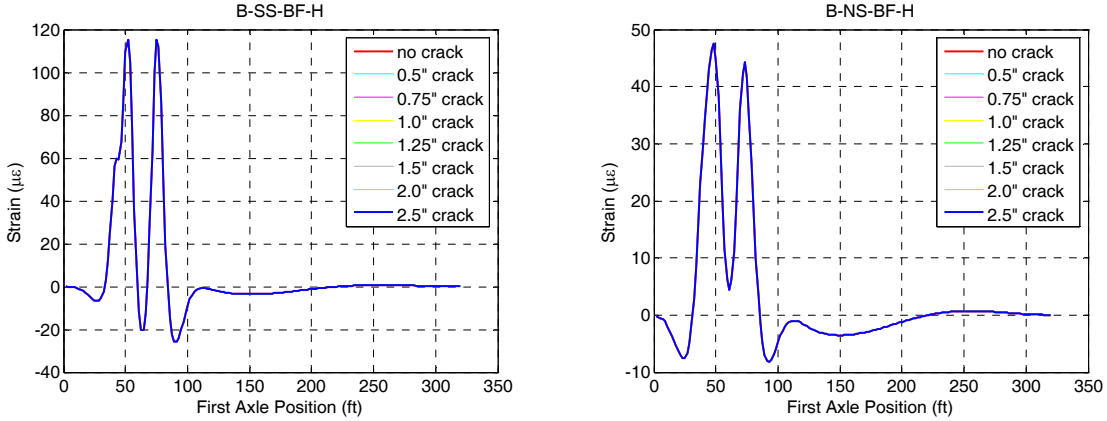

Figure 5.12 Strains for the selected stringer bottom sensors

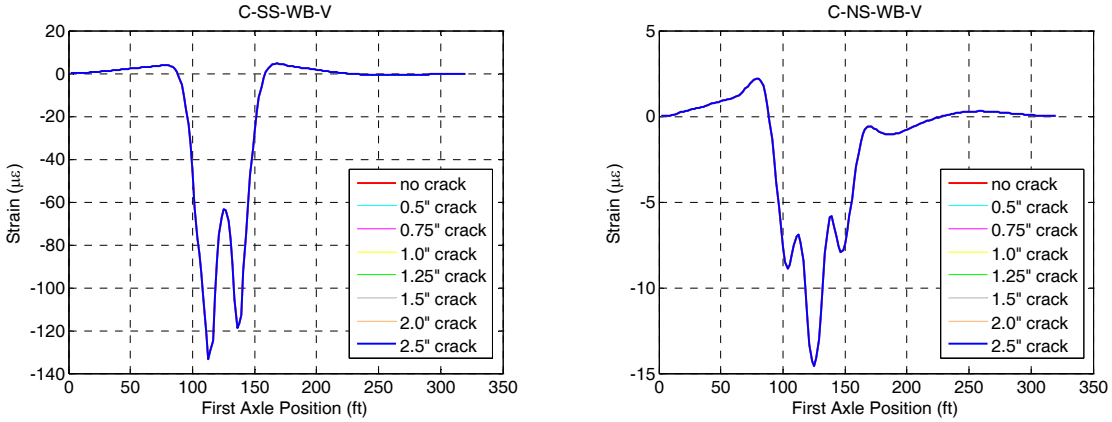

Figure 5.13 Strains associated for the selected stringer web vertical sensors

Table 5.1 Damage level and the corresponding crack size

Damage Level	Level0	Level1	Level2	Level3	Level4	Level5
Crack size (in.)	0	0.5	0.75	1	1.25	1.50

Table 5.2 Maximum and minimum strain at vicinity sensors for different damage levels (3S2A)

Structural states	Max strain $(\mu\varepsilon)$				
	C-SG-CB(1)-V	C-SG-CB(2)-V	C-SG-CB(3)-V	C-SG-CB(4)-V	C-SG-CB(5)-V
Level0	34.47	21.14	10.06	14.55	88.47
Level1	34.25	20.95	10.04	14.55	88.47
Level2	33.16	21.17	10.01	14.59	88.47
Level3	33.08	20.02	9.90	14.62	88.47
Level4	30.58	20.52	9.87	14.70	88.47
Level5	30.71	18.23	9.65	14.77	88.46
	Min strain $(\mu\varepsilon)$				
Level0	-164.77	-100.89	-47.49	-1.31	-17.01
Level1	-163.51	-99.81	-47.33	-1.32	-17.01
Level2	-161.43	-97.46	-47.01	-1.33	-17.01
Level3	-157.20	-94.70	-46.56	-1.36	-17.01
Level4	-152.68	-89.76	-45.88	-1.38	-17.00
Level5	-145.07	-85.37	-45.18	-1.44	-17.01

Table 5.3 Percentages of damage caused maximum and minimum strain changes

Structural states	δ_max (%)				
	C-SG-CB(1)-V	C-SG-CB(2)-V	C-SG-CB(3)-V	C-SG-CB(4)-V	C-SG-CB(5)-V
Level0	0.00%	0.00%	0.00%	0.00%	0.00%
Level1	-0.64%	-0.89%	-0.25%	0.06%	0.00%
Level2	-3.81%	0.13%	-0.54%	0.27%	0.00%
Level3	-4.04%	-5.29%	-1.60%	0.53%	-0.01%
Level4	-11.29%	-2.93%	-1.92%	1.09%	-0.01%
Level5	-10.90%	-13.77%	-4.07%	1.51%	-0.01%
	δ_min (%)				
Level0	0.00%	0.00%	0.00%	0.00%	0.00%
Level1	0.77%	1.08%	0.32%	-0.65%	0.00%
Level2	2.03%	3.40%	1.00%	-1.57%	0.01%
Level3	4.59%	6.14%	1.94%	-4.07%	0.00%
Level4	7.33%	11.04%	3.38%	-5.46%	0.04%
Level5	11.95%	15.38%	4.86%	-10.31%	0.00%

5.2.2.2 Corrosion Damage at South Girder Bottom Flange

For this analysis, damage was introduced to the bottom flange of the south girder, the entire width of the bottom flange and six inch from sensor B-SG-BF-H (elements 4051 and 4052 shown in Fig. 5.14). Three levels of corrosion were simulated by changing the thickness of the elements from 1.50in. to 1.25 in., 1in., and 0.75in., and they are indicated as Corrosion1, Corrosion2, and Crosion3 accordingly. FEA results show that only sensors B-SG-BF-H and B-NG-BF-H were affected by the simulated corrosion damages, and their strains associated with all the damage levels are shown in Fig. 5.15. Similarly, Table 5.4 summarizes the extreme event strains for these two sensors and the percentage change with damage. As the corrosion causes cross section loss, the maximum event strain increases while the minimum strain decreases for both sensor B-SG-BF-H and B-NG-BF-H.

Table 5.4 Maximum and minimum strain for damage affected sensors and change percentages

Thickness of bottom flange (in.)	Max strain $(\mu\varepsilon)$		δ_max (%)	
	B-SG-BF-H	B-NG-BF-H	B-SG-BF-H	B-NG-BF-H
1.50 (No damage)	102.55	49.64	0.00%	0.00%
1.25 (Crossion1)	110.60	53.54	7.85%	7.87%
1.00 (Crossion2)	121.72	58.94	18.69%	18.75%
0.75 (Crossion3)	138.19	66.95	34.75%	34.88%
	Min strain $(\mu\varepsilon)$		δ_min (%)	
1.50 (no damage)	-29.05	-22.42	0.00%	0.00%
1.25 (Crossion1)	-31.34	-24.19	7.87%	7.88%
1.00 (Crossion2)	-34.49	-26.63	18.74%	18.77%
0.75 (Crossion3)	-39.17	-30.24	34.85%	34.90%

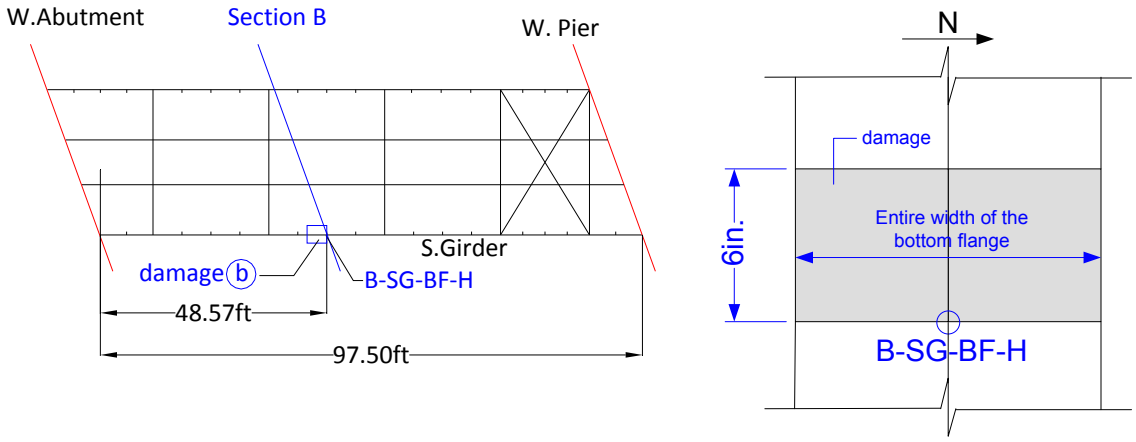

a. Position of the damage b. Size of the damage

Figure 5.14 Position and size of the simulated girder bottom flange corrosion damage

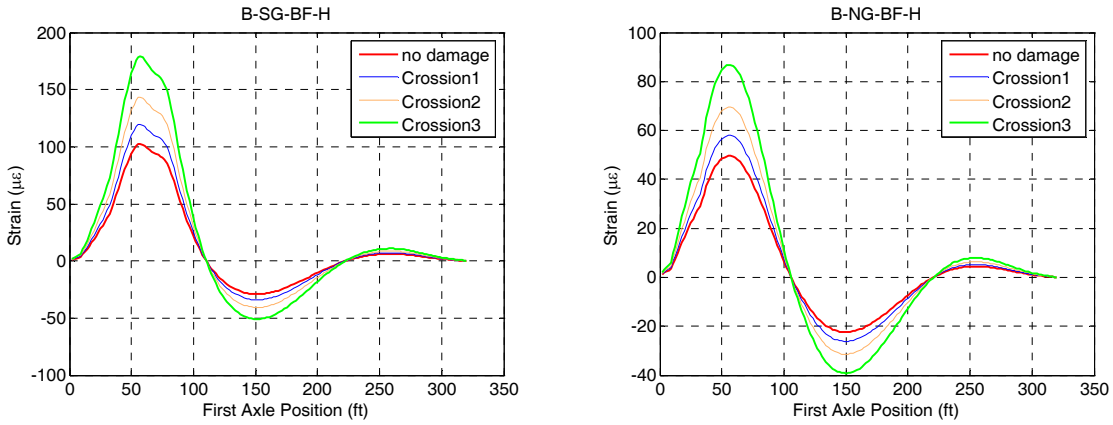

Figure 5.15 Comparison of the strains for affected sensors with different corrosion damages

5.2.3 The Synthetic Data Generation

After obtaining the FEA strain data for a particular damage condition, they were used along with the field collected data (which represents the un-damaged bridge) to simulate/estimate the strain responses of the damaged bridge. Two major steps were involved in the synthetic data generation procedure :1) calculate damage induced strain change (as a percentage) for each sensor from the FEA results, and 2) multiply field collected data by the percent change to estimate the damaged condition response data sets. For example, as shown in Tables 5.1 and 5.2, when a one inch crack happens between sensor C-SG-CB(1)-V and C-SG-CB(2)-V, the maximum strain for C-SG-CB(1)-V

reduced 4.04%. The synthetic data were generated by multiplying the baseline data collected by C-SG-CB(1)-V with 95.96% (0.9596). The procedure was repeated for all sensors. The synthetic data were used in the following damage detection discussions.

5.3 Damage Detection Method One (one-to-one model, direct evaluation method)

As described before, the developed SHM system includes 48 strain sensors, among them, 40 were distributed along the girders, floor-beams and stringers, and they are primarily installed for monitoring bridge performance. For such a system, 1600 one-to-one model can be created among the 40 sensors. The models then, in turn, were used to calculate a 40×40 residual matrix for each truck event, which is the basic format of the damage indictor used in the damage detection approaches described in this section and in Section 5.4.

For the approach described here, the residual matrix was further simplified into a forty degree vector, so that, each sensor is associated with a single element of the vector, and one control chart can be created for each sensor. The control chart results, thus, directly indicate not only the occurrence of damage but the general damage area. Three residual matrix simplification methods were studied. In the first two simplification methods, the residual matrix was summed either row-wisely or column-wisely to generate a row-sum-residual or a column-sum-residual vector. The third method was developed by subtracting the column-sum-residual from row-sum-residual and, thus, creating a combine-sum-residual vector. The dimensions of the three sum-residual vectors are all equal to the number of sensors.

The one-to-one model creation, residual calculation, residual simplification, control chart construction, and the control chart result interpretation and discussion will be presented in the following.

5.3.1 One-to-One Models and Residual Calculation

It was shown in Chapter 4 that generally linear relationships exist between the extreme event strains (both maximum and minimum strains) of any two sensors when some truck and truck position variations have been eliminated. If the extreme strains are utilized in the one-to-one prediction model creation, four models (e.g. max-max model, max-min model, min-max model, and min-min model) can be obtained. As an example, Fig. 5.16 presents the four models created

between sensor B-SG-BF-H and C-SG-CB(1)-V using the data produced by right-lane, five-axle semi truck events. The model can be mathematically expressed as Eq.5.1, in which, sensor B-SG-BF-H is called the control sensor, and C-SG-CB(1)-V is called the response sensor. The coefficients, a_0 and a_1, were determined from the training data by a standard least square linear regression algorithm. The residual, as defined in Eq.5.2, is the difference between the predicted and the recorded strain of the response sensor.

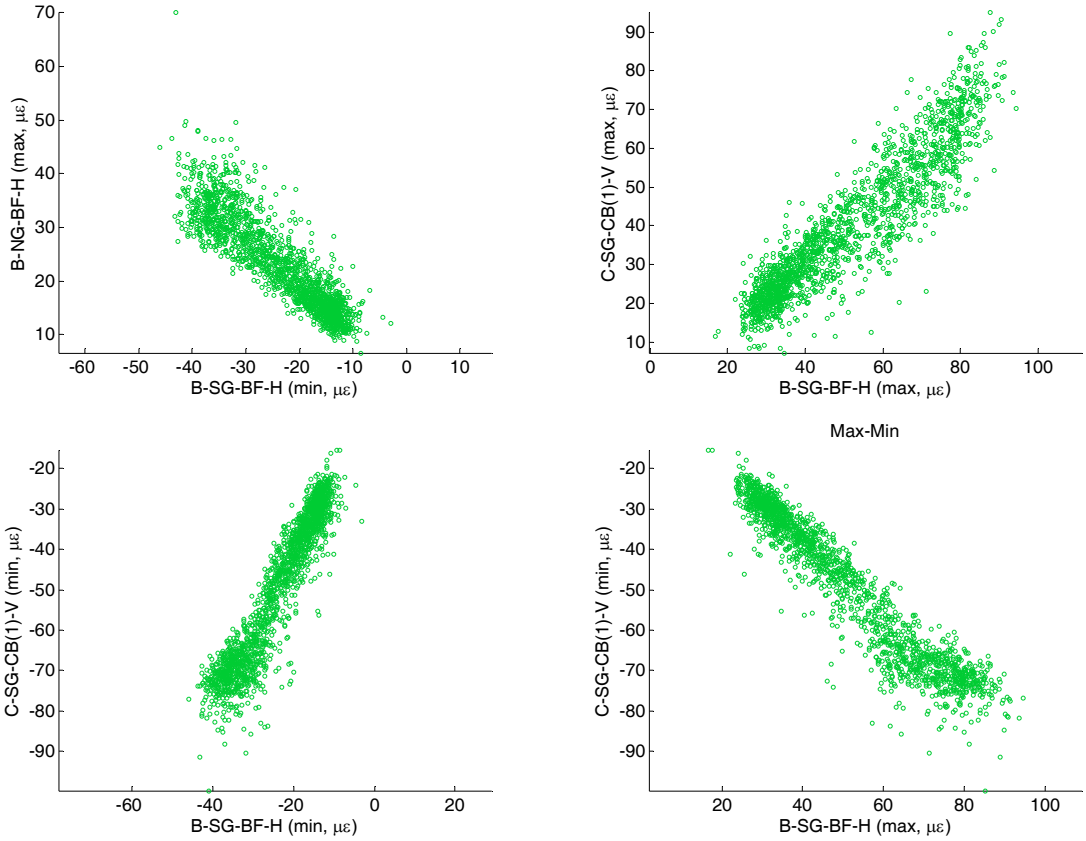

Figure 5.16 Example of the relationship of maximum and minimum event strain of two sensors

$$\varepsilon_{\text{C-SG-CB(1)-V,max/min,}predict} = a_0 + a_1 \varepsilon_{B-SG-BF-H,\text{max/min}} \qquad \text{Eq.5.1}$$

$$\text{Re}\,sidual = \varepsilon_{\text{C-SG-CB(1)-V,max/min,}monitor} - \varepsilon_{\text{C-SG-CB(1)-V,max/min,}predict} \qquad \text{Eq.5.2}$$

in which, $\varepsilon_{B-SG-BF-H,\text{max/min}}$ and $\varepsilon_{B-NG-BF-H,\text{max/min}}$ are the extreme event strain values of sensor B-SG-BF-H and B-NG-BF-H ;

a_0 and a_1 are coefficients;

Generalizing the control sensor (B-SG-BF-H) and response sensor (C-SG-CB(1)-V) in Eq. 5.1 & 5.2 into any sensor within the system, the equations can be rewritten as Eq.5.3a and Eq.5.3b, respectively. To be more intuitive, the matrix format of the residual is shown in Eq.5.3. Eq.5.3a can be any of the four prediction models (max-max, max-min, min-min, and min-max). There is no simple qualitative way to determine which model is the best in terms of the damage sensitivity. However, the FEA results showed that a crack near a sensor can cause the event maximum strain to decrease while the minimum strain increases. Therefore, the event strain range (max-strain – min-strain) will decrease due to the damage, and the decrease combines the changes in both the maximum strain and minimum strain. Intuitively therefore a strain range model may be more sensitive to damage than extreme strains alone. Figure 5.17 presents the relationship of event strain range between B-SG-BF-H and C-SG-CB(1)-V. The linear pattern of the relationship is evident. Therefore, the linear regression method used to construct the extreme strain models is applicable for strain range prediction model creation as well. The strain range model obtained from heavy trucks, light trucks and all trucks (trucks are used here and later refer to right-lane, five-axle semi) are also shown in Fig. 5.17. The slight differences of the three models indicate that classifying the trucks into weight groups is necessary, the simulation results and further discussions about this issue will be presented in Section5.2.4.

$$S_{pred,ij} = f(S_j) = a_{0,ij} + a_{1,ij} \times S_j \qquad \text{Eq.5.3a}$$

$$R_{ij} = S_i - S_{prd,ij} = S_i - (a_{0,ij} + a_{1,ij} \times S_j) \qquad \text{Eq.5.3b}$$

$$\begin{bmatrix} R_{11} & .. & R_{1j} & .. & R_{140} \\ : & : & : & : & : \\ R_{i1} & .. & R_{ij} & .. & R_{i40} \\ : & : & : & : & : \\ R_{401} & .. & R_{40j} & .. & R_{4040} \end{bmatrix} = \begin{bmatrix} S_1 & .. & S_1 & .. & S_1 \\ : & : & : & : & : \\ S_i & .. & S_i & .. & S_i \\ : & : & : & : & : \\ S_{40} & .. & S_{40} & .. & S_{40} \end{bmatrix} - \left(\begin{bmatrix} a_{0,11} & .. & a_{0,1j} & .. & a_{0,140} \\ : & : & : & : & : \\ a_{0,i1} & .. & a_{0,ij} & .. & a_{0,i40} \\ : & : & : & : & : \\ a_{0,401} & .. & a_{0,40j} & .. & a_{0,4040} \end{bmatrix} + \begin{bmatrix} a_{1,11} & .. & a_{1,1j} & .. & a_{1,140} \\ : & : & : & : & : \\ a_{1,i1} & .. & a_{1,ij} & .. & a_{1,i40} \\ : & : & : & : & : \\ a_{1,401} & .. & a_{1,40j} & .. & a_{1,4040} \end{bmatrix} \begin{bmatrix} S_1 & 0 & 0 & .. & 0 \\ : & : & : & : & : \\ 0 & 0 & S_j & .. & 0 \\ : & : & : & : & : \\ 0 & 0 & .. & 0 & S_{40} \end{bmatrix} \right)$$

Eq.5.3

in which, $i, j = 1,..,40$;

R_{ij} is the residual when use the data of the j-th sensor to predict the data of the i-th sensor. When i = j, $R_{ij} = 0$;

S_j can be the event based max-strain, min-strain, or the strain range for the j-th sensor; $a_{0,ij}$ and $a_{1,ij}$ are the coefficients obtained from linear regression.

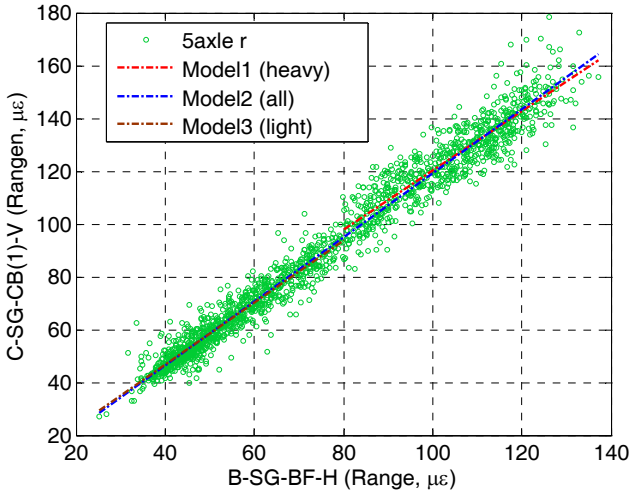

Figure 5.17 Example of the relationship of event strain range of two sensors

5.3.2 Residual Matrix Simplification

5.3.2.1 Row Summation

If damage affects the strain response of the p-th sensor (S_p) only (the change is high lighted by the red frame and green frame at the right side of Eq.5.4), it will cause all the elements in the p-th row (red frame at the left side of Eq.5.4) and the p-th column (green frame at the left side of Eq.5.4) of the residual matrix to change, except for R_{pp}, which always equals 0.

$$R_{pj}\begin{bmatrix} 0 & .. & R_{1p} & .. & R_{140} \\ : & : & : & : & : \\ R_{p1} & .. & 0 & .. & R_{p40} \\ : & : & : & : & : \\ R_{401} & .. & R_{40p} & .. & 0 \end{bmatrix} = \begin{bmatrix} S_1 & .. & S_1 & .. & S_1 \\ : & : & : & : & : \\ S_p & .. & S_p & .. & S_p \\ : & : & : & : & : \\ S_{40} & .. & S_{40} & .. & S_{40} \end{bmatrix}$$

$$- \left(\begin{bmatrix} a_{0,11} & .. & a_{0,1p} & .. & a_{0,140} \\ : & : & : & : & : \\ a_{0,p1} & .. & a_{0,pp} & .. & a_{0,p40} \\ : & : & : & : & : \\ a_{0,401} & .. & a_{0,40p} & .. & a_{0,4040} \end{bmatrix} + \begin{bmatrix} a_{1,11} & .. & a_{1,1p} & .. & a_{1,140} \\ : & : & : & : & : \\ a_{1,p1} & .. & a_{1,pp} & .. & a_{1,p40} \\ : & : & : & : & : \\ a_{1,401} & .. & a_{1,40p} & .. & a_{1,4040} \end{bmatrix} \begin{bmatrix} S_1 & 0 & 0 & .. & 0 \\ : & : & : & : & : \\ 0 & 0 & S_p & .. & 0 \\ : & : & : & : & : \\ 0 & 0 & .. & 0 & S_{40} \end{bmatrix} \right)$$

Eq.5.4

Notice that S can be either strain range or extreme strain (e.g. maximum or minimum strain). When different data (strain range or extreme strains) are used, and when the relative location of the sensor and the damage are different (sensor near to the damage or over the damage), S_p can be either decreased or increased due to the damage, and thus, elements of R_{pj} (the p-th row of the residual matrix) can either decrease or increase as well; nevertheless, in any of the cases, elements of the R_{pj} share the same change trend as S_p. Therefore, the summation of R_{pj} is thought to enlarge the damage effect.

During implementation, it should be noted that if the absolute value of $a_{1,qp}$ is large, the change of S_p can lead to a significant change of $S_{pred,qp}$, and which in turn, results in remarkable change of $row\_sum\_rsd_q$. In this case, damage would be indicated not only for the p-th sensor but the q-th sensor. In this scenario, the damage location is not correctly determined. To avoid this, the elements in the residual matrix were standardized using Eq.5.5. The mean and standard deviation of each element of residual matrix was determined from the training data sets. After the standardized residual matrix is obtained, each row can be summed up to get the row_sum_rsd vector (Eq.5.6). In the rest of this section, for simplicity, residual matrix refers to the standardized residual matrix.

$$R_{ij,std} = \frac{R_{ij} - \mu_{ij}}{\sigma_{ij}} \quad \text{(i, j = 1 to 40)} \qquad \text{Eq.5.5}$$

in which, R_{ij} is the element located at i-th row and j-the column in residual matrix;
μ_{ij} is the mean of R_{ij};
σ_{ij} is the standard deviation of R_{ij}.

$$row\_sum\_rsd_i = \sum_{j=1}^{40} R_{ij,std} \quad \text{(i = 1 to 40)} \qquad \text{Eq.5.6}$$

5.3.2.2 Column Summation

As mentioned before, when damage affects S_p, it affects not only the elements of R_{pj} but the elements of R_{ip} (see Eq.5.4, the p-th column of the residual matrix). The change trend (increase or decrease) of elements of R_{ip} is not only related to the change of S_p but $a_{1,ip}$. If $a_{1,ip}$ are all positive or negative, all elements of R_{ip} show the same change trend. For a linear structural system, the

strain range of all sensors are positively correlated to the magnitude of the load, and thus, the strain of p-th sensor and i-th sensor are positively correlated, so $a_{1,ip}$ are all positive. However, if extreme strains are used, this is not always true. For an example, in a max-max model using B-SG-BF-H as the variable sensor, most elements of $a_{1,i4}$ are positive, but when E-NG-CB(5)-V is used as the response sensor, $a_{1,i4}$ (i = 28) is negative. In the case that $a_{1,ip}$ contains both negative and positive elements, the summation procedure will reduce the damage effect. Therefore, the column summation is applicable for a strain range model only. Again, the summation should be performed against the normalized data (Eq.5.7).

$$column\_sum\_rsd_j = \sum_{i=1}^{40} R_{ij,std} \quad (j = 1 \text{ to } 40) \qquad \text{Eq.5.7}$$

5.3.2.3 Combined Summation

For the strain range model, as discussed before, if the damage is near the p-th sensor, S_p decreases, and as a result, R_{pj} decreases and R_{ip} increases. In the case that the sensor is located on the damage, the opposite effects can be seen. Specifically, S_p will be increased and R_{pj} will increase while R_{ip} decreases. In both cases, elements of R_{pj} and R_{ip} show opposite trends. Therefore, the combine-sum-residual, which is obtained by subtracting column_sum_rsd from row_sum_rsd, is thought to be more sensitive to damage than any one alone. The simulation results use the three sum-residuals will be compared in section5.2.4.

5.3.3 Control Chart Construction

The sum-residual vectors obtained from the residual matrix simplification procedure were used to create one control chart for each sensor. From the two months of collected data, 13,508 right-lane semi trucks were detected, among them, 5,477 are identified as heavy trucks and 8,031 are light trucks. For each weight group, 1000 event data were used to train the one-to-one linear prediction model, and additional 2000 were used to set the upper control limit (UCL) and the lower control limit (LCL) for the resulting control charts. The remaining data sets were utilized as monitoring data for the undamaged structure. Data for the damaged structure were obtained by incorporating the FEA results into the monitoring data as previously described. During the monitoring procedure of the proposed damage detection approach, data sets were plotted onto the control charts established during the training procedure. Out of limits points in the control charts indicate the

structural damage. The probability of detection (POD), which is the ratio of number of detections over the total number of tests (Eq.5.5), can be determined from the control chart results. Obviously, a higher POD indicated higher damage sensitivity and shorter detection delay. So POD can be used as a measurement of the sensitivity of the damage detection method.

$$probability\ of\ \text{det}ection\ (POD) = \frac{Number\ of\ \text{det}ections}{Total\ number\ of\ tests} \qquad \text{Eq.5.8}$$

When a statistical control chart is used, the POD can always be improved by lowering the UCL or increasing the LCL at the cost of a higher false alarm rate. For example, as shown in Fig. 5.18a&b, the histogram and cumulative distribution function (CDF) of the row-sum-residual for sensor S-SG-CB(1)-V are plotted before and after the occurrence of Level3 damage. In the figure, control limits ((UCL, LCL) and (UCL1, LCL1)) are calculated as following:

$$UCL, LCL = mean(no\_crack) \pm 3std(no\_crack) = \pm 1.02 .$$

$$UCL1, LCL1 = mean(no\_crack) \pm 2std(no\_crack) = \pm 0.68$$

When UCL and LCL are used, the POD is determined to be 19.03% with the false alarm rate of 0.3%. When the control limits are changed to UCL1 and LCL1, correspondingly, POD is changed to POD1 which equals to 55.47% with the false alarm rate of 2.3%. Changing the control limits increased the POD dramatically and it also increased the false alarm rate.

There is always a tradeoff between POD and false alarm rate. Therefore, determining a tolerable false alarm rate for a SHM system is important, and it in turn, determines the UCL and LCL of the control charts. In this work, the predefined target false alarm rate was selected to be around 0.3%. For normally distributed data, the corresponding UCL and LCL can be simply calculated as the mean plus or minus three times standard deviation. Study of the row-sum-residual, column-sum-residual, and combine-sum-residual indicated that their distributions are roughly normal no matter the range models or the extreme strain models are used. Some examples of the distributions are shown in Fig. 5.19 to Fig. 5.21, in which, the blue bars are the histograms of the training data, and the red lines show the fitted normal distributions. Figure 5.19 shows the distribution of the row- sum-residual for sensor C-SG-CB(1)-V and B-SG-BF-H obtained from

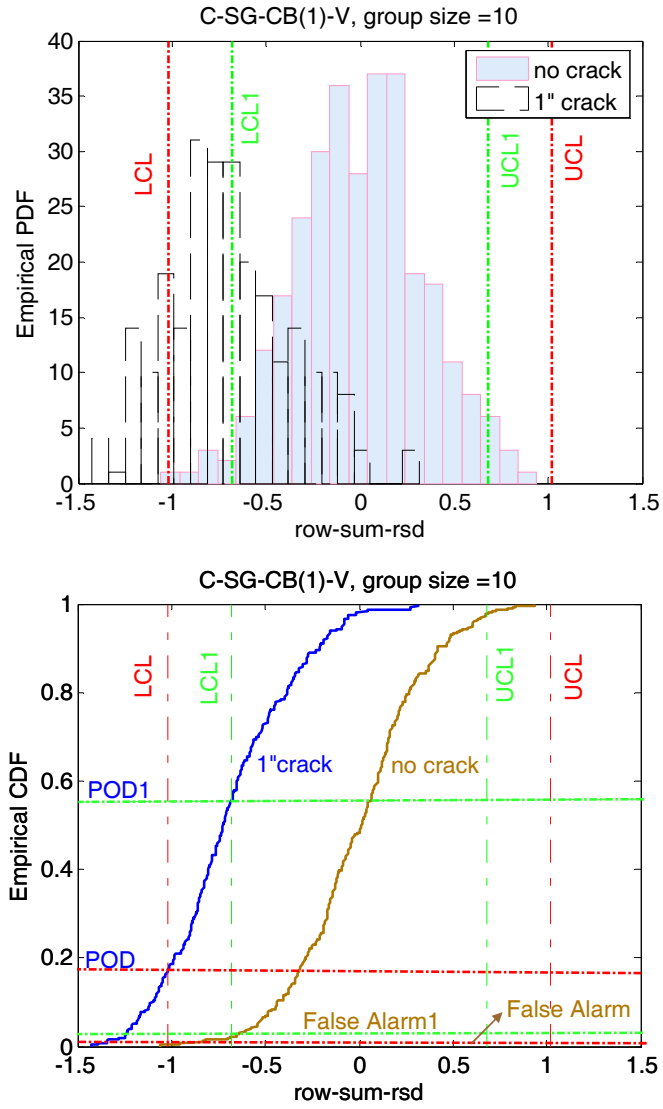

Figure 5.18 The relationship between the control limits and PODs and false alarm rates

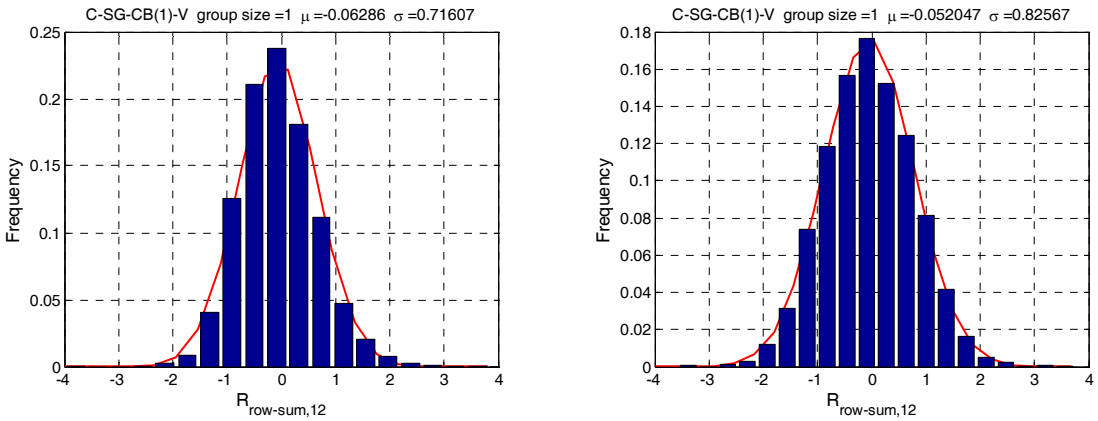

a. range model

b. max-max model

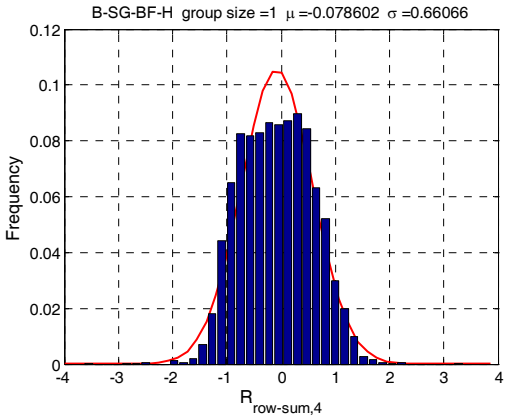

c. range model

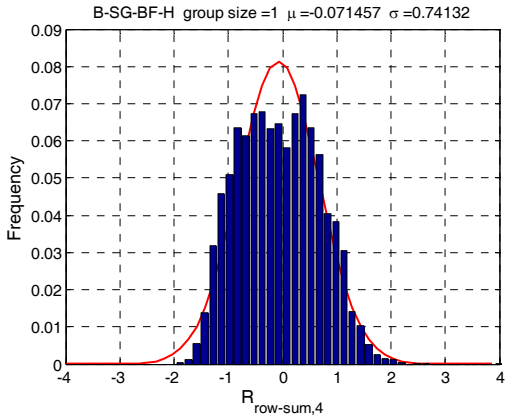

d. max-max model

Figure 5. 19 Distribution of the row-sum-residual

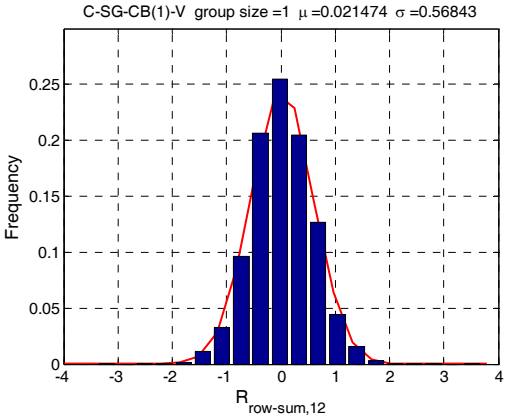

a. Sensor S-SG-CB(1)-V

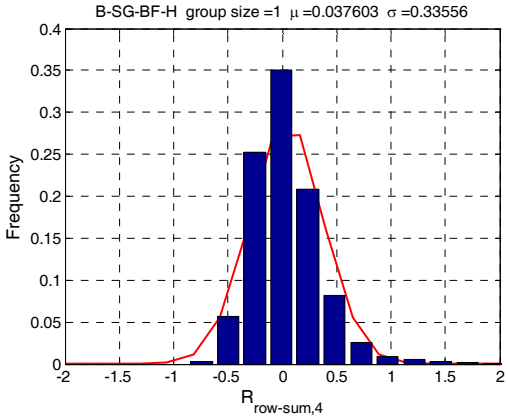

b. Sensor B-SG-BF-H

Figure 5.20 Distribution of the column-sum-residual, range model

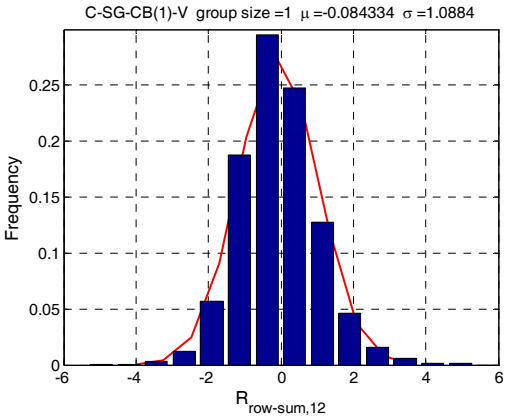

a. Sensor S-SG-CB(1)-V

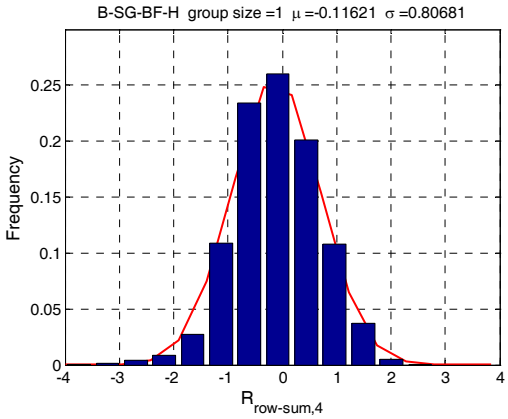

b. Sensor B-SG-BF-H

Figure 5.21 Distribution of the Combine-sum-residual

the range model and max-max model. The distributions of the column-sum-residual and combine-sum-residual for these two sensors calculated from the range model are shown in Figs. 5.20 and 5.21, respectively. Based on the selected false alarm rate and the observed normal distribution pattern, UCL and LCL for the control chart associated with the i-th sensor are determined to be:

$$\begin{cases} UCL_i = \mu_i + 3\sigma_i \\ LCL_i = \mu_i - 3\sigma_i \end{cases}$$

in which, μ_i is the mean of the i-th element in the simplified residual matrix, and

σ_i is the corresponding standard deviation.

Group size is another important parameter for $\bar{X}$ control chart analysis. When group size is larger than one, the mean of the data within one group is used as the chart variable and create one point in the resulting chart. The selection of group size directly affects the control limits and thus affects the sensitivity of the control chart. The relation between group size, control limits and the performance of resulting control chart will be discussed in details later in Section 5.6.

Using the group size of ten, examples of the constructed control charts are shown in Fig. 5.22. An observation period in Fig. 5.22 is equivalent to one truck group (i.e. ten trucks in this case). Such control charts were created for all sensors during the training procedure, and they define the baseline performance of the structure system. It should be pointed out that the data don't have to be normally distributed to use the control chart based damage detection approach. For non-normal data, the probability limits can be used as control limits. For example, if the false alarm rate is selected to be 0.3%, the control limits can be determined as the upper and lower 99.85% probability limits.

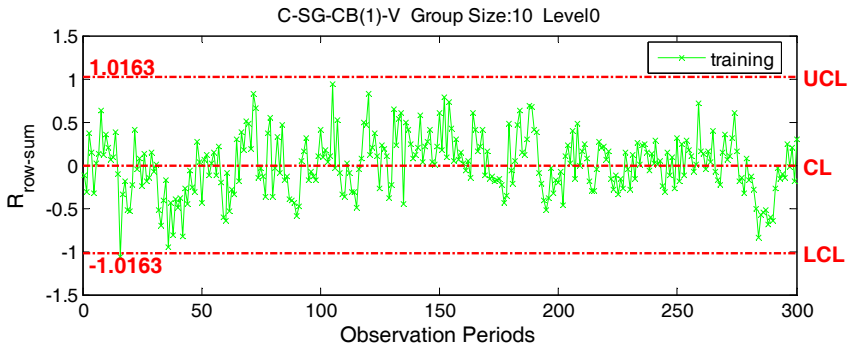

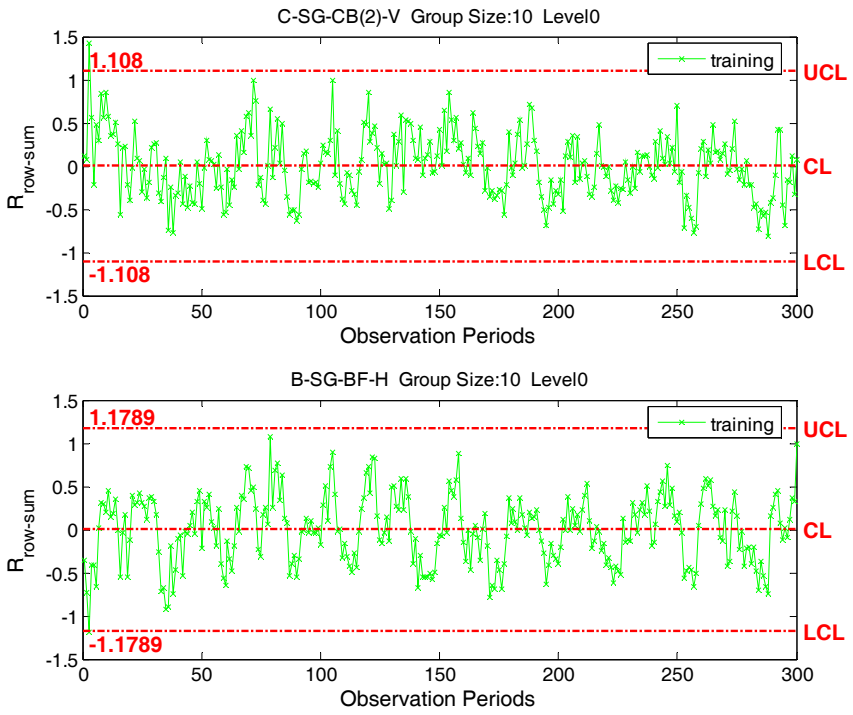

Figure 5. 22 Examples of the control chart constructed with training data

5.3.4 Results and Discussions

To evaluate the performance of the models and the residual matrix simplification methods proposed above, the monitoring stage control charts were studied using both the field collected data and simulated data. The damage detection results for the fatigue crack located between sensor C-SG-CB(1)-V and C-SG-CB(2)-V with different sizes are summarized and discussed in the following sections.

5.3.4.1 Comparison of Range Model and Extreme Strain Models

Among the residual simplifications approaches, only the row summation is applicable to both the range strain models and the extreme strain models. Therefore, it is employed in the performance comparison for these models. Examples of the monitoring stage control charts are shown in Fig. 5.23. In this figure, control charts of sensor C-SG-CB(1)-V obtained from different prediction models (e.g. range model, max-max model, min-min model, max-min, min-max model) were presented for the Level3 damaged structure. Red circles highlight damage alarms. Obviously, Fig. 5.23a presents a much better damage detection result than the others. Tables 5.5 and 5.6 summarize the POD obtained from all the models for all damage levels. The POD for the undamaged (Level0) structure is

the false alarm rates. From the tables, it can be seen that with comparable false alarm rate, the range-model can achieve much higher POD than any other model at most damage levels.

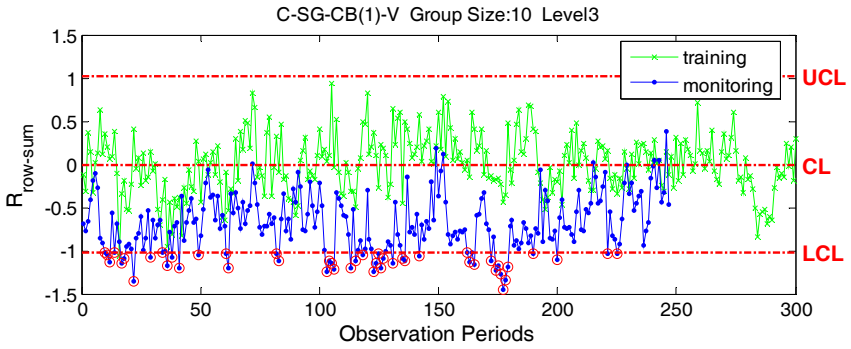

a. Range model

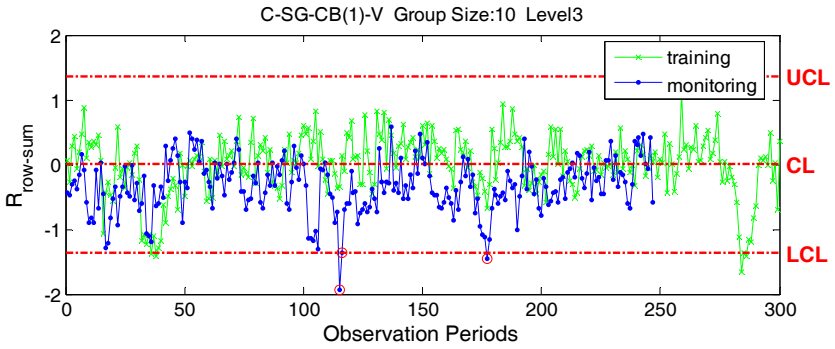

b. Max-max model

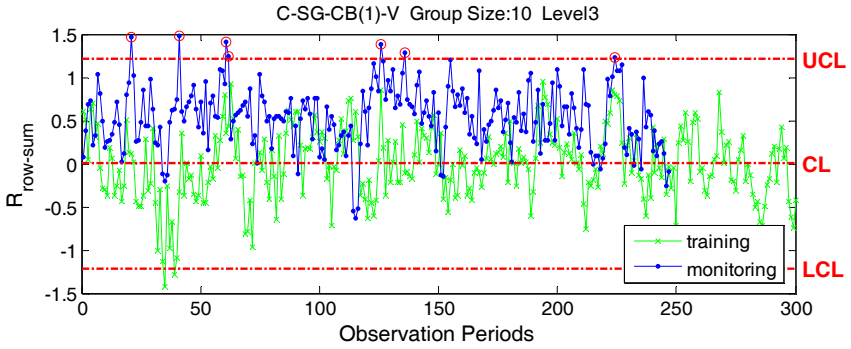

c. Min-min model

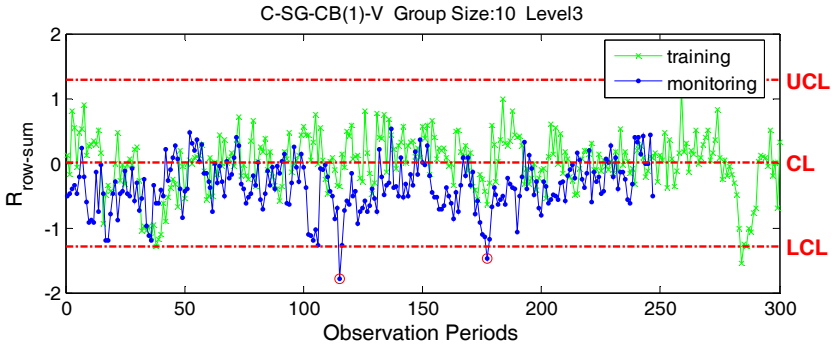

d. Max-min model

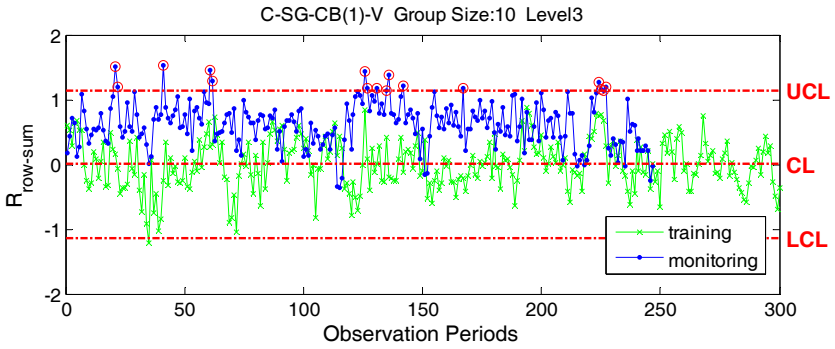

e. Min-max model

Figure 5.23 Control charts obtained from different one-to-one prediction models

Table 5.5 POD for sensor C-SG-CB(1)-V with different models

Damage Level	Models				
	Range	Max-Max	Min-Min	Max-Min	Min-Max
Level 0 (false alarm)	0.00%	0.41%	0.00%	0.41%	0.00%
Level 1	0.41%	0.41%	0.00%	0.81%	0.81%
Level 2	2.02%	1.22%	0.81%	0.81%	1.62%
Level 3	19.03%	1.22%	2.83%	0.81%	6.48%
Level 4	68.42%	6.88%	11.34%	8.50%	23.89%
Level 5	96.76%	6.07%	53.85%	7.69%	81.78%

Table 5.6 POD for sensor C-SG-CB(2)-V with different models

Damage Level	Models				
	Range	Max-Max	Min-Min	Max-Min	Min-Max
Level 0 (false alarm)	0.41%	0.81%	0.00%	0.81%	0.00%
Level 1	0.81%	0.81%	0.00%	0.81%	0.00%
Level 2	6.48%	0.81%	0.41%	0.81%	1.22%
Level 3	37.25%	2.02%	4.45%	2.02%	5.26%
Level 4	78.54%	1.22%	34.41%	1.22%	51.82%
Level 5	99.60%	8.91%	76.11%	12.15%	91.50%

5.3.4.2 Comparison of the Residual Matrix Simplification Methods

For the strain range-model three residual simplification methods were proposed. Here, the performances of the methods are compared in terms of the damage detection capability. Figures 5.24 and 5.25 show the monitoring stage control charts for the Level3 damaged structure obtained from the row summation, column summation, and combined summation algorithms for sensor C-SG-CB(1)-V and C-SG-CB(2)-V. It can be seen that both row summation and combined summation can achieve better damage detection results than column summation. However, no significant difference can be seen for row summation and combined summation methods. Further study of the PODs summarized in Tables 5.7 and 5.8 indicated that the PODs obtained from the two methods are comparable at all damage levels for sensor C-SG-CB(1)-V; for sensor C-SG-CB(2)-V, the combined summation approach leads to a higher POD and slightly lower false alarm rate. Therefore, the combined summation method is recommended and will be used as the residual matrix simplification method.

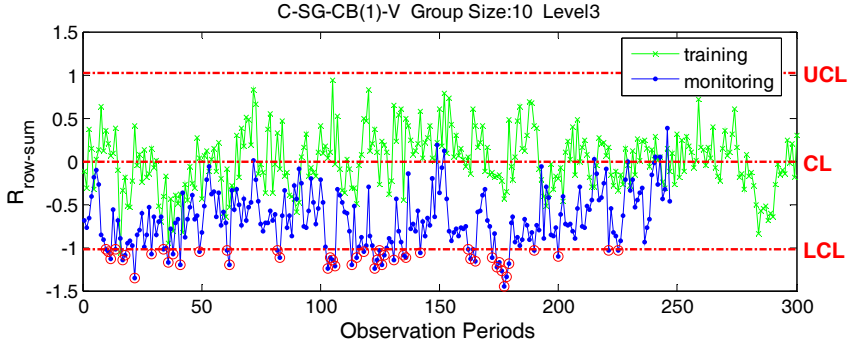

a. row summation

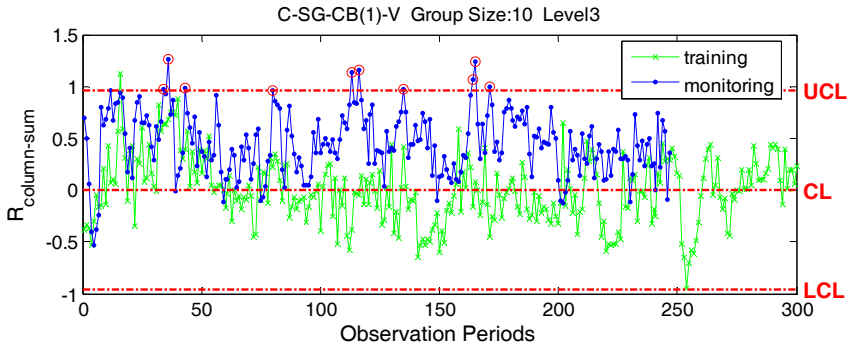

b. column summation

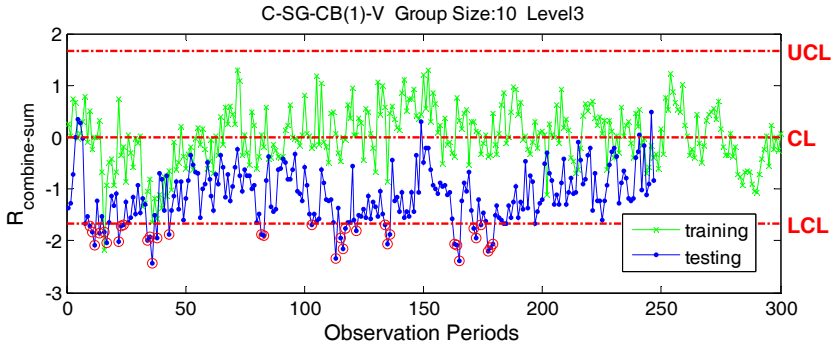

c. combined summation

Figure 5.24 Control charts obtained from different residual matrix simplification algorithms

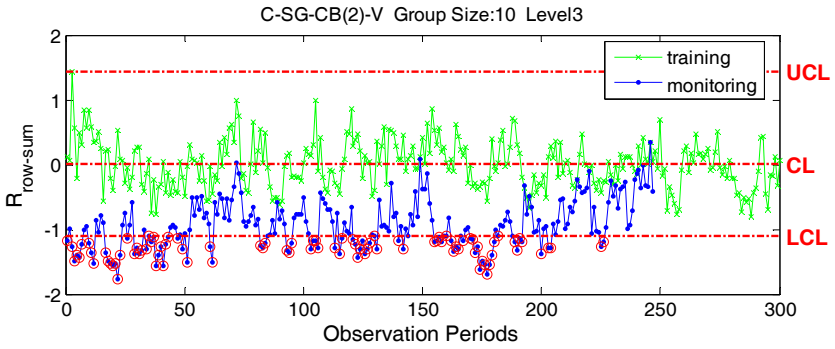

a. row summation

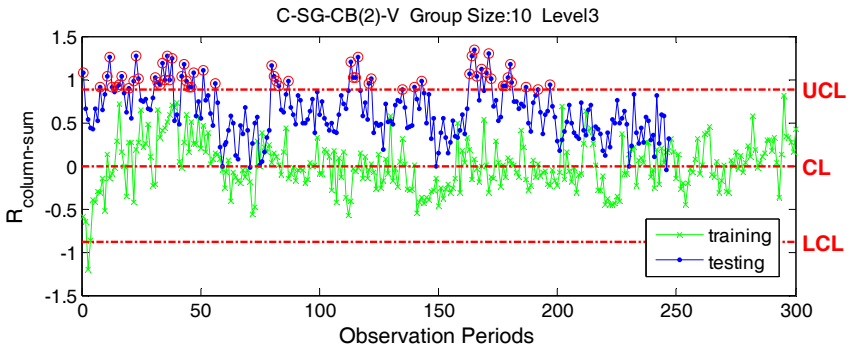

b. column summation

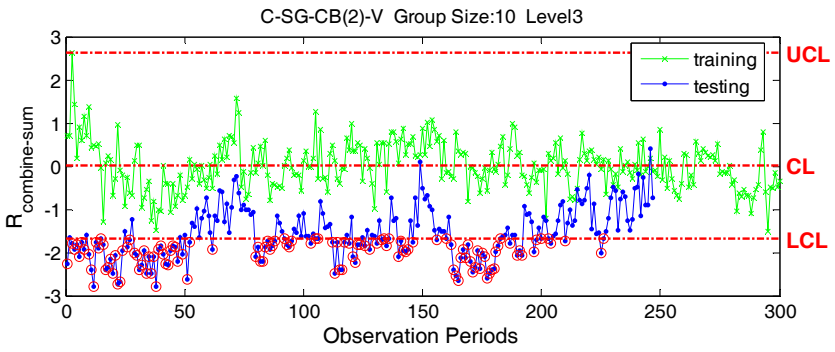

c. combined summation

Figure 5.25 Control charts obtained from different residual matrix simplification algorithms

Table 5.7 POD for sensor C-SG-CB(1)-V with different residual matrix simplification algorithms

Damage Level	Simplification algorithms		
	Row-sum	Column-sum	Combine-sum
Level 0 (false alarm)	0.00%	0.00%	0.00%
Level 1	0.41%	0.00%	0.00%
Level 2	2.02%	1.22%	2.43%
Level 3	19.03%	4.05%	13.77%
Level 4	68.42%	31.17%	68.02%
Level 5	96.76%	70.45%	97.17%

Table 5.8 POD for sensor C-SG-CB(2)-V with different residual matrix simplification algorithms

Damage Level	Simplification algorithms		
	Row-sum	Column-sum	Combine-sum
Level 0 (false alarm)	0.41%	0.00%	0.00%
Level 1	0.81%	0.00%	1.62%
Level 2	6.48%	4.05%	9.72%
Level 3	37.25%	23.48%	49.80%
Level 4	78.54%	56.68%	87.05%
Level 5	99.60%	97.98%	100.00%

5.3.4.3 Comparison of Different Truck Weight Groups

With the range model and the combined summation simplification approach, the control charts obtained from different truck groups (e.g. heavy trucks, light trucks and all trucks), are compared. Examples of the result control charts for sensor C-SG-CB(2)-V are shown in Fig. 5.26. As can be seen, for Level3 damage, using heavy truck data (Fig. 5. 24a) resulted in a higher alarm rate than using the other two truck groups. To make the comparison more precise and more complete, the PODs for all

damage levels and for both sensor C-SG-CB(1)-V and C-SG-CB(2)-V are summarized in Tables 5.9 and 5.10. It is no surprise that, with a comparable false alarm rate heavy trucks consistently show the highest damage detection rate. Further comparison indicates that using all trucks as one group can achieve a higher POD than using light trucks only. This is because the damage induced strain changes are relatively small for light trucks. Although the prediction models defined by light trucks are more specific than those defined by all trucks (as shown in Fig. 5.17), the effect is cancelled by the small damage induced strain changes.

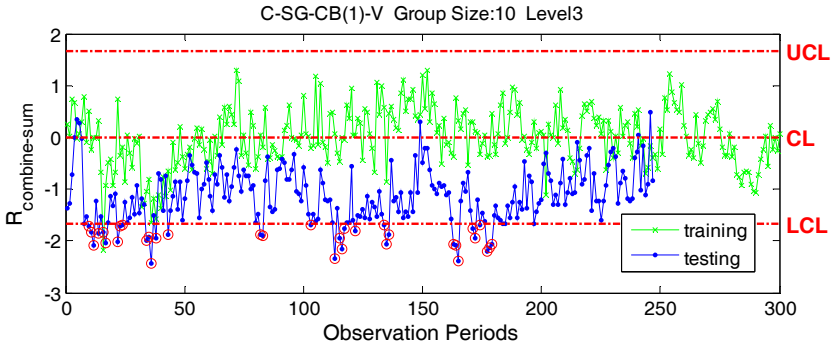

a. heavy trucks

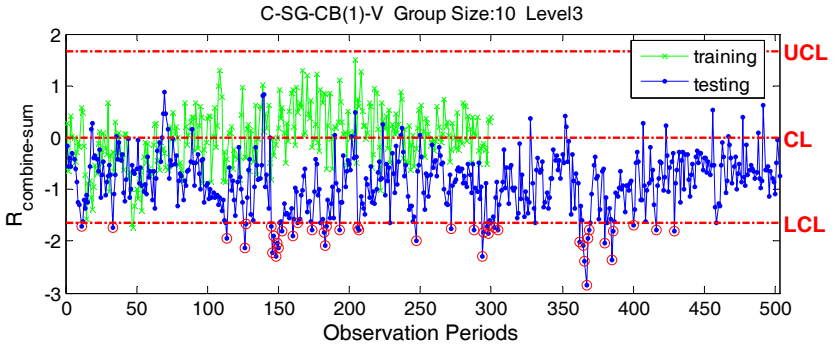

b. light trucks

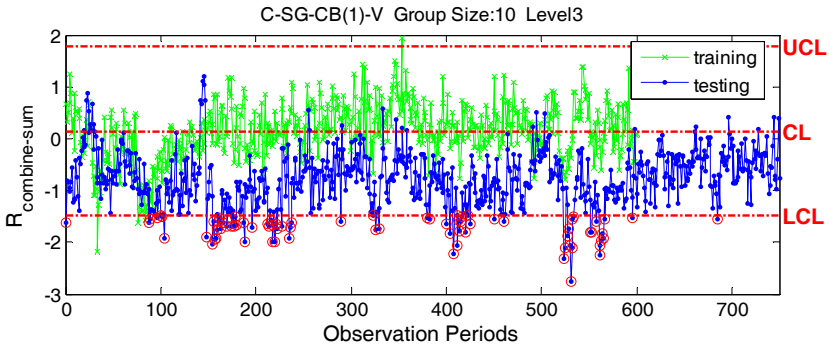

d. all trucks

Figure 5.26 Control charts obtained from different truck groups

Table 5.9 POD for sensor C-SG-CB(1)-V with different truck groups

	Truck groups		
Damage Level	heavy	light	all
Level 0 (false alarm)	0.00%	0.40%	0.40%
Level 1	0.00%	0.99%	0.67%
Level 2	2.43%	2.58%	3.07%
Level 3	13.77%	8.35%	10.40%
Level 4	68.02%	34.20%	45.20%
Level 5	97.17%	83.10%	87.33%

Table 5.10 POD for sensor C-SG-CB(2)-V with different truck groups

	Trucks used		
Damage Level	heavy	light	all
Level 0 (false alarm)	0.00%	0.40%	0.67%
Level 1	1.62%	1.19%	1.20%
Level 2	9.72%	3.98%	6.13%
Level 3	49.80%	23.46%	30.27%
Level 4	87.05%	61.63%	71.47%
Level 5	100.00%	98.01%	99.20%

5.3.4.4 Comparison of Using Residual and Using Strain Directly

It has been qualitatively analyzed that the residual is more sensitive to structural damage than the strain due to the reduction of truck weight variances caused strain deviations. To further verify this, the control charts analysis results of the two methods are compared using heavy truck data. The strain range model along with the combined summation residual matrix simplification procedure was employed to construct the residual based control chart. At the same time, the strain data sets were charted directly to create the strain based control chart. Examples of the two types of control charts are shown in Fig. 5.27. From the figure, it can be seen that the residual based control charts resulted in a higher probability of detection. The results summarized in Table5.11 further indicate that using the residual instead of strain itself can increase the damage sensitivity without introducing additional false alarms.

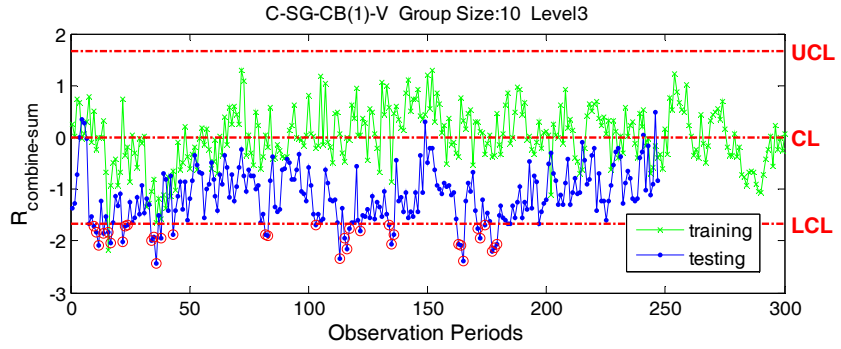

a. Combine-sum-residual

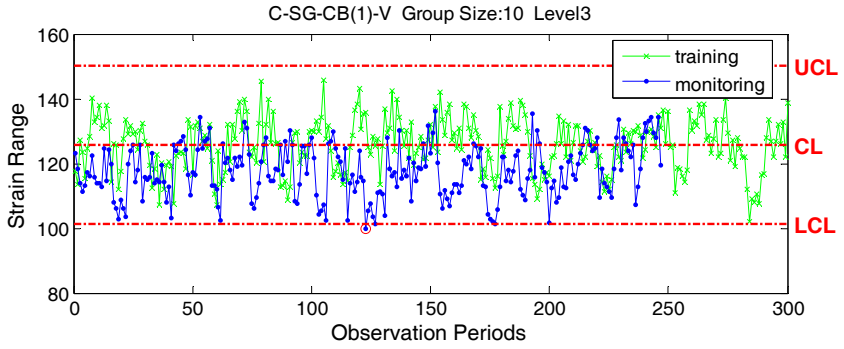

b. Event strain range

Figure 5.27 Control charts obtained from simplified residual data and event strain range

Table 5.11 POD for sensor C-SG-CB(1)-V and C-SG-CB(2)-V

	Combine_sum_residual		Strain directly	
Damage Level	C-SG-CB(2)-V	C-SG-CB(1)-V	C-SG-CB(2)-V	C-SG-CB(1)-V
Level 0 (false alarm)	0.41%	0.00%	0.00%	0.00%
Level 1	0.81%	0.41%	0.00%	0.00%
Level 2	6.48%	2.02%	0.00%	0.00%
Level 3	37.25%	19.03%	4.05%	0.41%
Level 4	78.54%	68.42%	11.34%	6.48%
Level 5	99.60%	96.76%	31.17%	17.41%

5.3.4.5 Summary

The results discussed above indicate that for the situations analyzed:

1) The strain range model is better than the extreme strain models;
2) The combination summation is an effective residual matrix simplification method;
3) Use of the simplified residual as the damage indictor can lead to higher damage sensitivity than the use of strain directly;
4) Use of the heavy truck group can improve damage sensitivity.

5.4 Method Two (one-to-one model, two-level evaluation method)

The first two steps of this method are the same as the one-to-one model direct evaluation approach discussed in Section5.3. As the strain range models have been shown to be more damage sensitive, they are selected for use in this approach as well. After the one-to-one models are constructed, a 40×40 residual matrix can be calculated for each truck event. With this method, a first level control chart is constructed for each element of the residual matrix. Therefore, 1600 first level control charts can be created. The control charts evaluation results are then used to generate the evaluation matrix by replacing the elements in the residual matrix with:

1) '0', if the element is within limits
2) '1', the element is larger than UCL;
3) '-1', the element is smaller than LCL;

After obtaining the evaluation matrix, it was simplified into a forty degree vector; so that a second level control chart can be created for each sensor. The elements of the simplified evaluation matrix are not normally distributed, so the data rank 0.15% from the top and the bottom of the sorted training data are used as the control limits.

The three simplification approaches, the row summation, column summation, and the combination summation, are compared in Section 5.4.1. The two-level evaluation approach is conceptually close to the approach proposed in the previous research. In Section5.4.2, previously developed method was re-implemented in the residual based control chart format, and only select truck loads were used. The re-implementation is an improved version of the original method, and it is compared with the two-level evaluation approach. Finally, in Section5.4.3, the two level evaluation method is compared with the one-to-one model direct evaluation method.

5.4.1 Comparison of the Evaluation Matrix Simplification Approaches

The residual matrix simplification procedures used in the direct evaluation method can also be applied for the evaluation matrix simplification. As the elements in the evaluation matrix have three values (e.g. +1, 0, or -1) only, they can be summed up without standardization. When damage occurs near to p-th sensor, the p-th row summation decreases because the "-1" evaluations increase. On the other hand, the column summation increases due to the increase of "+1" evaluations. The change tendencies can also be seen from Fig. 5.28, which shows examples of the control charts constructed with different evaluation matrix simplification methods. Since the column summation

was affected by the coefficients of $a_{1,ip}$ in the prediction model, when the absolute value of the $a_{1,ip}$ is small, the damage effect was reduced, and as a result the column summation is not as damage sensitive as the row summation method. This is consistent with the conclusion obtained from the residual matrix simplification approaches used in the direct evaluation method. As for the combined summation approach, with the two-level evaluation approach, its performance is not as good as the row summation approach. This might be due to the fact that the combined summation which contains more uncertainties than the row summation method alone. When the effect of the additional uncertainties overtakes the benefit of combining column summation and row summation together, the damage sensitivity is reduced. The examples shown in Fig. 5.28 and the POD results listed in Table 5.12 and 5.13 all indicate that row summation can achieve the best damage detection results for the two-level evaluation approach.

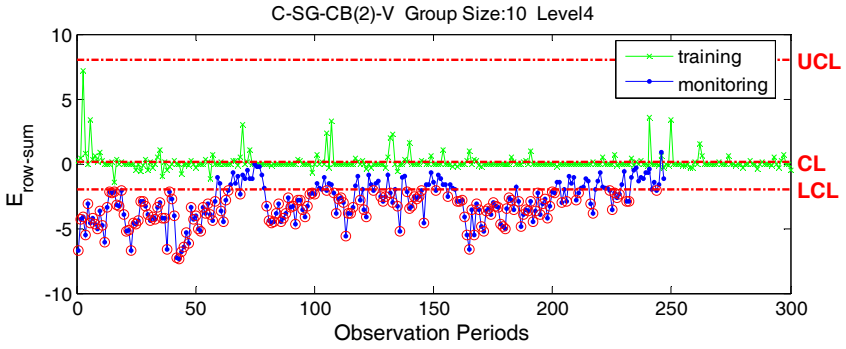

a. Row summation

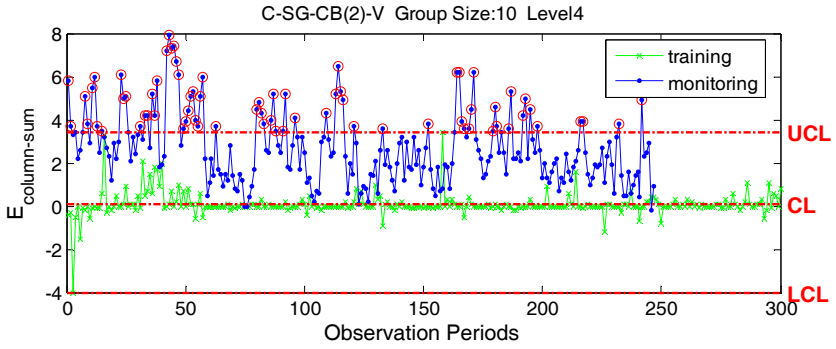

b. Column summation

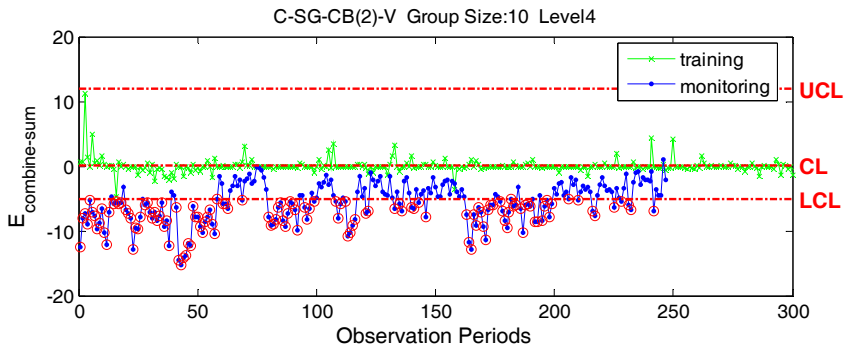

c. Combined summation

Figure 5.28 Control charts obtained from different evaluation matrix simplification algorithms

Table 5.12 POD for sensor C-SG-CB(1)-V with different evaluation matrix simplification methods

Damage Level	Row-sum	Column-sum	Combine-sum
Level 0 (false alarm)	0.00%	0.00%	0.00%
Level 1	0.00%	0.00%	0.00%
Level 2	0.00%	0.00%	0.00%
Level 3	0.81%	0.41%	0.41%
Level 4	21.86%	9.72%	15.39%
Level 5	85.83%	55.87%	74.49%

Table 5.13 POD for sensor C-SG-CB(2)-V with different evaluation matrix simplification methods

Damage Level	Row-sum	Column-sum	Combine-sum
Level 0 (false alarm)	0.41%	0.00%	0.41%
Level 1	0.41%	0.41%	0.41%
Level 2	1.22%	0.81%	0.81%
Level 3	16.60%	4.45%	8.91%
Level 4	68.83%	28.75%	53.44%
Level 5	100.00%	93.93%	100.00%

5.4.2 Comparison of the Two-Level Evaluation Method and the Improved Previous Method

The row summation based two-level evaluation method is conceptually close to the damage detection which was originally proposed in the previous research (Doornink, 2006). For easy comparison, the previously developed method was re-implemented in the control chart format. During the re-implementation, the following improvements were made:

1) Instead of using all types of trucks during the damage evaluation, the improved method only uses right-lane, five-axle, heavy, semis.

2) Using the residual as damage indicator enabled the mathematical control limits selection procedure, which is more reliable than defining control limits manually.
3) The in-direct matches used in the previous method were removed by the perfectly defined event based extreme strains.
4) The strain range is more damage sensitive than the extreme strains used in previous method.

Although significantly improved, the previous method still shows a lower POD than the two-level evaluation approach. Table 5.14 and the examples of the control charts shown in Fig. 5.29 all indicate as much. With the two-level evaluation approach the first level fail evaluations were differentiated into "1" (larger than UCL) and "-1" (smaller than LCL), however, in the improved previous approach, all the fail evaluations were taken as "1". So essentially, the POD improvement is resulted from the different evaluation matrix creation rule.

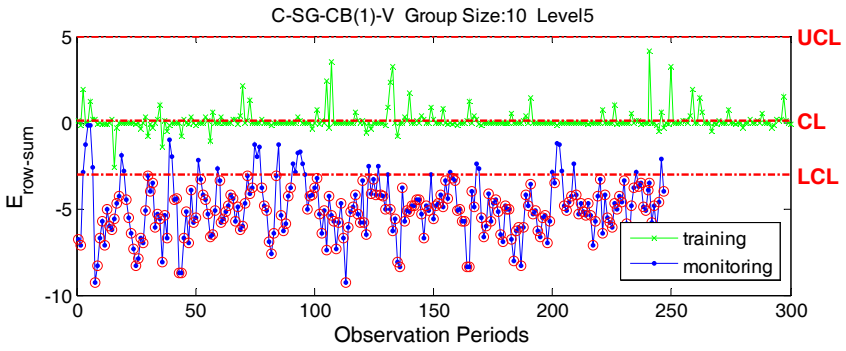

a. Two-level evaluation method

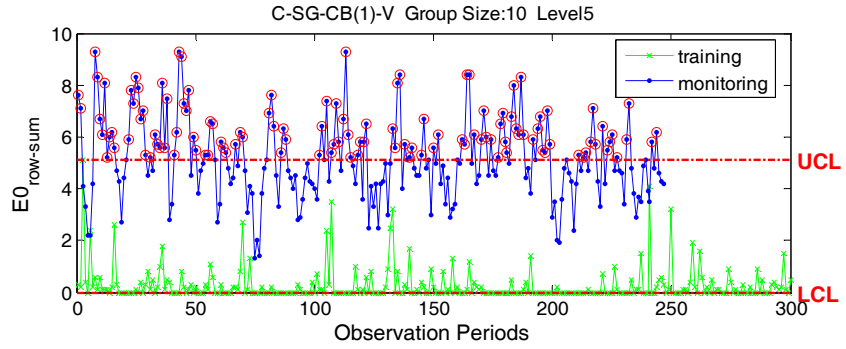

b. Improved previous method

Figure 5.29 Control charts obtained from different evaluation matrixes

Table 5.14 POD for sensor C-SG-CB(1)-V and C-SG-CB(2)-V

Damage Level	Improved previous method		Two-level evaluation method	
	C-SG-CB(2)-V	C-SG-CB(1)-V	C-SG-CB(2)-V	C-SG-CB(1)-V
Level 0 (false alarm)	0.00%	0.00%	0.41%	0.00%
Level 1	0.00%	0.00%	0.41%	0.00%
Level 2	0.00%	0.00%	1.22%	0.00%
Level 3	0.00%	0.00%	16.60%	0.81%
Level 4	0.00%	2.02%	68.83%	21.86%
Level 5	54.25%	48.18%	100.00%	85.83%

5.4.3 Comparison of the Two-Level Evaluation Method and the Direct Evaluation Method

The discussion presented in Section 5.3 and Section 5.4.1 indicate that the combined summation and row summation achieve the best damage detection results for the direct evaluation method and the two-level evaluation method, respectively. The PODs for these two approaches are compared in Table 5.15. It can be seen that for Level5 damage, both methods can achieve a 100% detection rate. For relatively small damages, such as Level3 damage, the POD associated with the direct evaluation method is 49.8% for C-SG-CB(2)-V. For the two-level evaluation method, however, it is only 16.6%. Apparently, using the evaluation matrix in the two-level evaluation method can cause information loss which in turn results in its insensitivity to small damages. With the direct evaluation method, the small changes in the residual matrix can be summed up into a damage signal. However, when they are replaced by first level control chart evaluation results, these small changes can be masked and be replaced with “0”; and, as such, no signal will be created. In conclusion, compared to the one-to-one model direct evaluation method, the two-level evaluation method is not as sensitive to small damage.

Table 5.15 POD for sensor C-SG-CB(1)-V and C-SG-CB(2)-V with different damage detection methods

Damage Level	Direct evaluation method (combine_sum)		Two-level evaluation method (row_sum)	
	C-SG-CB(2)-V	C-SG-CB(1)-V	C-SG-CB(2)-V	C-SG-CB(1)-V
Level 0 (false alarm)	0.00%	0.00%	0.41%	0.00%
Level 1	1.62%	0.00%	0.41%	0.00%
Level 2	9.72%	2.43%	1.22%	0.00%
Level 3	49.80%	13.77%	16.60%	0.81%
Level 4	87.05%	68.02%	68.83%	21.86%
Level 5	100.00%	97.17%	100.00%	85.83%

5.5 Method Three (many-to-one model method)

As discussed above, the methods which use the one-to-one models always result in a complicated residual matrix which needs significant effort to handle. In this section, a different prediction model, named the many-to-one model, is discussed. With the new model, the dimension of the obtained residual matrix always equals the number of sensors. Many-to-one models, as implied by the name, use data of all other sensors to predict the performance of the remaining one sensor (Eq.5.9). As strain ranges have been shown to be the most damage sensitive performance measurement, they are utilized here to construct the many-to-one models. In the same way as the construction of the one-to-one model, 1000 training data sets were employed to calculate model coefficients (a_{ij} in Eq.5.9) with the standard least squares linear regression approach. After the models were obtained for all sensors, the residual matrix can be calculated as Eq.5.10. As the dimension of the residual matrix equals the number of sensors, one control chart can be created for each sensor directly. Observations show that the distribution of each element in the residual matrix is near to normal (selected examples are shown in Fig. 5.30). And, as such, the UCL and LCL of the control charts are determined to be the mean plus/minus three times the standard deviation (Eq.5.11).

$$S_{pred,i} = f(S_1, S_2, ..S_j ...S_{40}) = a_{i0} + a_{i1}S_1 + a_{i2}S_2 + ... + a_{ij}S_j + ... + a_{i40}S_{40} \quad (a_{ij} = 0 \ when \ i = j) \qquad \text{Eq.5. 9}$$

$$\begin{bmatrix} R_1 \\ : \\ R_i \\ : \\ R_{40} \end{bmatrix} = \begin{bmatrix} S_1 \\ : \\ S_i \\ : \\ S_{40} \end{bmatrix} - \left(\begin{bmatrix} a_{10} \\ : \\ a_{i0} \\ : \\ a_{400} \end{bmatrix} + \begin{bmatrix} 0 & .. & a_{1j} & .. & a_{140} \\ : & 0 & : & : & : \\ a_{i1} & .. & a_{ij} & .. & a_{i40} \\ : & : & : & 0 & : \\ a_{401} & .. & a_{40j} & .. & 0 \end{bmatrix} \begin{bmatrix} S_1 \\ : \\ S_i \\ : \\ S_{40} \end{bmatrix} \right) \qquad \text{Eq.5.10}$$

In which, R_i is the residual associated with the i-th sensor

S_i is the strain range for the i-th sensor

a_{ij} are coefficients.

$$\begin{cases} UCL_i = \mu_i + 3\sigma_i \\ LCL_i = \mu_i - 3\sigma_i \end{cases} \qquad \textbf{Eq.5. 11}$$

in which, μ_i is the mean of R_i calculated from training data, and

σ_i is the standard deviation of R_i calculated from training data.

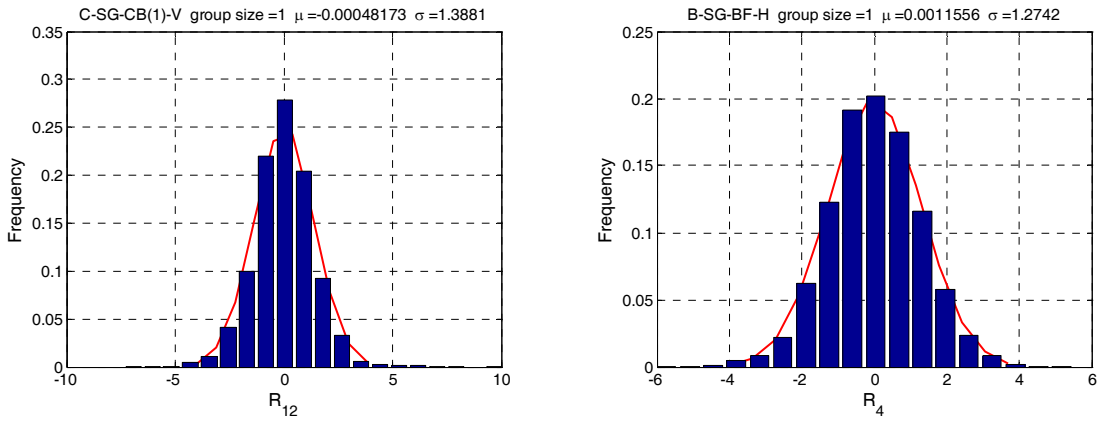

Figure 5.30 Examples of distribution of residuals obtained from many-to-one model

Using the same testing data, the POD results obtained from the many-to-one model method are compared with those obtained from the one-to-one model direct evaluation method. As can be seen from Table 5.16, the PODs associated with C-SG-CB(2)-V are comparable for the two methods; while the direct evaluation method shows a slightly higher damage detection rate for C-SG-CB(1)-V. Obviously only comparing the PODs for sensor C-SG-CB(2)-V and C-SG-CB(1)-V can hardly determine which method is better. Keep in mind that the control chart results should indicate not only the damage occurrence but the damage locations. Therefore, the crack located in the middle of sensor C-SG-CB(2)-V and C-SG-CB(1)-V should not cause the damage alarms for other sensors. With the one-to-one model direct evaluation method this is generally true due to the standardization procedure. Recall that in the one-to-one model direct evaluation method, elements in the residual matrix are standardized before being summed up. So in the summation results, the contribution of each single element is roughly equal. As a result, the row/column summation changes significantly when all or most elements in a row/column of the residual matrix show some changes; otherwise, if only few elements are changed, the change will not result in a damage alarm. However, with the many-to-one model approach, there is no chance to perform such standardization. The damage induced strain change for one sensor can be enlarged by the coefficients of the prediction model and result in alarms for sensors which are not near to the damage location. Examples of the control charts which create considerable alarms due to a non-vicinity damage are presented in Fig. 5.31a. As a comparison, the corresponding control charts obtained from the direct evaluation method are shown in Fig. 5.31 b. The comparison indicates that the many-to-one model method is not as effective as the direct evaluation method in terms of the damage location detection.

Table 5.16 POD for sensor C-SG-CB(1)-V and C-SG-CB(2)-V

Damage Level	One-to-one model		Many-to-one model	
	C-SG-CB(2)-V	C-SG-CB(1)-V	C-SG-CB(2)-V	C-SG-CB(1)-V
Level 0 (false alarm)	0.00%	0.00%	0.81%	0.41%
Level 1	1.62%	0.00%	2.02%	0.41%
Level 2	9.72%	2.43%	4.45%	5.26%
Level 3	49.80%	13.77%	43.32%	6.48%
Level 4	87.05%	68.02%	92.31%	54.25%
Level 5	100.00%	97.17%	100.00%	70.85%

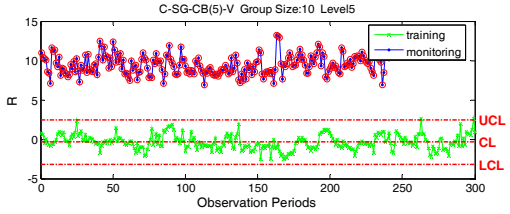

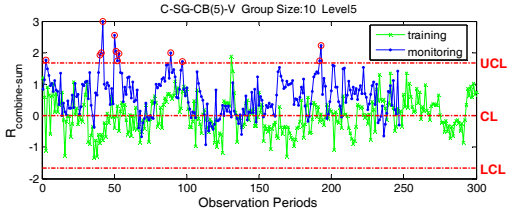

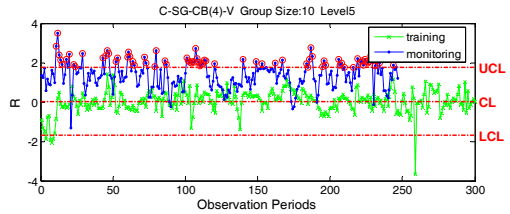

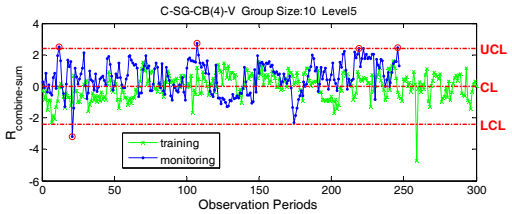

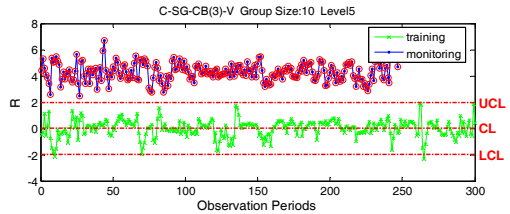

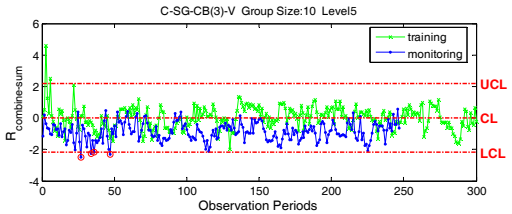

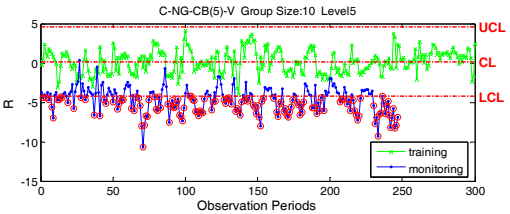

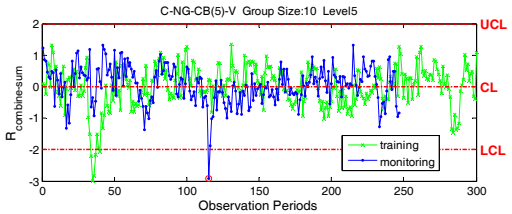

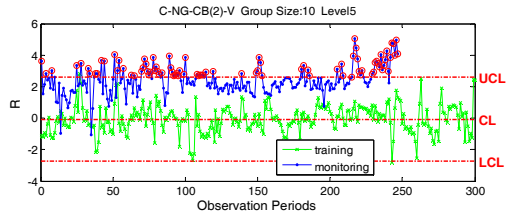

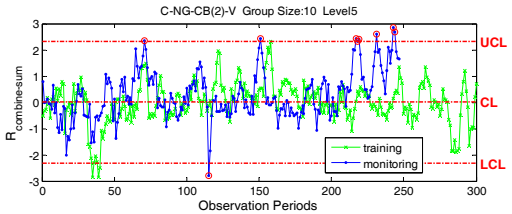

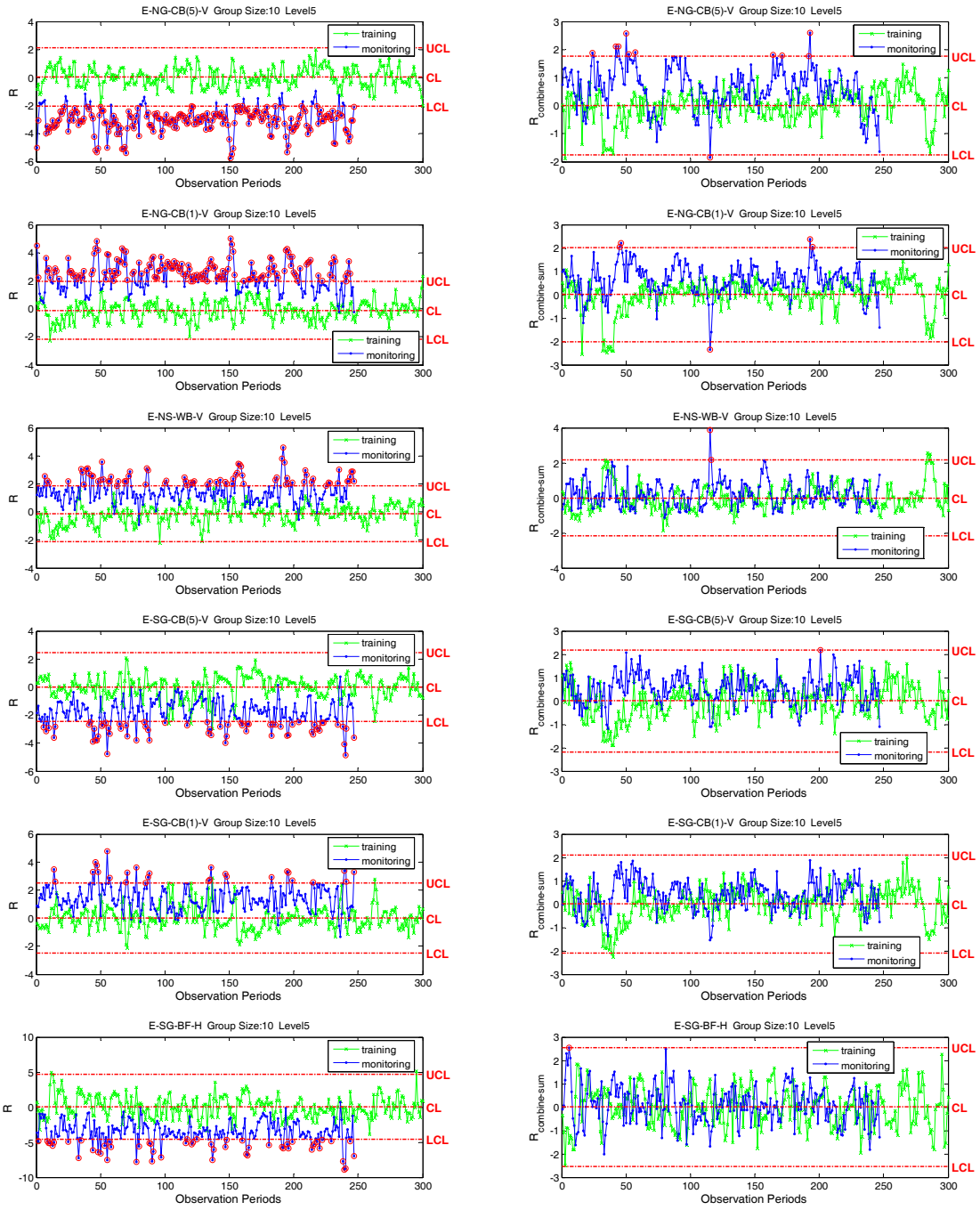

a. many-to-one model method b. direct evaluation method

Figure 5.31 Alarms caused by a non-vicinity damage

5.6 Further Discussions for the One-to-One Model Direct Evaluation Method

From the discussion above, it can be concluded that the one-to-one model direct evaluation method is the most damage sensitive and the most effective in damage location detection. In this section, studies were carried out to further evaluate the performance of this damage detection approach.

5.6.1 Detection Delay and Its Relationship with the Group Size

The control charts results and PODs obtained from the direct evaluation method were discussed in Section 5.2. With the POD known, the average damage Detection Rate (DR) after n-groups (n_{group}) of truck passed the bridge can be calculated. It is easier to calculate the probability that the damage can not be detected first, which is, as shown in Eq.5.12, $(1-POD)^{n_{group}}$. The corresponding damage Detection Rate (DR) is simply one minus the No-Detection Rate (NDR), see Eq.5.13. After selecting a reliable DR, the detection delay in terms of the number of truck groups (n_{group}) can be calculated as Eq.5.14. For an example, the POD is 92.31% for C-SG-CB(2)-V when Level3 damage occurs; the detection is considered to be reliable when DR is higher than or equal to 99%; by plugging these numbers into Eq.5.14 , the detection delay can be calculated as $n_{group} = \log_{(1-92.31\%)}(1-99\%) = 2$. The result indicates that with two groups of trucks passed the bridge, the probability that C-SG-CB(2)-V can detect the damage is higher than 99%.

$$No\text{-}Detection\ Rate\ (NDR) = (1\text{-}POD)^{n_{group}} \qquad \text{Eq.5. 12}$$

$$Detection\ Rate(DR) = 1\text{-}NDR = 1\text{-}(1\text{-}POD)^{n_{group}} \qquad \text{Eq.5. 13}$$

$$n_{group} = \log_{(1-POD)}(1-DR) \qquad \text{Eq.5. 14}$$

As can be seen from Eq.5.14, the detection delay (n_{group}) is directly related to POD, which, as discussed before, is an indication of the sensitivity of the control chart. The sensitivity of Shewhart control chart has long been known to be highly correlated with the group sizes (Grant 1996). Therefore, the group size is an important parameter for control chart based damage detection approaches. In general, the larger the group size, the narrower the control limits and the easier it is to detect small variations. As an example, Fig. 5.32 shows the distributions of the combine-sum-residual for C-SG-CB(1)-V with the group size of 10 and 1. Obviously, the group size 10 results in a less dispersed distribution and narrowed control limits (LCL10 and UCL10 in Fig. 5.32b) than the group size of one does. When control chart is applied in the industrial quality control the ideal group size was suggested to be four. For ease of calculation, in some industrial practices, a group size of five is widely used. However, when it is desired to make the control chart sensitive to small variations a larger group sizes such as 10 or 20 are suggested (Grant 1996). The group size was

selected to be 10 in the discussion in Section 5.2 to Section 5.4. The selection will be justified in the following.

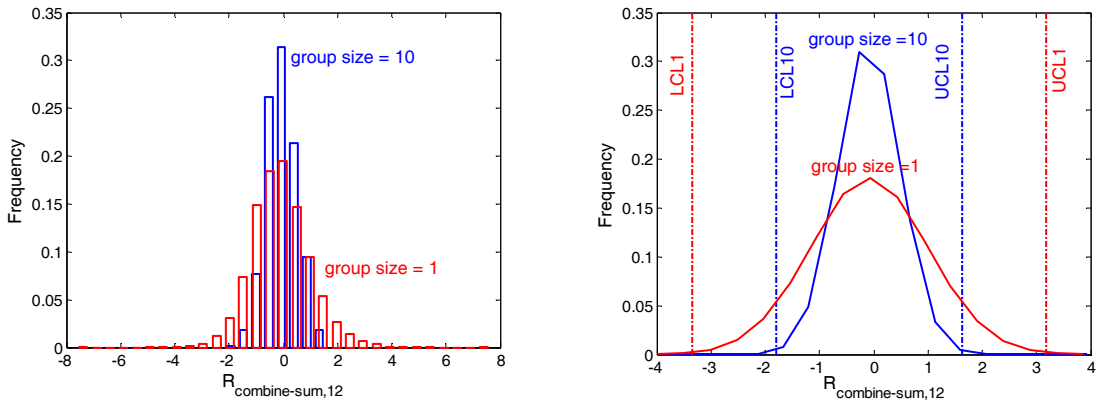

a. the comparison of the distributions b. the comparison of control limits

Figure 5.32 The combine-sum-residual distributions and control limits for sensor C-SG-CB(1)-V with different group sizes

For slight damages, larger group size can improve the POD dramatically, which in turn, leads to a smaller damage delay (n_{group}). On the other hand, for relatively large damage, the improvement is not significant. This can be seen from Tables 5.17 and 5.18, which summarize the PODs for C-SG-CB(1)-V and C-SG-CB(2)-V with different group sizes and different damage levels. For Level2 damage (slight damage), when the group size is reduced from 200 to 10, the POD for sensor C-SG-CB(2)-V decreased from 58.33% to 9.72%. On the other hand, for Level5 damage (relatively large damage), 100% POD can be achieved for both group size of 200 and a group size of 10. As another example, Fig. 5.33 shows the relationship between detection rate and the number of monitoring periods (one monitoring period is equivalent to one truck group) for sensor C-SG-CB(2)-V. Level3 damage (Fig. 5.33 a) is selected to represent slight damage, while Level5 damage (Fig. 5.33 b) represents relatively large damage. For slight damage (Fig. 5.33 a), to allow the detection rate to reach 99% the required number of monitoring periods is small when the group size is large. (i.e. 3 monitoring periods are required by a group size of 100, and 4 monitoring periods are required by a group size of 50). As the group size decreases, the required monitoring periods increase dramatically. It increases to 14 for a group size of 5, and more than 100 for a group size of 1. However, for Level5 damage (Fig. 5. b), when the group size is larger than one, the damage can always be detected with only one monitoring period.

Table 5.17 POD for C-SG-CB(2)-V with different group sizes and different damage levels

Group Size	Level0 (False Alarm)	Level1	Level2	Level3	Level4	Level5
1	0.08%	0.32%	0.93%	3.71%	14.82%	66.45%
5	0.20%	0.61%	3.84%	28.69%	76.57%	99.39%
10	0.00%	1.62%	9.72%	49.80%	87.05%	100.00%
20	0.00%	2.44%	16.26%	65.04%	95.12%	100.00%
30	0.00%	4.88%	23.17%	70.73%	100.00%	100.00%
40	0.00%	4.92%	26.23%	78.69%	100.00%	100.00%
50	0.00%	4.08%	26.53%	77.55%	100.00%	100.00%
60	0.00%	7.32%	26.83%	73.17%	100.00%	100.00%
70	0.00%	11.43%	34.29%	80.00%	100.00%	100.00%
80	3.33%	6.67%	40.00%	80.00%	100.00%	100.00%
90	0.00%	7.41%	37.04%	77.78%	100.00%	100.00%
100	4.17%	12.50%	37.50%	87.50%	100.00%	100.00%
125	0.00%	10.53%	36.84%	89.47%	100.00%	100.00%
150	0.00%	18.75%	31.25%	87.50%	100.00%	100.00%
175	0.00%	21.43%	42.86%	92.86%	100.00%	100.00%
200	8.33%	25.00%	58.33%	100.00%	100.00%	100.00%

Table 5.18 POD for C-SG-CB(1)-V with different group sizes and different damage levels

Group Size	Level0 (False Alarm)	Level1	Level2	Level3	Level4	Level5
1	0.24%	0.32%	0.53%	1.41%	6.42%	24.59%
5	0.20%	0.20%	1.41%	8.89%	50.71%	91.92%
10	0.00%	0.00%	2.43%	13.77%	68.02%	97.17%
20	0.00%	0.81%	4.88%	26.02%	83.74%	99.19%
30	0.00%	2.44%	9.76%	29.27%	92.68%	98.78%
40	0.00%	0.00%	8.20%	39.34%	96.72%	100.00%
50	0.00%	0.00%	4.08%	42.86%	100.00%	100.00%
60	0.00%	0.00%	7.32%	46.34%	97.56%	100.00%
70	0.00%	0.00%	8.57%	45.71%	97.14%	100.00%
80	0.00%	0.00%	13.33%	53.33%	100.00%	100.00%
90	0.00%	0.00%	11.11%	48.15%	100.00%	100.00%
100	0.00%	0.00%	12.50%	54.17%	100.00%	100.00%
125	0.00%	0.00%	21.05%	52.63%	100.00%	100.00%
150	0.00%	0.00%	18.75%	62.50%	100.00%	100.00%
175	0.00%	0.00%	28.57%	64.29%	100.00%	100.00%
200	0.00%	0.00%	33.33%	66.67%	100.00%	100.00%

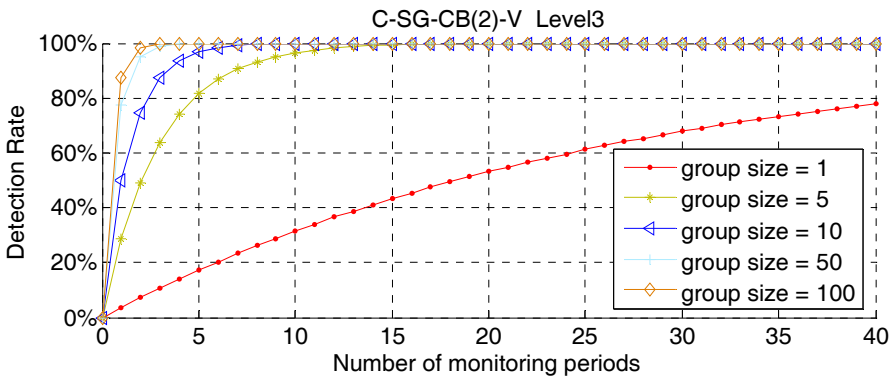

a. slight damage

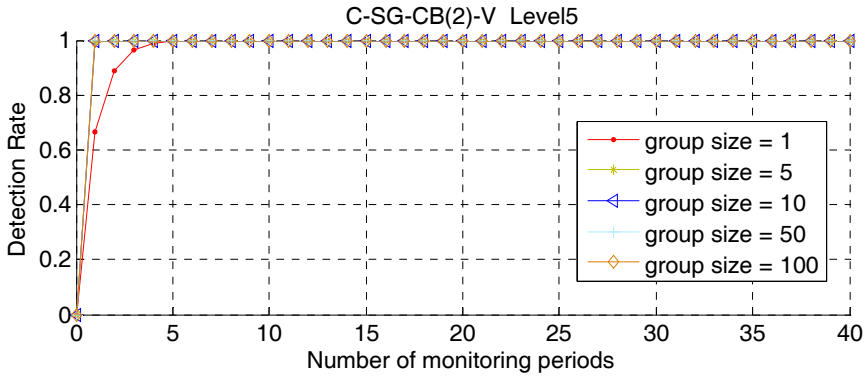

b. relatively heavy damage

Figure 5.33 The relationship between detection rate and the number of monitoring periods

In practice, users care more about the detection delay in terms of number of trucks (n_{trucks}) instead of the number of monitoring periods (or number of truck groups, n_{group}) discussed above. Converting n_{group} to n_{trucks} is not difficult, and it is shown in Eq.5.15. The equation indicates that

$$n_{trucks} = group\ size \times n_{group} \qquad \text{Eq.5. 15}$$

n_{trucks} is not only related to n_{group} but the group size. For slight damages, as discussed before, larger group sizes lead to smaller n_{group}. However, since the group size is larger, the n_{trucks}, which is the product of the group size and n_{group}, is not necessarily small. For heavy damages, n_{group} is almost the same for most group sizes, so smaller group size can result in smaller n_{trucks}. Figure 5.34 shows the relationship between the detection delay (n_{trucks} when DR is not smaller than 99%) and the group sizes for Level1 to Level5 damages. It can be seen that for each damage level, there is a minimum n_{trucks} (highlighted by a red circle in the figure). The group size associated with the minimum n_{trucks} is taken as the optimal group size. For Level1 damage, the optimal group size is 70. Even with the

optimal group size, 2500 trucks are required to achieve the 99% detection rate. On average, 100 right-lane, five-axle, heavy trucks pass the demonstration bridge per day, so Level1 damage can not be reliably detected until 25 days after it occurred. With the long detection delay, the damage can evolve into a higher level damage before being detected. For Level2 damage, the optimal group size is 10 and the corresponding n_{trucks} can be determined as 460 from Fig. 5.34 b. Figure 5.34c shows that the group size of 10 is optimal for Level3 damage as well, and the associated minimum n_{trucks} is 70. For damage Level4 and Level5, the optimal group sizes are determined to be five. However, if group sizes of 10 are used, the n_{trucks} will not increase too much. For Level4 damage, it increases from the minimum value of 20 to 30, for Level5 damage, n_{trucks} increases from 5 to 10. Detecting small damages earlier is the objective of the SHM, therefore the group size of 10 is recommended for the system.

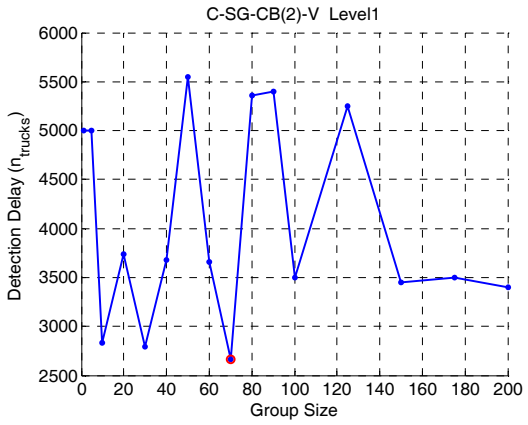

a. Level1 damage

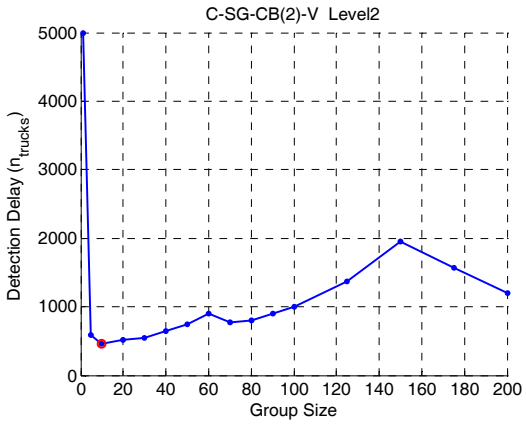

b. Level 2 damage

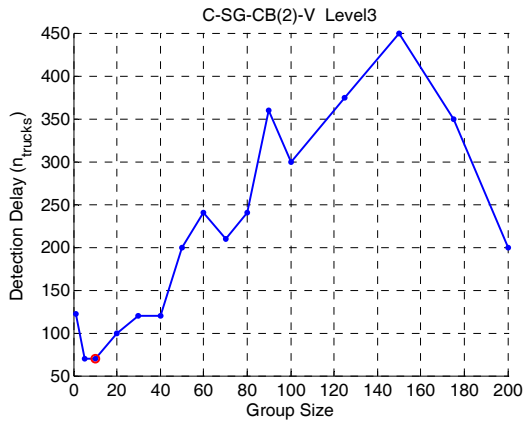

c. Level3 damage

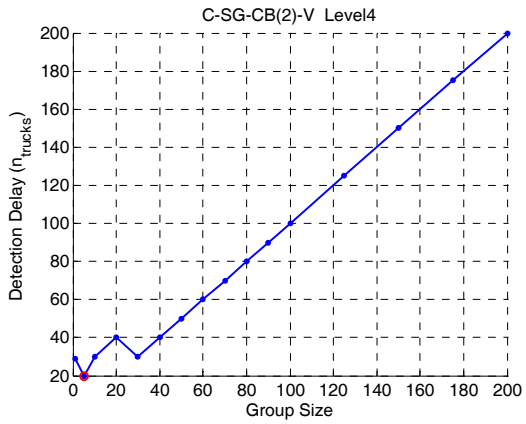

d. Level4 damage

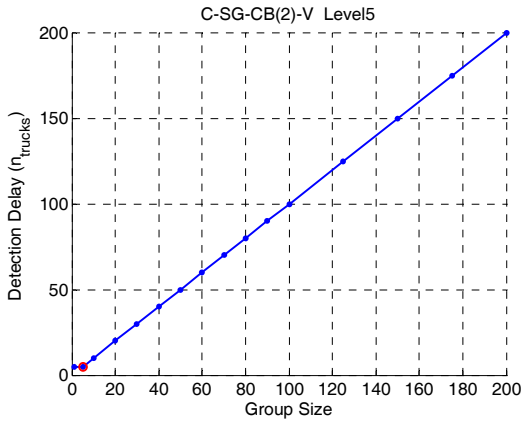

e. Level5 damage

Figure 5.34 The relation between detection delay (n_{trucks}) and group size for each damage level

5.6.2 Application for Other Type of Damages

Although fatigue cracks in the cut-back area was the primary reason the proposed damage detection algorithm was developed, the application of the algorithm is not limited to this type of damage. The one-to-one model used in the algorithm involves all sensors equally in the performance cross prediction procedure. So as long as there is a sensor within the damage influence area, the damage detection approach is thought to be virtually equally effective no matter where the damage occurs. To verify this, the direct evaluation method was applied in the detection of the simulated corrosion damage. As discussed in Section 5.2, the damage was simulated by reducing the thickness of the bottom flange elements of south girder. The sensor B-SG-BF-H is located on the boundary of the damage. FEA results show that the damage affect B-SG-BF-H and B-NG-BF-H. Reviewing the control chart analysis results can find that alarms were created only by these two sensors also. As an example, control charts for B-SG-BF-H at different corrosion levels are shown in Fig. 5.35. The PODs for sensor B-SG-BF-H and B-NG-BF-H at different corrosion levels are summarized in Table 5.19. The table indicates that for the same corrosion level, the POD associated with sensor B-SG-BF-H is always higher than B-NG-BF-H. So the sensor nearer to the damage can detect it earlier than other sensors. To be clear, Fig. 5.36a&b present the relationship between the number of trucks and the detection rate for sensor B-SG-BF-H and B-NG-BF-H, respectively. As can be seen, with the same number of trucks and the same corrosion level, sensor B-SG-BF-H always show higher detection rate than B-NF-BF-H.

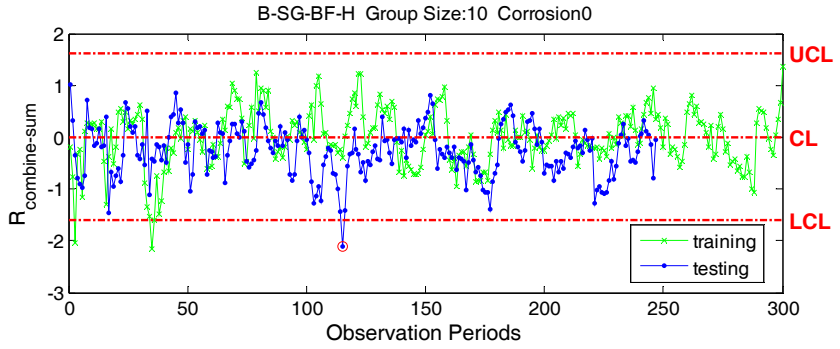

a. Corrossion0

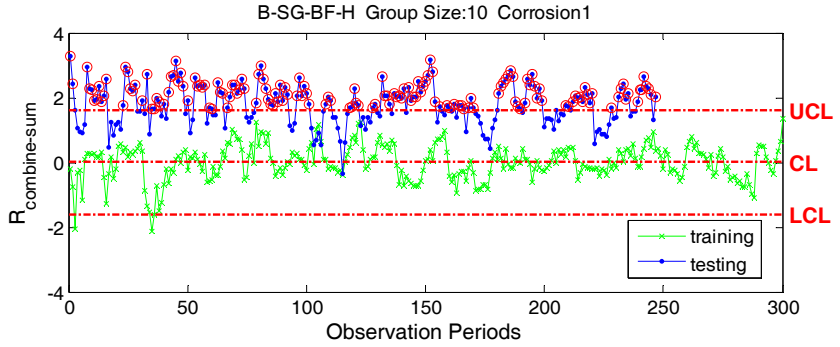

b. Corrossion1

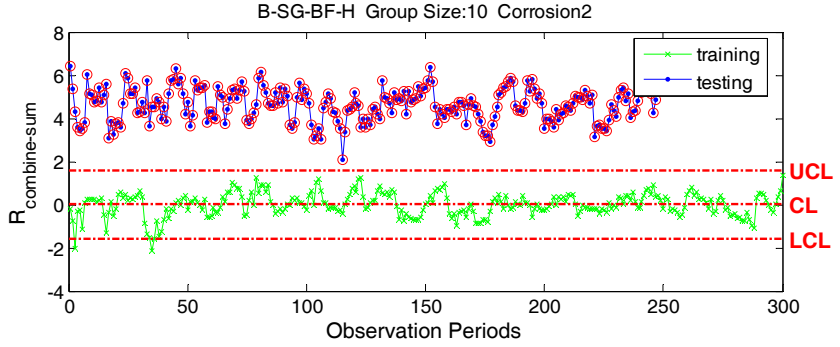

c. Corrossion2

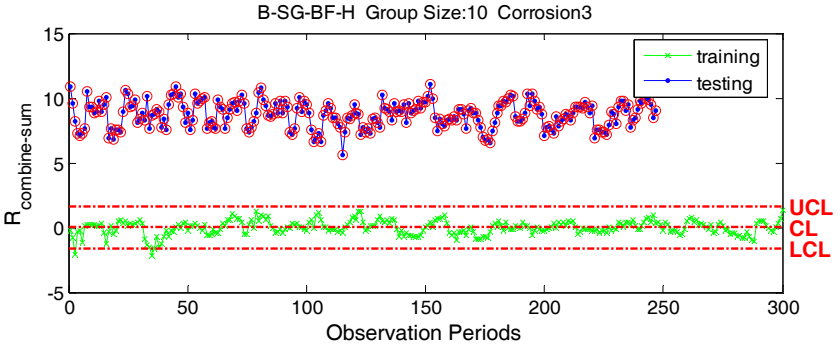

d. Corrossion3

Figure 5.35 Control charts for B-SG-BF-H at different corrosion levels

Table 5.19 The PODs for sensors B-SG-BF-H and B-NG-BF-H

Corrosion Level	POD	
	B-SG-BF-H	B-NG-BF-H
Corrossion0	0.41%	0.00%
Corrossion1	62.35%	1.22%
Corrossion2	100.00%	4.86%
Corrossion3	100.00%	40.89%

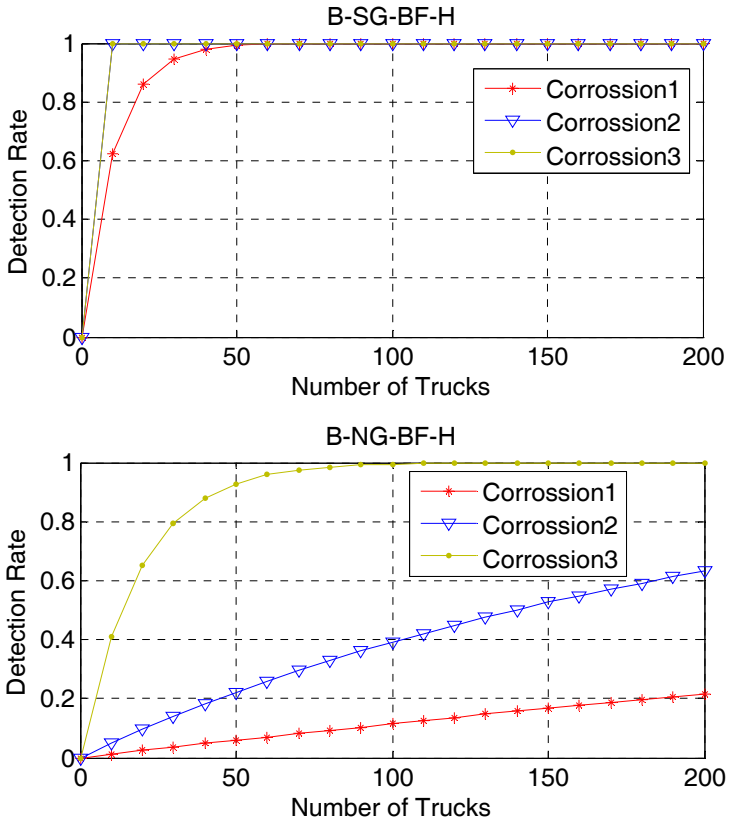

Figure 5.36 The detection rate for sensor B-SG-BF-H and B-NG-BF-H

5.7 Summary

In this work, a novel strain based damage detection approach was developed. The residuals calculated from linear prediction models were used as the basic format of the damage indictor, and it was shown to be more damage sensitive than using strain directly. Studies also indicated that the strain range is more damage sensitive than event extreme strains. Simulation results showed that among the studied methods, the one-to-one model direct evolution method is the most effective in terms of both the damage occurrence and damage location detection. With the unique one-to-one

model, the developed damage detection approach can be applied for virtually all types of steel bridges and can detect all types of damage.

CHAPTER 6 SUMMARY, CONCLUSIONS AND FUTURE WORK

6.1 Summary

In a previous project, a FOS SHM system was developed that enables bridge owners to remotely monitor bridges for gradual and sudden damage formation. However, the correlation between the data analysis results and damage was not objectively defined; bridge owners need to interpret the results according to their experiences, which might be subjective. To improve the existing SHM system, a statistical damage detection method was proposed and analytically evaluated.

The basic idea of this method is that the response of a normal structure is different from that of the damaged structure. To define the difference mathematically, Shewhart $\bar{X}$ control chart analysis was carried out over a strategically defined damage indicator. Compared to use the strain directly, it was found that the residual calculated from cross prediction models is more sensitive to structural damage and immune to load condition variations. With different prediction models and different damage indicator calculation procedures, three damage detection methods (one-to-one model direct evaluation method, two-level evaluation method, and many-to-one model method) were studied. Each method has its advantages and disadvantages. The first method (e.g. one-to-one model direct evaluation method) was shown to be the most damage sensitive and the most effective in damage location detection. However, its implementation is relatively complicated and the simplified residual matrix does not have a clear physical meaning. For the second method (e.g. two-level evaluation method), which uses the simplified evaluation matrix as the damage indicator, the physical meaning of the indicator is clear (i.e. the number of failed first level evaluation). However, this method is not sensitive to small damage due to the loss of important information inherent to this process. The advantages of the third method (e.g. many-to-one model method) are obvious; the implementation procedure is simpler than the other two methods and its damage sensitivity is comparable to the first method. However, the simulation results indicated that this method is not effective in terms of the damage location detection. As a result of the overall study, the one-to-one model direct evaluation method is recommended.

For the recommended damage detection method, studies were carried out to compare the performance matrix selection, the truck group selection, and residual matrix simplification

procedure selection. The simulation results showed that the strain range is the most damage sensitive performance measurement, and it was utilized in the one-to-one model creation. It was also verified that using right-lane, five-axle, heavy trucks can achieve better damage detection results than using light trucks or using all trucks as a single group. Among the three residual matrix simplification approaches (row summation, column summation, and combined summation), the combine summation was found to be the most damage sensitive.

The recommended damage detection approach was developed with the following three major steps.

Step 1, data preprocessing. The strain variance caused by determinable factors, such as the thermal effect, vibration produced by vehicles and the interaction between vehicles and the bridge, and the variance caused by different truck types, were removed from the raw data. The unique truck parameter detection/calculation method developed in this research allows for truck selection which improves the sensitivity of the damage detection method significantly.

Step 2, system training. In the training procedure, one-to-one linear regression prediction models are trained with field collected undamaged structural data. Using the prediction models, a 40×40 residual matrix is calculated for each truck event. The combine summation simplification approach is then employed to simplify the residual matrix into a 1×40 combine-sum-rsd vector, so that one baseline control chart is created for each sensor. As the distributions of the elements of combine-sum-rsd are roughly normal, the control limits are set to be $\mu\pm3\sigma$.

Step 3, structural monitoring. During the monitoring stage, the current structural state is determined by comparing the current performance with that of the undamaged structure using the control charts developed in Step 2. For each preprocessed monitoring data set, the same residual matrix calculation and simplification procedure used in Step 2 is repeated to calculate the combine-sum-rsd vector. The comparison is accomplished by plotting the elements of combine-sum-rsd onto the corresponding baseline control charts established during system training. Out-of-limits points indicate structural damage and the position of the associated sensor indicates the general damage location.

The above outlined damage detection approach was evaluated with FEA simulation data. The results of the evaluation indicated that:

1. Using a group size of 10 can achieve the earliest detection for slight damages while keeping the detection delay reasonable for relatively large damage.

2. For the demonstration bridge, C-SG-CB(2)-V can always detect the simulated fatigue cracks earlier than C-SG-CB(1)-V does. By controlling the false alarm rate to around 0.3% using a group size of 10, the POD for Level2 damage is 9.72%, and on average the damage detection rate can achieve 99% with 460 trucks passing the bridge; for Level3 damage the detection delay was reduced to 70 trucks. When Level5 damage occurs, it can be detected after 10 trucks passing. Not surprisingly, severe damage can be detected sooner than slight damage. The detection delay for Level1 damage is long, and the damage can evolve into higher level damage before being detected.
3. Study of the detection of corrosion damage indicated that with a 0.3% false alarm rate and a group size of 10, the POD is 62.35% for Corrossion1 and 100% for Corrossion2, and the corresponding detection delay is 50 and 10 trucks, respectively.

6.2 Conclusions

Reviewing the various aspects of this research, the following conclusions can be made about the developed truck detection sub-system and the damage detection approach:

1. The developed strain based truck detection sub-system can detect truck events and calculate relevant parameters including the number of axles, axle spacings, speed, event start and end time, and weight group autonomously in a near-real-time fashion. The sub-system has been integrated into the existing SHM system successfully. The truck parameter detection function allowed for a successful data selection procedure. Using a single truck type during the structural evaluation improved the performance of the system significantly.
2. By using the uniquely one-to-one cross prediction model, sensors in the SHM system can be used as both TS and NTS; and the developed damage detection approach can be applied for virtually all types of bridges.
3. Using the simplified residual as the damage indicator enabled reliable mathematical control limits selection. The control chart analysis results can show not only the damage occurrence but the damage location. The strategically defined damage indicator significantly improved the damage detection power of the method.
4. The damage sensitivity (measured by POD and detection delay) and the damage location detection ability of the recommended one-to-one model direct evaluation method were evaluated using the synthetic data. The optimal group size was recommended based on the simulation results.

6.3 Future Work

In future, additional effort is required to further verify and improve the developed damage detection method:

1. Verify the recommended damage detection method with field collected data. The POD and detection delay information obtained from field collected post-damage data is more reliable than the simulation results.
2. Schewart control chart concepts were used in the developed damage detection method. In the future; the CUSUM control chart should also be investigated. CUSUM charts, while not as intuitive and simple to operate as Shewhart charts, have been shown to be more efficient in detecting small shifts in the mean of a process. So, theoretically, a more damage sensitive method may be achievable by using CUSUM charts.
3. Comparing the performance of the Schewart charts based method and CUSUM charts based method using the field collected data.

REFERENCES

Aktan, E., S. Chase, D. Inman, D. Pines (2001), "Monitoring and Managing the Health of Infrastructure Systems", Proceedings of the SPIE Conference on Health Monitoring of Highway Transportation Infrastructure, March 6-8.

Alampalli, S., G. Fu (1994), "Instrumentation for remote and continuous monitoring of structure conditions", Transport. Res. Rec. No.1432, 59-67.

Bakht, B., J. G. Jaeger (1990), "Bridge testing: a surprise every time", ASCE J. Struct. Eng. Vol.116 (5), 1370-1383.

Balageas, D., C.-P Fritzen, A. Güemes (2006), Structural Health Monitoring, ISET Ltd., London, UK.

Bampton, M. C. C., J. V. Ramsdell, R. E. Graves, L. A. Strope (1986), Deer Isle-Sedgwick suspension bridge, Wind and motion analysis, Report FHWA/RD-86/183.

Barr, I. G., P. Waldron, H. R. Evans (1987), "Instrumentation of glued segmental box girder bridges", Proc. IABSE colloquium - monitoring of large structures and assessment of their safety, Bergamo, October.

Brownjohn, J. M. W. (2007), "Structural health monitoring of civil infrastructure", Phil. Trans. R. Soc. A365, 589-622.

Brownjohn, J. M. W., M. Bocciolone, A. Curami, M. Falco, A. Zasso (1994), "Humber Bridge fullscale measurement campaigns 1990–1991", J. Wind Eng. Ind. Aerodyn. Vol.52, 185–218.

Brownjohn, J. M. W., P. Moyo, C. Rizos, S. C. Tjin (2003a), "Practical issues in using novel sensors in SHM of civil infrastructure: problems and solutions in implementation of GPS and fiber optics", Proc. 4th Int. workshop on structural health monitoring, Stanford University, 499-506.

Brownjohn, J. M. W., Moyo, P., Omenzetter, P. & Lu, Y. (2003b), "Assessment of highway bridge upgrading by dynamic testing and finite element model updating", ASCE J. Bridge Eng. Vol.8, 162-172.

Carder, D. S. (1937), "Observed Vibrations of Bridges". Bull. Seismol. Soc. Am. Vol.27, 267-303.

Catbas, F. N., S. K. Ciloglu, K. A. Grimmelsman, A. E. Aktan (2001). "Issues in fleet health monitoring of aged concrete T-beam bridges in Pennsylvania", Proceedings of the 80th Annual meeting of the transportation research board, Washington DC, 7-11 January.

Cheung, M. S., G. S. Tadros, J. Brown, W. H. Dilger, A. Ghali, D. T. Lau (1997), "Field monitoring and research on performance of the Confederation Bridge", Can. J. Civil Eng. Vol.24, 951-962.

Deraemaekera, E. Reyndersb, G. D. Roeckb, J. Kullaa (2008), “Vibration-based structural health monitoring using output-only measurements under changing environment”, Mechanical Systems and Signal Processing, Vol.22, 34-56.

Doebling, S. W., C. R. Farrar, M. B. Prime (1998), “A summary review of vibration-based damage identification methods”, The Shock and Vibration Digest, Vol.30(2), 91-105.

Doornink, J. D. (2006), Monitoring the Structural Condition of Fracture-Critical Bridges Using Fiber Optic Technology, Ph.D. dissertation, Iowa State University.

Dubin, E.E., B.S. Yanev (2001), “Managing the east river bridge in New York city”, Proceedings of the 7th international symposium on smart structures and materials, Newport, CA, 4-8 March.

Farrar, C.R., W.E. Baker, T.M. Bell, K.M. Cone, T.A. Duffey, A. Eklund, A. Migliori (1994), “Dynamic Characterization and Damage Detection in the I-40 Bridge over the Rio Grande”, Loa Alamos National Laboratory Report: LA-12767-MS.

Farrar, C. R., and S. W. Doebling (1997), “An overview of modal-based damage identification methods”, Proc. of EUROMECH 365 International Workshop: DAMAS 97- Structural Damage Assessment Using Advanced Signal Processing Procedures, June/July, Sheffield, U.K.

Farrar, C. R., S. W. Doebling (1999). ‘‘Vibration-based structural damage identification.’’ Philosophical Trans. Royal Soc.: Math., Phys. and Engrg. Sci., London.

Fisher, J.W. (1984), Fatigue and fracture in steel bridges: case studies, Wiley, New York.

Flannigan, J. C. (2006), Acoustic Emission Monitoring on Fiber Reinforced Bridge Panels, master thesis, Kansas State University.

Flint, A. R., B. W. Smith (1992), “Strengthening and refurbishment of Severn Crossing -- Part 5: Other background research and development”, ICE Proceedings: Structures and buildings, Vol.94 (1), 51-60.

Fraser, M. S. (2006), Development and implementation of an integrated framework for structural health monitoring, Doctor Dissertation, University of California, San Diego.

Fritzen, C. P., D. Jennewein, T. Kiefer (1998), “Damage detection based on model updating methods”, Mechanical Systems and Signal Processing, Vol.12(1), 163-186.

Fugate, M., H. Sohn, C. R. Farrar (2001), “Vibration-Based Damage Detection Using Statistical Process Control”, Mechanical Systems and Signal Processing, Vol.15(4), 707-721.

Fujino, Y. and Abe, M. (2003), “Structural monitoring in civil infrastructures— research activities at the Bridge and Structure Laboratory of the University of Tokyo”, The First International Conference on Structural Health Monitoring and Intelligent Infrastructure, 13 -15 November, Tokyo, Japan, 39-50.

Fujimoto, Y., J. Yue (2005). “Depth estimation of surface cracks based on the measurement of crack opening deformation and numerical-experimental iteration”, Journal of Marine Science and Technology, Vol.10(4), 203-210.

Geier, R., H. Wenzel (2002), “Bridge classification based upon ambient vibration monitoring”, Proc. First European conference on structural health monitoring, Paris, 981-988.

Gope, J. K., Ramdas, C. (2005), “Damage identification from simple static strain data using neural network”, Proceedings of ISSS International Conference on Smart Materials Structures and Systems, July 28-30, Bangalore.

Grant, E.L., R.S. Leavenworth (1996), Statistical quality control, The McGRAW-Hill companies, INC.

Heywood, R. J., W. Roberts, R. Taylor, R. Anderson (2000), “Fitness-for-purpose evaluation of bridges using health monitoring technology”, Transport. Res. Rec. No.1696, 193-201.

Higgins, M. S., C. Randy, K. Frank (2006), “Acoustic Monitoring on the Fred Hartman Bridge: Understanding the Condition of Stay Cable”, Sixth International Symposium on Cable Dynamics, Charleston SC, USA.

Hu, X., H. W. Shenton (2003), “Damage identification in a two span continues beam”, Proceedings of the First International Conference on Structural Health Monitoring and Intelligent Infrastructure, Tokyo, Japan, Nov. 13-15.

Idriss, R. L., R. Kenneth, C. B. White, J. M. Woodward, D.V. Jauregui (1995), "Evaluation and Testing of a Fracture Critical Bridge: The I-40 Bridges over the Rio Grande-Case Study", Journal of NDT and E International, Vol.28(6), 339-347.

Inman, D.J., S. W. Farrar, V. Lopes Junior, V. Steffen Junior (2004), “Damage Prognosis for Aerospace, Civil and Mechanical Systems”, John Wiley & Sons, Ltd.

Ihn, J. B., F. K., Chang (2004a), “Detection and monitoring of hidden fatigue crack growth using a built-in piezoelectric sensor/actuator network: I. Diagnostics.” Smart Materials and Structures, Vol.13, 609-620.

Ihn, J. B., F. K., Chang (2004b), “Detection and monitoring of hidden fatigue crack growth using a built-in piezoelectric sensor/actuator network: II. Validation using riveted joints and repair patches”, Smart Materials and Structures, Vol.13, 621-630.

Kesavan, A., M. Deivasigamani, S. John, I. Herszberg (2005), “Damage criticality assessment in complex geometric structures using static strain response-based signal Processing Techniques”, Smart Structures and Integrated Systems, Proceeding of SPIE, Vol.5764, 542.

Kim, J. T. (1995), “Robust Damage Localization Algorithm for Highway Plate-Girder Bridges”, Proc. SPIE, smart strucu. & Mat., Smart Systems for Bridges, structures and Highways.

Ko, J.M., Z. G. Sun, Y. Q. Ni (2002), “Multi-stage identification scheme for detecting damage in cable-strayed Kap Shui Mun Bridge”, Engineering Structures, Vol.24 (7), 857-868.

Koh, H. M., J. F. Choo, S. K. Kim, C. F. Yim (2003), “Recent application and development of structural health monitoring systems and intelligent structures in Korea”, Proc. SHMII- 1, Structural Health Monitoring and Intelligent Infrastructures, Vol.1, 99-112.

Kowalik, A., Acoustic Monitoring on the Fred Hartman Bridge. Bridge Division, Texas Department of Transportation. from http://www.txdot.gov/publications/bridge/hartman_acoustic_monitoring.pdf.

Kullaa, J. (2003), “Damage detection of the Z24 Bridge using control charts.” Mechanical Systems and Signal Processing, Vol.17(1), 163-170.

Kullaa, J. (2003), “Is Temperature Measurement Essential in Structural Health Monitoring”, Proceedings of the 4th International Workshop on Structural Health Monitoring, Stanford University, Stanford, CA, Sep 15-17.

Li, J., Zhang, Y. (2006). "Prediction error method-based second-order structural identification algorithm in stochastic state space formulation", Earthquake Engineering and Structural Dynamics, Vol.35, 761-779.

List, D. (2004), “Rejuvenating the Tamar Bridge: A review of the strengthening and widening project and its effect on operations”, Proc. 4th Int. Cable Supported Bridge Operators’ Conference, Copenhagen.

Lu, P., B. M. Phares, H. Ceylan, T. J. Wipf (2006), “A Three-Stage Structural Damage Detection Approach Using Artificial Neural Networks”, Proceeding of Artificial Neural Networks n Engineering, Nov.5-8, St. Louis, USA.

Mita, A. (1999), “Emerging needs in Japan for health monitoring technologies in civil and building structures”, Proc. 2nd Int. workshop on structural health monitoring, Stanford University.

Moses, F. (1979), “Weigh-in-motion System Using instrumented Bridges”, Transportation Engineering Journal, Vol.105(3), 233-249.

Nagayama, T., M. Abe, Y. Fujino, K. Ikeda (2004), “Structural Identification of Nonproportional Damped Systems and Its Application to a Full Scale Suspension Bridge”, J. Struct. Eng, Vol.131(10), 1536-1545.

Ni, Y. Q., B. S. Wang, J. M. Ko (2002), “Constructing input vectors to neural networks for structural damage identification”, Smart Mater. Struct., Vol.11, 825-833.

Ou, J.P. (2003), “some recent advances of intelligent health monitoring systems for civil infrastrucres in Mainland china”, Proc. SHMII-1, Structural Health Monitoring and Intelligent Infrastructures, Vol.1, 131-144.

Phares, B. (2001), “Highlights of study of reliability of visual inspection”, Presentation at the Annual Meeting of TRB Subcommittee A2C005(1) non-destructive Evaluation of Structures. Report is also available from FHWA Turner Fairbanks Research Center.

Pines, D. (2001), “Ongoing Research and Development in the U.S. on Structural Health Monitoring”, 7th International Seminar on Seismic Isolation, Passive Energy Dissipation and Active Control of vibrations of Structures, October 2-5.

Prine, D. W. (1995), “Application of Acoustic, Strain, and Optical Sensors to NDE of Steel Highway Bridges”, Sensors Expo Conference, 16 May, BIRL Industrial Research laboratory, Northwestern University.

Roddis, W.M.K., Y. Zhao (2003), “Finite-element analysis of steel bridge distortion-induced fatigue”, Journal of Bridge Engineering, Vol.8(5), 259-266.

Ross, R. M. and Matthews, S. L. (1995), “In-service structural monitoring—a state of the art review”, Struct. Eng. Vol.73, 23-31.

Salane, H. J., J. W. Baldwin, R. C. Duffield (1981), “Dynamics approach for monitoring highway bridge deterioration”, Transport. Res. Rec. No.832, 21-28.

Schulz, W.L., E. Udd, J.M. Seim, G.E. McGill (1998), “Advanced fiber grating strain sensor systems for bridges, structures, and highways”, SPIE proceedings series, Vol. 3325, 212-221.

Seible, F., G. Hegemier, V. Karbhari, A. Davol (1996), The I-5/Gilman Advanced Composite Cable Stayed Bridge Study, University of California, San Diego, SSRP Report-96/05.

Sohn, H., J. J. Czarnecki, C.R. Farrar (2000), “Structural Health Monitoring Using Statistical Process Control”, Journal of Structural Engineering, Vol. 126 (11), 1356-1363.

Sohn, H., C. R. Farrar, N. F. Hunter, K. Worden (2001), Applying the LANL Statistical Pattern Recognition Paradigm for Structural Health Monitoring to Data from a Surface-Effect Fast Patrol Boat, LA-13761-MS.

Sohn, H., C. Farrar, F. Hemez, D. Shunk, D. Stinemates, and B. Nadler (2003), “A review of structural health monitoring literature: 1996 – 2001.” Los Alamos National Laboratory Report, LA-13976-MS.

Sun, Z., C. C. Chang (2004), “Statistical Wavelet-Based Method for Structural Health Monitoring”, Journal of Structural Engineering, Vol.130(7), 1055-1062.

Tikka, J., R. Hedman, A. Siljander (2003), “Strain Gauge Capabilities in Crack Detection”, 4th International Workshop on Structural Health Monitoring, Stanford, CA, Sept.15-17.

University of Washington (1954), Aerodynamic stability of suspension bridges with special reference to the Tacoma Narrows Bridge. Bulletin No. 116, University of Washington Engineering Experiment Station, Seattle, Washington.

Wang, C. Y., H. L. Wang, C. Y. Wu, C. H. Chen (2003), “Development of bridge health monitoring systems in Taiwan”, Proc. SHMII-1, Structural Health Monitoring and Intelligent Infrastructures, Vol.2, 1067-1072.

Wang, Y., K. J. Loh, J. P. Lynch, M. Fraser, K. Law, A. Elgamal (2006), “Vibration Monitoring of the Voigt Bridge using Wired and Wireless Monitoring Systems”, Proceeding of 4th China-Japan-US Symposium on Structural Control and Monitoring, Oct.16-17.

Wipf, T.J., B.M. Phares, L.F. Greimann, D. Hemphill, J.D. Doornink, P. Lu (2006), “Remote Continuous Evaluation of a Bridge Constructed Using High-Performance Steel”, Report to the Iowa Department of Transportation, Bridge Engineering Center, Iowa State University, May.

Wong, K. Y. , C.K. Lau (2000), “Planning and implementation of the structural health monitoring system for cable-supported bridges in Hong Kong”, Nondestructive Evaluation of Highways, Utilities, and Pipelines IV, Proceedings of SPIE 3995, 266-275.

Wong, K. Y. (2003), “Instrumentation and health monitoring of cable-supported bridges. Struct”, Control Health Monit. Vol.11, 91-124.

Wu, Z.S. (2003), “structural health monitoring and intelligent infrastructures in Japan”, Proc. SHMII-1, Structural Health Monitoring and Intelligent Infrastructures, Vol. 1, 153-170.

Xia, Yong, Y. Fujino, M. Abe, J. Murakoshi (2005), “Short-term and long-term health monitoring experience of a short highway bridge: case study”, Bridge Structures, Vol.1(1) 43-53.

Yan, A.M., G. Kerschen, P. De Boe, J.-C. Golinval (2005), “Structural damage diagnosis under varying environmental conditions—Part I: A linear analysis”, Mechanical Systems and Signal Processing, Vol.19, 847-864.

Yanev, B. (2003), “Structural Health Monitoring as a Bridge Management Tool”, Proc. SHMII-1, Structural Health Monitoring and Intelligent Infrastructures, Vol.1, 87-98.

APPENDIX A TRUCK WEIGHT CALCULATION

Early in the project it was postulated to be possible to calculate the truck weight using weight in motion (WIM) concepts. Although FEA results showed the feasibility, controlled test results were not satisfactory. This indicated that the WIM concept is not applicable for the selected demonstration bridge. The global strain effects produced by different axles of a truck are not completely decomposable. Nevertheless, the utilized WIM concept and the verification procedure are summarized in the following.

1. WIM Concept

Many WIM algorithms have been studied in the literature. The one used in this project was first proposed by Moses (1979). The algorithm was field verified on a three span bridge, which has six continuous steel girders and no skew. Theoretical influence line was used in the verification, and it was claimed to be effective for any beam-slab bridge.

In the proposed approach, the influence line for a selected sensing point was calculated from the strain responses produced by field testing. The field calibrated influence line is considered to be more accurate than the theoretical one. The truck speed, event start time, and axle distances were known, so the position of each truck axle could be computed for any time instance. With the truck axle positions and the influence line known, the theoretical strain response can be calculated for any truck location. At the same time, the monitoring strain response is available as well. Thus, the weights of individual truck axles could be determined by minimizing the difference between the calculated and the monitoring strain responses. The total truck weight is simply the summation of the axle weights.

In short, implementing the WIM concept needs two key steps: 1) obtain the influence line, and 2) calculate the axle weight by minimizing the difference between the monitoring and calculated strain responses.

2. FEA feasibility study

<u>2.1 Influence line generation</u>

The finite element structural and load models introduced in section4.2.2.1 were used here. To calculate the influence line for the point where sensor B-SG-BF-H was installed, FEA was carried out using a single dump truck but with three different load levels. Two percent normal distributed random noises were added to the FEA strain results to simulate the monitoring data. The geometry and axle weights of the three dump trucks are shown in Fig A.1 a&b. The simulated strain responses are plotted in Fig A.1c. When the first axle of the truck is located at a point (P in Fig A.2), the total strain $R_i(P)$ can be expressed as the sum of each axle weight of i-th truck times the influence line value at the axle position. The coefficients of W_{ij} and $R_i(P)$ in (A.1) are known, and they defined an independent and consistent linear system. Therefore the influence line instance I(P) can be uniquely solved from the system. The weights of two axles of the tandem group were assumed to be the same, I(P) can be solved from any two equations of (A.1) . When the first and the last equations are used, the solution is shown in (A.2). Repeating the simultaneous equations solving procedure for all truck positions we can obtain the entire influence line, which is shown in Fig A.2.

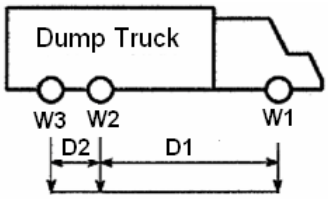

a. Truck configuration

	W1 (k)	W2 (k)	W3 (k)	D1 (ft)	D2 (ft)
Run1	5.6	7.89	7.89	14	4.5
Run2	4.48	4.73	4.73	14	4.5
Run3	3.92	2.367	2.367	14	4.5

b. Truck axle weights and axle distances

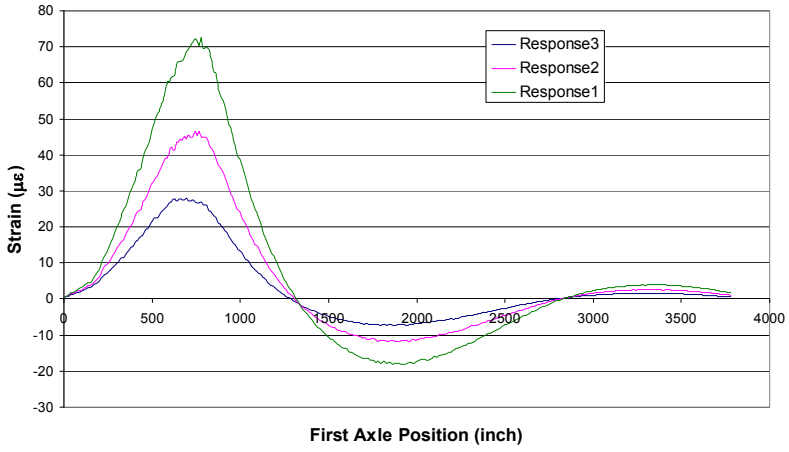

c. The strain response of the truck at different load levels

Figure A.1 The strain data used for influence line generation

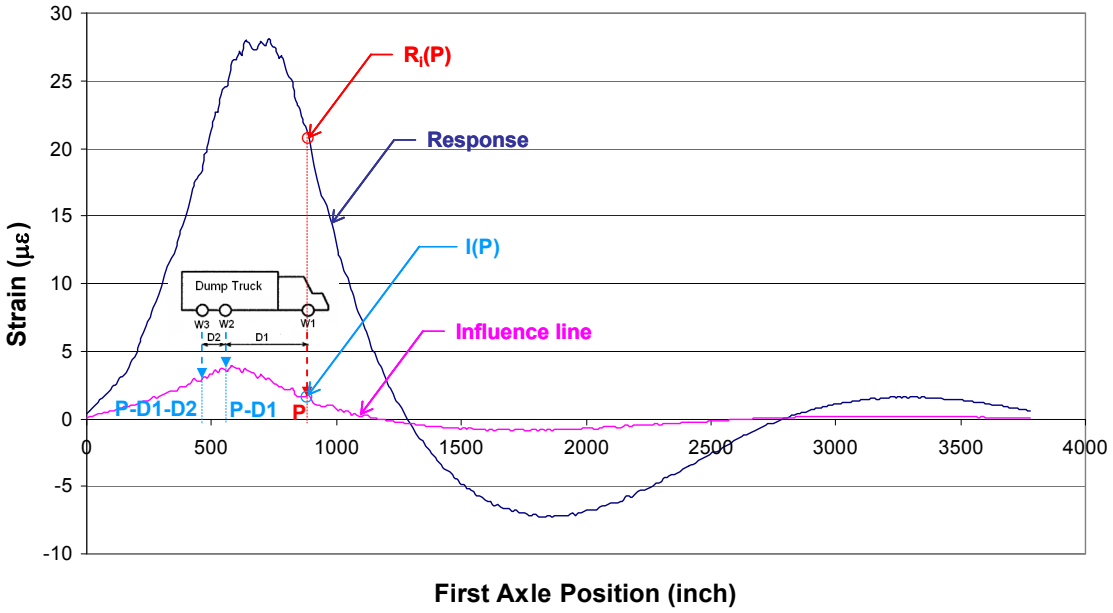

Figure A.2 The influence line calculation

$$\begin{bmatrix} W_{11} & W_{12} & W_{13} \\ W_{21} & W_{22} & W_{23} \\ W_{31} & W_{32} & W_{33} \end{bmatrix} \begin{bmatrix} I(P) \\ I(P-D_1) \\ I(P-D_1-D_2) \end{bmatrix} = \begin{bmatrix} R_1(P) \\ R_2(P) \\ R_3(P) \end{bmatrix} \quad \text{(A.1)}$$

$$I(P) = \frac{W_{32}R_1(P) - W_{12}R_3(P)}{W_{32}W_{11} - W_{12}W_{31}} \quad \text{(A.2)}$$

In which, W_{ij} is the weight of the *j-th* axle of the *i-th* truck;

I(P), I(P-D1), I(P-D2) are the influence line values at the point of P, P-D1, and P-D2;

$R_i(P)$ is the response produced by *i-th* truck when its first axle is located at point P.

2.2 Truck weight calculation

By extending the three axle dump truck case shown in (A.1) to an n-axle truck case, the theoretical strain response, when the first truck axle is located at position P, can be calculated as (A.3). The corresponding monitoring response data was simulated by adding 2% random noises to the FEA strain results. The axle weight of the truck was then calculated by minimize the objective function of (A.4) using the least square error optimization method.

$$\begin{pmatrix} I(P) & I(P-D_1) & I(P-D_1-D_2)\ldots & \ldots & I(P-D_1-\ldots-D_{n-1}) \end{pmatrix} \begin{bmatrix} W_1 \\ W_2 \\ W_3 \\ \vdots \\ \vdots \\ W_n \end{bmatrix} = R\_caculated(P, W_1, W_2, \ldots, W_n) \quad \text{(A.3)}$$

$$objective\ function = R\_calculated(P, W_1, W_2, \ldots, W_n) - R\_monitoring(P) \quad \text{(A.4)}$$

As discussed before, the dump truck (Fig A.1) Run1 and Run3 data were used to generate the influence line. So the data of Run2 can be used to verify the weight prediction results. As presented in Table A.1, the axle weight prediction error is smaller than 10%, and the total weight prediction error is no more than 5%. In this verification the target truck has the same geometry configuration as that used in influence line generation. The weight prediction results of two trucks with different geometries than influence generation trucks are shown in Tables A.2 and A.3. It can be seen that the prediction errors are as good as that shown in Table A.1. The results indicated that once the influence line was calculated, it can be applied to calculate the weight of any type of trucks.

Table A.1 Dump truck weight prediction using FEA data(D1 = 14ft, D2 = 4.5ft)

	Actual	Predicted	Error
W1 (k)	8.96	8.80	-2%
W2 & W3 (k)	9.46	10.24	8%
W Total (k)	27.88	29.28	-5%

Table A.2 Dump truck weight prediction using FEA data (D1 = 18ft, D2= 4ft)

	Actual	predicted	Error
W1 (k)	10.00	9.42	-6%
W2 & W3 (k)	14.00	14.10	1%
W Total (k)	38.00	37.62	-1%

Table A.3 Five-axle semi truck weight prediction using FEA data
(D1 = 10ft, D2 = 4ft, D3 = 22ft, D4 = 4ft)

	Actual	Predicted	Error
W1 (k)	12.00	10.76	-1%
W2 & W3 (k)	13.00	13.48	4%
W4 & W5 (k)	15.50	15.22	-2%
W Total (k)	69.00	68.16	-1%

The FEA concluded that the WIM concept may be applicable for the demonstration bridge. To simplify the influence line computation and reduce the required data amount, trucks with fewer

axles are more desirable for influence line generation. Once the influence line was computed, it is applicable for any truck type. Observations show that the prediction error of gross vehicle weight (GVW) is smaller than that of axle weights.

3. BDI testing data study

3.1 Influence line generation

The BDI strain data produced by Dump4 and Dump2 (Table 4.1) were used to generate the influence line. In Fig A.3, the influence line is compared with that obtained from FEA results. Although the overall shapes are similar, the maximum magnitude difference can be as large as 28%. A number of factors contribute to the difference. They include: 1) the weights of the two tandem axles are not exactly same; 2) the dynamic effects were not completely removed by the digital filter; 3) the field data unavoidably contained noises and strains caused by other vehicles; 4) the bridge structure system does not perform exactly the same as the finite element model, and the axle strain effects are not completely decomposable for the demonstration bridge. Among these, the last one is considered to be the most significant.

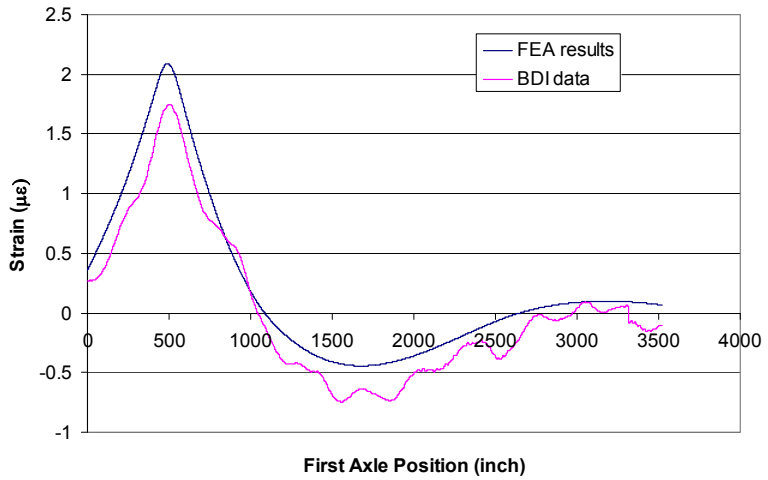

Figure A.3 Comparison of the influence line calculated from BDI data and FEA results

3.2 Truck weight calculation

Following the same optimization procedure introduced in the FEA feasibility study, the truck weights were calculated using the data obtained from the BDI test. Examples of the calculation results for

dump and semi trucks are listed in Tables A.4 and A.5 respectively. As shown, errors of the total weight calculation are less than 10% for dump trucks. However, for 6-axle semi trucks, the errors are found to be between 10% and 25%. The considerable difference between the truck weight prediction qualities for different truck types indicated that the real bridge structure system can not completely decouple the effects of individual axles.

Table A.4 Weight prediction results for a dump truck from control testing data

	Actual	Calculated 1	Calculated 2	Calculated 3	Calculated 4
W1 (k)	13.60	11.78	9.79	11.56	12.10
W2 & W3 (k)	19.39	20.37	21.19	22.16	21.97
Total Weight(k)	52.38	52.52	52.16	55.88	56.04
Error W1		-13.38%	-28.04%	-15.01%	-11.00%
Error W2&W3		5.07%	9.27%	14.29%	13.30%
Error Total Weight		0.28%	-0.42%	6.68%	6.99%

Table A.5 Weight prediction results for a six-axle semi truck from control testing data

	Actual	Calculated 1	Calculated 2	Calculated 3	Calculated 4
W1 (k)	44.76	48.58	-6.58	-35.43	-33.16
W2 & W3 (k)	35.98	25.18	39.43	51.25	49.59
W4-6 (k)	12.41	18.908	19.56	16.78	16.67
Total Weight(k)	153.96	155.66	130.94	117.42	116.03
Error W1		8.53%	-114.70%	-179.16%	-174.09%
Error W2&W3		-30.00%	9.58%	42.45%	37.83%
Error W4-6		52.28%	57.54%	35.18%	34.30%
Error Total Weight		1.10%*	-14.95%	-23.74%	-24.63%

*T*he good total weight prediction result is not reliable since the truck changed speed on the bridge*

APPENDIX B PSEUDO CODE FOR Δt CALCULATION

```
Input: Data11 , Data12 , Data21 , Data22  \*deck-bottom sensor data*\
Output:Δt

for i = 1 to 2    \*line index*\
    for j = 1 to 2  \*sensor index*\
        UBij  = mode(Dataij>0)  \*UBij  is the upper bound
                                    of zero readings for the ith line jth sesnor*\
    end
end

for i = 1 to 2
    for j = 1 to 2
        StrongPeakij  = Peak (Dataij ,3) \*Peak(x,y ) is the peak detection sub-function,
                                          x:input data, and y:threshold*\
        WeakPeakij  = Peak(Dataij , UBij )
    end
end

for i = 1 to 2
    for j = 1 to 2
        PSensorij = StrongPeakij  U WeakPeakij
    end
end

for i = 1 to 2
    PLinei  = PSensori1UPSensori2
end

Num = 0
MaxNum = 0
while 0.4sec < t <  2sec
    for i = 1 to length(PLine1 )
        for j = 1 to length(PLine2 )
            if |T_PLine2 (j) - (T_PLine1 (i)+t)| < 2*TimeStep \* TimeStep is
                                1/data collection frequency; T_Pline is the time stamp of the peak*\
                Num = Num+1
            end
        end
    end

    if MaxNum < Num
      MaxNum = Num
      Δt = t
    end

     Num = 0
     t =  t+TimeStep
end
```

APPENDIX C SPECIFICATIONS FOR FOSS IN THE US30 SHM SYSTEM

Channel	FOS Name	Grating length (mm)	Central Wavelength(nm)	Package dimension
Channel1	A-NS-WB-V	10	1577.5	210x20x1mm
	A-SS-WB-V	10	1582.5	210x20x1mm
	B-NG-BF-H	10	1517.5	210x20x1mm
	B-NS-BF-H	10	1522.5	210x20x1mm
	B-SS-BF-H	10	1527.5	210x20x1mm
	B-SG-BF-H	10	1532.5	210x20x1mm
	C-SG-BF-H	10	1537.5	210x20x1mm
	C-FB(SS)-BF-H	10	1542.5	210x20x1mm
	C-SS-WB-V	10	1547.5	210x20x1mm
	C-SG-CB(5)-V	5	1552.5	220x20x1mm
	C-SG-CB(4)-V	5	1557.5	220x20x1mm
	C-SG-CB(3)-V	5	1562.5	220x20x1mm
	C-SG-CB(2)-V	5	1567.5	220x20x1mm
	C-SG-CB(1)-V	5	1572.5	220x20x1mm
Channel2	D-SG-BF-H	10	1517.5	210x20x1mm
	D-SS-BF-H	10	1522.5	210x20x1mm
	D-NS-BF-H	10	1527.5	210x20x1mm
	D-NG-BF-H	10	1532.5	210x20x1mm
	C-NG-BF-H	10	1537.5	210x20x1mm
	C-FB(NS)-BF-H	10	1542.5	210x20x1mm
	C-NS-WB-V	10	1547.5	210x20x1mm
	C-NG-CB(5)-V	5	1552.5	220x20x1mm
	C-NG-CB(4)-V	5	1557.5	220x20x1mm
	C-NG-CB(3)-V	5	1562.5	220x20x1mm
	C-NG-CB(2)-V	5	1567.5	220x20x1mm
	C-NG-CB(1)-V	5	1572.5	220x20x1mm
Channel3	E-NG-BF-H	10	1517.5	210x20x1mm
	E-NG-CB(5)-V	5	1522.5	15x20x1mm
	E-NG-CB(1)-V	5	1527.5	15x20x1mm
	E-NS-WB-V	10	1532.5	210x20x1mm
	E-FB(NS)-BF-H	10	1537.5	210x20x1mm
	E-FB(SS)-BF-H	10	1542.5	210x20x1mm
	E-SS-WB-V	10	1547.5	210x20x1mm
	E-SG-CB(5)-V	5	1552.5	15x20x1mm
	E-SG-CB(1)-V	5	1557.5	15x20x1mm
	E-SG-BF-H	10	1562.5	210x20mm
	F-SG-BF-H	10	1567.5	210x20x1mm
	F-SS-BF-H	10	1572.5	210x20x1mm
	F-NS-BF-H	10	1577.5	210x20x1mm
	F-NG-BF-H	10	1582.5	210x20x1mm
Channel4	DB1	10	1522	210x20x1mm
	DB2	10	1527	210x20x1mm
	DB3	10	1532	210x20x1mm
	DB4	10	1537	210x20x1mm
	DB5	10	1542	210x20x1mm
	DB6	10	1547	210x20x1mm
	DB7	10	1552	210x20x1mm
	DB8	10	1557	210x20x1mm